Summer 2017

Ship maneuvers with discretized propeller and coupled propeller model/CFD

Alireza Mofidi
University of Iowa

SHIP MANEUVERS WITH DISCRETIZED PROPELLER AND COUPLED PROPELLER MODEL/CFD

by

Alireza Mofidi

A thesis submitted in partial fulfillment
of the requirements for the Doctor of Philosophy
degree in Mechanical Engineering in the
Graduate College of
The University of Iowa

August 2017

Thesis Supervisor: Professor Pablo M. Carrica

Graduate College
The University of Iowa
Iowa City, Iowa

CERTIFICATE OF APPROVAL

PH.D. THESIS

This is to certify that the Ph.D. thesis of

Alireza Mofidi

has been approved by the Examining Committee for
the thesis requirement for the Doctor of Philosophy degree
in Mechanical Engineering at the August 2017 graduation.

Thesis Committee: _____
Pablo M. Carrica, Thesis Supervisor

_____
Casey Harwood

_____
Juan E. Martin

_____
Albert Ratner

_____
Hiroyuki Sugiyama

To my lovely wife and my family

ACKNOWLEDGEMENTS

I would like to thank my advisor professor Pablo M. Carrica for the continuous support of my PhD study and research, for his patience, enthusiasm, and immense knowledge. His guidance helped me in all the time of research and writing this thesis. I would also like to thank my committee members, Professor Harwood, Dr. Martin, Professor Ratner and Professor Sugiyama, for serving as my committee members.

I would like to acknowledge the help and constructive comments from Dr. J. Ezequiel Martin. I thank all of the students and fellows I've had the opportunity to work with, for their suggestions and help during my studies.

Last but not the least, I would like to thank my lovely wife Farzaneh, my parents, Sonbole and Hassan Ali, and my sisters, Sepideh and Sara, for supporting me spiritually throughout writing this thesis and my life in general.

ABSTRACT

A high fidelity computational fluid dynamics approach to perform direct simulations of ship maneuvers is presented in this thesis. The approach uses dynamic overset grids with a hierarchy of bodies to enable arbitrary motions between objects, and overcome the difficulties in simulation of the moving rudder and rotating propeller. To better resolve propeller/rudder interaction a Delayed Detached Eddy Simulation turbulence model based on Menter's SST is used. The methodology was implemented in the general purpose RANS/DES/DDES research code REX, and is applied to the KRISO Container Ship (KCS) with moving rudder and rotating propeller in deep and shallow water. For the first time, a grid study is conducted for the self-propulsion condition for the propeller RPM, thrust, torque and lateral force, and for the roll and pitch motions, using grids of 8.7 (coarse), 24.6 (medium) and 71.3 (fine) million points. A grid study is also performed for the zigzag maneuver evaluating the maximum and minimum values of propeller thrust, torque and lateral force roll, pitch, yaw, roll rate, yaw rate and drift throughout the maneuver. An extensive comparison between predicted motions and forces of the direct simulations and the experimental data collected by Schiffbau-Versuchsanstalt Potsdam GmbH (SVA) and Flanders Hydraulics Research (FHR) are presented.

While the results and comparisons with experimental data show that using direct CFD to compute modified and standard maneuvers with moving rudder and rotating discretized propeller is feasible, computational cost remains an impediment for many practical applications. Coupling a dynamic overset CFD solver with a potential propeller code can dramatically reduce the computational time to perform maneuvering simulations by using one order of magnitude larger time step than direct simulation. This thesis

investigates the ability of a coupled CFD/potential propeller code approach to simulate maneuvers in ships, where the rudder is located downstream of the propeller. While the approach has been successfully applied to submarine maneuvers, in which the propeller wake is free of interference, the concept had not been evaluated before for cases where an object (the rudder) is immersed in the wake. The study is performed using the CFD code REX and the propeller code PUF-14. Performance of the coupled REX/PUF-14 approach is first tested studying propeller/rudder interaction, evaluating influence of the propeller/rudder gap size and rudder deflection on propeller performance curves and rudder forces, comparing against DDES simulations with a discretized rotating propeller. A grid study was performed for advance coefficient J=0.6 and a rudder angle δ=20 degrees for a propeller rudder gap of 0.2 times the rudder radius, with the resulting grid uncertainties for propeller thrust and torque coefficients suggesting that the effects of the grid changes are small for the present range of grid sizes. A 15/1 zigzag maneuver for the KCS container ship, in which case the rudder is very close downstream of the propeller, is then analyzed, and compared against discretized propeller simulations and experimental data. Self-propulsion coupled REX/PUF-14 results agree very well with experiments and discretized propeller simulations. Prediction of motions, forces and moments, and mean flow field with the coupled REX/PUF-14 approach are comparable to results obtained with discretized propeller simulations and agree with experiments well, though as implemented the coupled approach is unable to resolve tip vortices and other flow structures that interact with the rudder, potentially affecting prediction of flow separation. It can be concluded that coupled CFD/potential flow propeller approaches are an effective and economical way to perform direct simulation of surface ship maneuvers with CFD.

PUBLIC ABSTRACT

Predicting ship maneuvering capabilities, dynamic stability and the behavior of marine vessels in seaways has recently seen an increase in numerical and experimental research effort. Predicting ship maneuvering and performance has a major influence on: 1) navigational safety including the safety of passengers, crew, cargo, and 2) the ship itself and the evaluation of hydrodynamic loads, including forces and moments, needed for accurate prediction of dynamic stability and responses of the ship and its motion. This thesis focuses on dynamic overset Computational Fluid Dynamics (CFD) simulations of surface ship maneuvers in deep and shallow water. Two approaches are presented for simulations, direct CFD using discretized propeller and coupled CFD/potential flow solver using PUF-14 propeller model. Extensive simulations are performed with both approaches to evaluate the accuracy and performance of these methods in ship maneuvering simulations.

TABLE OF CONTENTS

LIST OF TABLES

LIST OF FIGURES

CHAPTER 1

INTRODUCTION

1.1 Overview

Predicting ship maneuvering capabilities, dynamic stability and the behavior of marine vessels in seaways has recently seen an increase in numerical and experimental research effort (ITTC 20111, ITTC 2014, SIMMAN 2008, SIMMAN 2014).

Maneuvering prediction and ship performance has a major influence on:

- Navigational safety including the safety of passengers, crew, cargo, and ship itself.
- The evaluation of hydrodynamic loads including forces and moments, needed for accurate prediction of dynamic stability and responses of the ship and its motions.
- Sustained ship absolute velocity and optimization of fuel consumption.

Prediction of maneuverability performance in the preliminary stage of ship design permits a designer to take proper measures in a timely fashion to achieve standard maneuvering criteria. Also, understanding ship behavior in maneuvering is critical for the ship designer to select appropriate maneuvering equipment for the ship. This equipment includes the type of rudder such as spade or balanced rudder, unbalanced rudder, semi-balanced rudder, flaps rudder, or pleuger rudder, and the type of propeller for the ship including fixed pitch, controllable pitch, slewable, or cycloidal such as Voith-Schneider propellers (Carlton 2012). The International Maritime Organization (IMO) (2002) has established standards for ship maneuverability performance. These standards include turning ability, course changing and yaw checking ability, initial turning ability, stopping ability, straight-line stability and course keeping ability. All the maneuvers, except

stopping, are required to be performed on both port and starboard sides. Figure 1 shows an overview of all available methods that predict ship maneuvers.

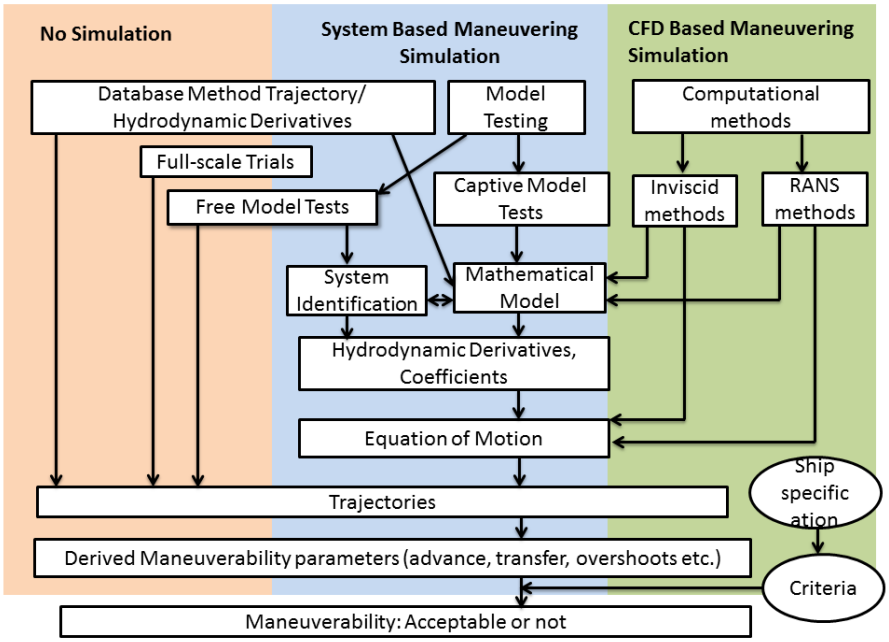

Figure 1.1 Overview of maneuvering prediction methods (ITTC, 2008).

The conventional methods to predict the ship maneuvering and seakeeping are based on Systems Based Simulation (SBS) and potential codes. While the SBS approach is extremely fast, it requires integral coefficients that need to be obtained from experiments or CFD (Carrica et al. 2013). The range of validity of these coefficients limits the applicability and accuracy of these models. Rudder and propeller behavior under complex inflows is very difficult to characterize for a wide range of conditions. Potential flow codes rely less on modeling since flow equations are solved, but suffer some limitations due to lack of physics related to viscous effects and treatment of the free surface. CFD is a higher fidelity method based on physical principles, and yields results that are typically more accurate with almost no need for empirical inputs. Use of CFD for maneuvering prediction

is becoming more popular as numerical algorithms improve and computers gain in power. Due to the importance of viscous effects on maneuvering, Unsteady Reynolds Averaged Navier-Stokes (URANS) and Detached Eddy Simulation (DES) approaches are used rather than inviscid solvers. URANS/DES simulations replace the static and dynamic Planar Motion Mechanism (PMM) experiments to obtain hydrodynamic derivatives and provide detailed local flow physics around the hull under maneuvering motions. Among several possible approaches that could be used to perform CFD of maneuvering ships, direct CFD simulation is the most complex and the one least reliant on models, though it requires capabilities for self-propulsion, rotating propellers, moving rudders and full 6DOF in a free surface environment. Due to complexity and cost, there has been only a limited number of direct CFD simulations for ship maneuvers. As high-performance computing systems become faster and less costly, direct CFD simulation of ship maneuvering is becoming feasible for a wider range of applications though it is still computationally expensive. Using coupled CFD/Potential approach is an alternative solution to reduce computational time for maneuvering simulations. In this method the overset CFD solver is coupled with a potential flow propeller code with the capability of exchanging propeller forces and moments, body forces and velocities at the propeller plane but allowing control surfaces such as rudders to still be resolved explicitly. There are several studies using the coupled method with fairly good results for Open Water Curves (OWC) computations and submarine maneuvering simulations. In these types of simulations usually there are no other moving objects that exist downstream of the propeller, and propeller wake is not affected by obstruction. As far as author of this thesis knows, standard surface ship maneuvering simulations with the coupled method and a moving rudder are presented for the first time in this thesis.

1.2 Literature Review of Maneuvering Prediction Methods

An overview of maneuvering prediction methods provided by the ITTC Maneuvering Committee (ITTC, 2008) is summarized as: predictions based on free model tests, captive model tests followed by simulations, empirical methods, system identification, viscous CFD, inviscid CFD, and hybrid methods.

Free model test predictions, since there are no assumptions made by experimentalists, are the closest to the reality of ship maneuvering. However, these tests are expensive and require a large basin and a model ship equipped with properly scaled rudder, propeller and controllers. They also suffer from a much lower Reynolds number than actual full scale ships, resulting in excessive viscous forces. In addition, free model tests do not provide physical understanding of processes affecting ship maneuverability or information for mathematical models used for maneuvering simulations. A series of free running tests for KCS have been conducted by SVA POTSDAM in Germany (2005-2006). Standard and modified zig-zag maneuvers and turning circle maneuvers are performed at different yaw checking and rudder angles. Results of standard 10/10 and modified 15/1 zig-zag maneuvers are used in this thesis to verify the CFD simulations.

Flanders Hydraulics Research (FHR) in Belgium (2010) studied ship behavior in confined areas and shallow water conditions. The facilities consist of a shallow water towing tank, equipped with a planar motion carriage, a wave generator and an auxiliary carriage for ship-ship interaction tests. The facilities are fully computer controlled and operated, both in captive and in free running mode. 20/5 zigzag maneuver experimental results of KCS in shallow water (Delefortrie and Eloot 2014) are used in this thesis for validation and verification studies.

Ship maneuvering predictions based on empirical methods rely on mathematical models and hydrodynamic derivatives. These models are based on empiricism or semi-theory/semi-empiricism (Aoki et al. 2006). Two important features of this method are low-cost and fast turnaround times. Also, this method can easily be used for different types of rudders and propellers. However, the method has limited accuracy and reliability. Dubbioso and Viviani (2012) used simplified mathematical models based upon semi-empirical regression formulae describing forces and moments acting on the hull and stern appendages of twin screw ships during maneuvering. A thorough analysis has been performed on a ship model equipped with 13 different stern appendage configurations and new formulae have been developed in order to describe accurately their influence on ship maneuvering behavior.

One of the most commonly used methods in maneuvering prediction is the system-based method. In this method the hydrodynamic derivatives are optimized by using sufficient amounts of data sets describing ship maneuvering, which are then inserted into the mathematical model. Generally, these data sets include a wide range of speeds, rudder angles, rudder rates and drift angles. This method can be applied to both model-scale and full-scale simulations. There are some limitations in using data sets for the mathematical models. For example, 10/10 zigzag maneuver data sets will not be capable of simulating a 20/20 zigzag maneuver.

Captive model tests are another common method used to predict ship maneuvering derivatives. In this method the hydrodynamic derivatives provide input for the creation of a mathematical model (Otzen and Agdrup 2008). The Planar Motion Mechanism (PMM) test, which is the main methodology for captive model tests, includes static and dynamic

tests. Static drift/rudder, steady turn and static speed with rudder motions are categorized in static PMM tests, while pure sway, pure yaw, combined yaw and drift, and yaw and rudder angle motions are categorized in dynamic PMM tests. These tests can be performed using a conventional towing tank equipped with a PMM motion generator. Captive model tests can also be performed in a basin with rotating arm capability. There are some limitations in using captive model tests. This method is time consuming and expensive in terms of experimental facilities. Satisfying Reynolds number (Re) and Froude number (Fr) similarity at the same time is possible only for small craft and large installations, thus scaling effects cannot be ignored. Also, these methods cannot provide physical insight of processes affecting the flow field around a ship during maneuvers.

Ship maneuvering predictions using Computational Fluid Dynamics is one of the most promising approaches these days. Using Unsteady Reynolds Averaged Navier Stokes (UANS) and Delayed Detached Eddy Simulation (DDES) methods instead of using inviscid methods helps study the viscous effects to obtain more accurate maneuvering predictions. URANS/DDES simulations can provide hydrodynamic derivatives for a mathematical model and also provide local flow information around the hull and rudder/propeller interaction, enabling studies to optimize performance.

1.3 Literature Review of CFD, Direct CFD and Coupled CFD/Potential Code Methods for Maneuvering Predictions

Ship maneuvering and seakeeping have been traditionally studied using experiments, potential flow and system-based methods. In recent years, CFD has become more popular as improvements in numerical algorithms, computer power, and lower cost

of access has enabled a wider range of user expertise. Performing CFD to predict maneuvering performance has the advantage of not using mathematical models or empirical values for various forces or viscous effects, but on the other hand it is considerably more expensive than system-based or potential flow approaches. The majority of maneuvering simulations are URANS using 1- and 2-equation isotropic/anisotropic models and the Reynolds-stress transport model for turbulence modeling. Surface capturing methods such as level-set and volume of fluid are used to model the free surface, and a small number of simulations use surface tracking approaches for maneuvering applications.

Several RANS maneuvering approaches for ships with modeled propellers have been attempted with various levels of success. Jacquin et al. (2006) performed simulations of unsteady ship maneuvering using a free-surface RANS solver. The authors studied three phenomena. The first point was the ability to accurately predict ship dynamics with six degrees of freedom, when it is only subject to forces and moments computed by the solver ICARE. The second point was to simulate rudder turning during ship maneuvering, and the last point was the ability to simulate ship self-propulsion, taking into account propeller effects in the flow. Muscari et al. (2008a) conducted numerical simulations of the turning circle maneuver for a VLCC hull. A RANS solver based on dynamic overlapping grids was used that couples the Navier-Stokes equations to the solution of the dynamic equations of a rigid body. The authors showed that the complete maneuver could be obtained in a reasonable time with good resolution of the main features of the flow, including the formation of the bilge vortices. These approaches with modeled propellers are less expensive than direct simulation of the propeller primarily because the time step is not

limited by the stringent requirements to resolve the propeller flow, and are thus attractive. In one of the first direct simulations of appendages, Pankajakshan et al. (2004) performed RANS calculations of the maneuvering vessel ONR Body 1, using pre-generated grids to account for the motions of the appendages. Jensen et al. (2004) computed a turning circle maneuver with a body force model for the propeller and resolving the free surface for a container ship. Venkatesan and Clark (2007) simulated the ONR Body 1 model submarine with 6DOF for the first time using an explicit rotating propeller. They treated the relative motions between bodies by using deformable grids while the free surface was neglected in their simulations. Muscari et al. (2008b) computed a turning circle maneuver of the very large crude carrier model KVLCC2 using RANS with the rudders and propellers. They did not compute the free surface for their simulations and their computation was limited to only three degrees of freedom. Broglia et al. (2008) performed RANS simulations of the flow past the KVLCC1-2 MOERI tankers with prescribed pure sway and pure yaw motions. Rudder and propeller were included in the discrete model and the free surfaces were neglected, using an iterative coupled RANS/BEM model to simulate the propeller. The dynamic overlapping grid approach was implemented to handle the body motion. The results showed a strong correlation between vortical structures shed from the edge of the hull, surface pressure, cross flows and the time histories of the hydrodynamic forces and moments. Cura Hochbaum et al. (2008) performed RANS simulations of static and dynamic captive model tests for the tankers KVLCC1 and KVLCC2 to obtain a suitable set of hydrodynamic coefficients for standard maneuvers simulations. The results showed that usual maneuvering derivatives can be determined with RANS with enough accuracy. Ferrant et al. (2008) performed turning maneuvering simulations of DTMB5415 in regular

waves with 6 degrees of freedom using body force propeller and side force rudder. Simulations of wave-structure interactions were handled by the spectral wave explicit Navier-Stokes equations (SWENSE) approach, while the free surface was modeled by using a surface tracking method. Drouet et al. (2008) simulated unsteady ship maneuvering in calm water and waves using a free-surface RANS solver. Computations of a 6DOF free model in turning motion in calm water and regular waves are considered. Simulations were performed with constant forces simulating propeller thrust and rudder lift. They showed that the interactions between hull, propeller and appendages have important effects on the behavior of a maneuvering ship.

The dynamic overset technique was used to perform DES simulation of a 35 degree rudder turn and 20/20 zigzag maneuvers of the KVLCC1 model ship in 6DOF, including free surface, rotating propeller and moving rudder, but the rudder was approximated as a spade rudder to simplify the geometry (Carrica and Stern 2008a). These simulations were performed blindly and results showed that the grid was not fine enough to properly simulate the flow field and integral quantities. Carrica et al. (2013) conducted unsteady Reynolds averaged Navier-Stokes (URANS) computations of turn and zigzag maneuvers of a surface combatant with dynamic overset grids at model and full scale. Simulation results were compared against available experimental integral variables and time history results. The differences between CFD and EFD were mostly within 10% for maneuvering predictions, highly satisfactory given the degree of complexity of these computations. Results indicate feasibility of using URANS to compute standard maneuvers and more complex situations like maneuvers in waves.

In SIMMAN 2014, prediction capabilities of different ship maneuvering simulation methods, including systems-based and CFD, were tested blindly against experimental data for KVLCC2, KCS and DTMB 5415. In addition to the deep water IMO maneuvers, SIMMAN 2014 also focused on maneuvering in shallow water. The maneuvering behavior of a ship becomes even more important when approaching a harbor where the available water depth is limited and the ship feels forces due to the interaction with the environment (other ships, banks, etc.). Larger ship size leads to more restricted maneuvering space, as the harbors and access channels cannot follow the pace of increasing ship size. Toxopeus (2013) performed CFD calculations to study the influence of the water depth on the flow field and the forces and moments on the ship for the full-block hull form of KVLCC2. The results showed a clear dependence of the forces and moments on the water depth. Shallow water results demonstrated that the flow separation is increased at the stern. Also, flow separation is more significant in maneuvering conditions compared to straight ahead conditions.

Araki et al. (2014) performed URANS PMM simulations and RANS rudder angle simulations for the KVLCC2 tanker using an overset grid approach. The results showed difficulty in convergence for the nonlinear maneuvering coefficients while the linear coefficients showed reasonable convergence at small time steps.

Cura-Hochbaum and Uharek (2014) performed standard maneuvers simulations for KCS by using a mathematical model of Abkowitz type. They determined the hydrodynamic coefficients by means of virtual model tests performed with the RANS code Neptun. The results of the turning circle and zigzag tests in deep water fulfill all IMO recommendations with margin. For the shallow water case the results showed larger advance and transfer

values and much smaller overshoot and drift angles. Guilmineau et al. (2014) carried out URANS simulations of a planar motion mechanism for DTMB 5415 and KVLCC2. They results showed relatively good agreement with experimental data, even for static drift with the appended hull for which a full RANS simulation was performed. They did not perform a full RANS simulation for dynamic maneuvering with operating propeller due to excessive CPU cost. They suggested RANS-BEM coupling method might be useful to perform dynamic maneuvering simulation.

Mikkelsen et al. (2014) performed simulations of pure sway PMM maneuvers using a RANS solver for the KCS container ship with rudder and propeller. The propeller was modeled as a virtual disk adding momentum to the flow and forces of the ship. They also performed a mesh study which showed that monotonic and oscillatory convergence was achieved.

Full direct CFD simulations of maneuvers of ships and submarines have been presented recently. 10/10 and 15/1 zigzag maneuvers of the Potsdam Model Basin (SVA) KCS model with a moving rudder and rotating propeller were computed by Mofidi and Carrica (2014a). The simulations were performed at model scale in deep water, for approach velocity corresponding to $Fr = 0.26$, showing comparisons with towing tank zigzag tests. Simulations of a 20/5 zigzag maneuver of the SVA KCS model with moving rudder and rotating propeller were conducted by Mofidi and Carrica (2014b). The simulations were performed at model scale in shallow, calm water, for approach velocities corresponding to a full-scale velocity of 8.75 knots (Fr=0.095). Self-propulsion was achieved using a PI controller which acts on the propeller rotational speed, allowing the ship to surge, heave, roll and pitch. Once the approach speed was stable, the ship was freed

to move in six degrees of freedom (6DOF) and the maneuver begins at constant RPM. A Delayed Detached Eddy Simulation (DDES) turbulence model based on Menter's SST was used. Verification studies were performed for three grids with 8.7, 24.6 and 69.6 million grid points for coarse, medium and fine grids, respectively. Verification studies showed that motions, forces and moments are fairly insensitive to the grid size, but not the flow field in the wake. Shen et al. (2014) performed RANS simulations of zigzag and turn maneuvers of DTMB 5415M, KVLCC2 and KCS with moving rudder and propeller using overset grids in OpenFOAM. The approach showed great flexibility and the ability to perform complex computations with relatively coarse grids. Chase et al. (2013) performed simulations of horizontal and vertical overshoots of the submarine models DARPA Suboff. The effect of the turbulence model on the wake was compared with RANS, DES, DDES and with no turbulence model. Results showed that RANS overly dissipates the wake, and that in the solution with the no turbulence model the tip vortices quickly become unphysically unstable.

Shen et al. (2015) implemented dynamic overset grid technique into the open source code Open FOAM with application to KCS self-prolusion and maneuvering. The implementation relied on the code Suggar to compute the domain connectivity information (DCI) dynamically at run time. A towed condition of the KCS was used for static overset tests and KP505 open-water curves, and self-propulsion and zigzag maneuvers of the KCS model were used to validate the dynamic overset grid implementation. Computations of the towed bare hull KCS were performed for the self-propulsion condition. Free surface, resistance and nominal wake were compared with experimental data showing good agreement. For open-water computations of KP505 propeller, overset and non-overset

grids techniques were used and the results did not show significant discrepancies. They also conducted simulations of zigzag maneuvers for the SVA KCS model with direct simulation of the rotating propeller and the moving rudder. The simulations showed good agreement with experimental data, including ship motions, propeller forces and rudder angle. The overshoot angle was under-predicted due to excessive rudder turning moment caused by inability to predict separation on the rudder.

Carrica et al. (2016) performed a study of a 20/5 zigzag maneuver for the KCS containership in shallow water with a depth to draft ratio $\frac{h}{T} = 1.2$, including experimental fluid dynamics (EFD) and CFD, using the fully implicit dynamic overset solver REX. Since there are some obstacles in performing the standard zigzag maneuver at a small rudder angle, such as 5 degrees, for less stable or unstable ships like large container ship, a modified maneuver was executed to examine course keeping and maneuvering qualities. In the case of a fully loaded container ship the standard zigzag maneuver usually cannot be completed because the trajectory of the ship diverges and the difference between course angle and the original course grows too large. Therefore, the modified zigzag maneuver was used to evaluate course keeping qualities in conditions similar to actual operation.

While the results and comparisons with experimental data show that direct CFD simulations of modified and standard maneuvers are feasible, computational cost remains too high for many practical applications. Coupling a dynamic overset CFD solver with a potential propeller code can dramatically reduce the computational time to perform maneuvering simulations by using a time step that is one order of magnitude larger than direct simulation.

Warren (1999) developed a method to analyze the maneuvering forces on marine vessels with a complex propulsion system. He developed an unsteady lifting-surface method to predict the maneuvering forces and moments and used PUF-14 for propeller modeling. He also coupled the unsteady lifting-surface method with RANS solver to estimate the maneuvering forces. The model has been tested for wide range of geometries and conditions for validation and verification.

Steady OWC and unsteady inclined shaft analyses of propeller model 4661 were performed with RANS/PUF-14 coupled method by Black and Michael (2003). They presented simulations of two horizontal overshoot maneuvers of the ONR Body 1 with the coupled approach. The open water curve simulations predicted propeller performance well at advance ratios close to design point, but the slope of the curve did not have a slope similar to the experimental data. This is due to not capturing the wake roll up and leading edge separation. The maneuvering simulations data showed the over-prediction of heading and roll angles in the coupled method compared to experimental data. They also explained that at high rudder angle during the maneuver, flow separation on the model could not be captured by the RANS code and therefore, the coupled method over-predicted the results.

The discretized propeller or fully resolved approach is a common method to simulate the propeller in ship maneuvering or open water curve conditions. Krasilnikov (2013) presented detailed CFD simulations on the benchmark container ship MOERI KCS using the coupled viscous/potential approach and a fully unsteady RANS method. His results showed that both approaches are accurate for the hull-propeller interaction analysis for self-propulsion simulations, although the direct method showed better agreement with experimental results than did the coupled method. Rijpkema et al. (2013) numerically

investigated the propeller-hull interaction using a coupled RANS/BEM approach for propeller loading. They performed the computation for a self-propulsion condition and they did not include a rudder in their simulations. Their results showed a prediction of the rotation rate and propeller thrust within 2 to 3% of the experimental results.

Propelled submarine simulation in towed, self-propelled and maneuvering conditions was conducted by Chase et al. (2013). The free running simulation of the DARPA Suboff submarine was considered in a horizontal overshoot maneuver. The coupled PUF-14/CFDShip-Iowa was used to perform the computations. The results showed good agreement between the discretized propeller and coupled approaches for open water curves simulations. The towed and self-propelled conditions also presented satisfactory simulation results. In their study the overshoot maneuver case depicts different trends between the discretized and coupled approach when the simulation conditions were close to high load propeller conditions and large wake distortions.

Martin et al. (2015a) coupled the MIT propeller code PUF-14 (Warren, 1999) with an overset CFD code to simulate maneuvers of the submarine ONR Body-1. The CFD/PUF-14 coupled approach results were compared with direct simulation and experiments for a variety of maneuvers, showing that the coupled approach can be considered as an alternative for direct propeller simulation for advance ratios close to the design point. The simulation results showed that the coupled approach can run about five times faster than the discretized propeller simulation approach. One of the main disadvantages of coupled method compared to the discretized approach was poor propeller wake resolution and capture of flow field details, but prediction of forces, moments and motions was good.

Martin et al. (2015b) presented validation of a propeller model for maneuvering applications by using two modeling strategies for propellers, an unsteady Reynolds averaged Navier-Stokes solver with discretized propeller and coupled CFD/PUF-14 method. Oblique propeller conditions are considered to simulate maneuvering conditions since the propeller encounters incoming flow with an important lateral component. Results showed good agreement between discretized propeller simulation and experiment, while the coupled CFD/PUF-14 model predicted the mean propulsion values well, but under-predicted higher harmonics.

Neitzel et al. (2015) studied the effect of different propeller modeling methods on maneuvering simulations and rudder forces. They used three different approaches: a fully modeled propeller, a coupled RANS/potential method, and an actuator disk. The computational results were compared with captive propulsion test results to evaluate the applicability of the different propulsion modeling methods for ship maneuvering simulations. The fully modeled propeller results showed good agreement with experimental data, and the results for actuator disk and the Boundary Element Method (BEM) coupling technique showed good agreements with measurement data, but only for advance coefficients close to the design condition.

1.4 Contribution of this Thesis

This thesis assesses direct CFD simulation of maneuvers with the naval hydrodynamics code REX, and performs validation and verification of ship self-propulsion and maneuvering. Direct simulations are presented for KCS container ships in deep and shallow water for both standard and modified zigzag maneuvers. Extensive comparisons

of results with experimental data sets are performed. Due to complexity and cost, verification studies for simulations of free running ships with directly moving propellers and rudders are not available in the literature. For the first time grid studies of the self-propulsion condition and the 20/5 zigzag maneuver are performed. In these computations the fully appended geometry is directly discretized, accurately following the geometry in the experiments. This direct approach is expensive, but eliminates modeling of propellers or appendages, and attempts to resolve all physics involved in the maneuver, leaving turbulence as the only aspect needing mathematical modeling. The grid study is performed for the nominal rudder rate condition as part of a blind test. The rudder rate is then corrected to match the experimental value and computations repeated on the medium grid, performing extensive comparisons against EFD data for pitch, roll, yaw, yaw rate and rudder angles, and forces and moments in the propeller.

Although direct simulation is still expensive in terms of CPU time, simulation results show excellent agreement with the experimental results. The final goal of this thesis is to improve computational speed retaining the most important features of the flow. The first strategy is to use grids as coarse as possible for simulation. Coarser grids make simulations faster by allowing use of less grid points per available processor. Two considerations are important in an overset grid system such as the one used in this work: a) the overlap has to be enough to guarantee a valid domain connectivity and b) the coarse grid has to yield appropriate forces and moments. Grids too coarse fail on both accounts, and should be avoided. The results of using coarser grids are presented in this work.

The second strategy is using CFD/potential code coupled approach. Coupling a dynamic overset CFD solver with a potential propeller code can dramatically reduce the

computational time to perform maneuvering simulations by using one order of magnitude larger time step than is used in direct simulation. In most cases a time step such that the ship advances one ship length in 200~400 time steps is adequate to handle the flow around the ship. The propeller requires a much smaller time step, usually 10 times smaller, causing a significant increase in the total computation time. In the case of most submersible designs, the propeller wake is free of obstructions since rudders and other appendages are located upstream of the propeller, making it an ideal case for use of coupled CFD/potential flow solvers. In most surface ships the rudder is located in the propeller wake, thus reducing the accuracy of the propeller potential flow solver, which typically assumes an unobstructed wake. In this thesis we investigate the extent of the influence of rudder presence in the wake of a propeller in the propeller performance, and the influence on maneuvers of the KCS container ship, where the rudder is very close downstream from the propeller.

CHAPTER 2

COMPUTATIONAL METHODS

In this chapter details of the CFD code REX are discussed. A concise review of the code, flow solver and their mathematical foundations are covered here.

2.1 CFD Code REX

The computations in this thesis were performed with the ship hydrodynamics CFD code REX. REX is an URANS/DES/DDES CFD solver with dynamic overset grids capability developed at the University of Iowa, and is being continuously developed. The latest implementations have greatly augmented capabilities, robustness and speed, while reducing memory footprint. An unsteady single-phase level set capturing approach is used to model the free surface (Carrica et al. 2007a), which allows for robust computations and large amplitude/steep waves. A dynamic overset technique is used for grid deformation or relative motions, in which the overset grid connectivity is computed with Suggar or Suggar++ (Noack et al. 2009) at run time or as a pre-processing step for static problems. REX has unique capabilities to compute polydisperse bubbly wake flows (Castro and Carrica 2013), as well as density stratified flow models (Esmaeilpour et al. 2016). The code solves for full 6 degrees of freedom (6 DOF) motions with a parent/child hierarchy of objects, allowing for multi-object simulations, and motion of control surfaces and appendages (Carrica et al. 2007b). Other high-level models include proportional-integral-derivative (PID) based controllers for control of heading, speed or attitude (Carrica et al. 2008b), passive controllers to perform maneuvers (Chase et al. 2013, Mofidi and Carrica 2014, Martin et al. 2015, Carrica et al. 2016), and a linear/non-linear fluid-structure interaction solver (Paik et al. 2009, Paik and Carrica 2014). The code uses an MPI-based

domain decomposition approach for large-scale and high-performance computations (Carrica et al. 2010b). Recent improvements include a quaternion-based multibody dynamics (MBD) approach to solve bodies and cables simultaneously, implementation of a new pressure-velocity coupling approach that improves enforcement of the continuity and enables high void fraction or air/water computations (Li et al. 2015a), coupling with the MBD code Virtual.lab (Li et al. 2015b) and a universe/system/planet overset decomposition technique to run large-scale motion problems.

2.2 Governing Equations

Though REX can handle variable density, Eulerian bubble transport and other complex models, only the equations relevant to this thesis will be described here. All variables and properties of incompressible Navier-Stokes equations are non-dimensionalized using the reference velocity and length, U and L, usually the ship's speed and length between fore and aft perpendiculars, and corresponding fluid properties. REX solves the incompressible Navier-stokes equations in an inertial coordinate system. The coordinates system can be fixed to an object moving at constant speed or in the earth system. The dimensionless mass and momentum equations written as:

$$\frac{\partial u_i}{\partial x_j} = 0 \tag{2.1}$$

$$\frac{\partial u_i}{\partial t} + \frac{\partial u_i u_j}{\partial x_j} = -\frac{\partial p}{\partial x_j} + \frac{\partial}{\partial x_j}\left[\frac{1}{Re_{eff}}\left(\frac{\partial u_i}{\partial x_j} + \frac{\partial u_j}{\partial x_i}\right)\right] + S_i \tag{2.2}$$

Where u is the fluid velocity and S_i is a source term due to body forces, e.g. a propeller model; p is the dimensionless piezometric pressure, $p = {p_{abs}}/{\rho U_0^2} + {z}/{Fr^2} + {2k}/{3}$ with

p_{abs} the absolute pressure respect to atmospheric; Re_{eff} is the effective Reynolds number, defined as $1/Re_{eff} = 1/Re + \nu_t$; $Re = U_0 L/\nu$ is the Reynolds number for water; k and ν_t are the turbulent kinetic energy and turbulent eddy viscosity, respectively, obtained from the turbulence model.

2.3 Turbulence Models

The turbulence is modeled using a delayed detached eddy simulation (DDES) model (Gritskevich et al. 2011) based on Menter's shear stress transport model (SST) (Menter 1994), where the turbulent kinetic energy k and the specific dissipation rate ω are computed from

$$\frac{\partial k}{\partial t} + \frac{\partial (u_i k)}{\partial x_i} = \frac{\partial}{\partial x_i}\left[(\nu + \sigma_k \nu_t)\frac{\partial k}{\partial x_i}\right] + P_k - \frac{\sqrt{k^3}}{l_{DDES}} \tag{2.3}$$

$$\frac{\partial \omega}{\partial t} + \frac{\partial (u_i \omega)}{\partial x_i} = \frac{\partial}{\partial x_i}\left[(\nu + \sigma_\omega \nu_t)\frac{\partial \omega}{\partial x_i}\right] + 2(1 - F_1)\sigma_{\omega 2}\frac{1}{\omega}\frac{\partial k}{\partial x_i}\frac{\partial \omega}{\partial x_i} + \alpha\frac{1}{\nu_t}P_k - \beta\omega^2 \tag{2.4}$$

$$\nu_t = \frac{a_1 . k}{\max(a_1 . \omega, F_2 . S)} \tag{2.5}$$

Where F_1 and F_2 represent the SST blending functions:

$$F_1 = \tanh(arg_1^4) \tag{2.6}$$

$$arg_1 = \min(\max\left(\frac{\sqrt{k}}{C_\mu \omega d_\omega}, \frac{500\nu}{d_\omega^2 \omega}\right), \frac{4\sigma_{\omega 2} k}{CD_{k\omega} d_\omega^2}) \tag{2.7}$$

$$CD_{k\omega} = \max\left(2\sigma_{\omega 2}\frac{1}{\omega}\frac{\partial k}{\partial x_i}\frac{\partial \omega}{\partial x_i}, 10^{-10}\right) \quad (2.8)$$

$$F_2 = \tanh(arg_2^2) \quad (2.9)$$

$$arg_2 = \max\left(\frac{2\sqrt{k}}{C_\mu \omega d_\omega}, \frac{500\nu}{d_\omega^2 \omega}\right) \quad (2.10)$$

Where d_ω is the distance to the nearest wall. P_k in equation (2.3) is defined as follows:

$$P_k = \min\left(\nu_t S^2, 10\,.\,C_\mu k\omega\right) \quad (2.11)$$

Where $S = \sqrt{2S_{ij}S_{ij}}$ is the strain rate magnitude and $S_{ij} = 1/2(\frac{\partial u_i}{\partial x_j} + \frac{\partial u_j}{\partial x_i})$. The DDES length scale in equation (2.3) reads as:

$$l_{DDES} = l_{RANS} - f_d \max(0, l_{RANS} - l_{LES}) \quad (2.12)$$

$$l_{RANS} = \sqrt{k}/C_\mu \omega \quad (2.13)$$

$$l_{LES} = C_{DES} h_{max} \quad (2.14)$$

$$C_{DES} = C_{DES1}.F_1 + C_{DES2}.(1 - F_1) \quad (2.15)$$

where h_{max} is the maximum edge length of the cell. In equation (2.12), f_d is an empiric blending function defined as

$$f_d = 1 - tanh[(C_{d1} r_d)^{C_{d2}}] \quad (2.16)$$

$$r_d = \frac{\nu_t + \nu}{\kappa^2 d_\omega^2 \sqrt{0.5\,.\,(S^2 + \Omega^2)}} \quad (2.17)$$

where S is the strain rate magnitude tensor and Ω is the vorticity magnitude tensor. The model constants are $C_\mu = 0.09, \kappa = 0.41, a_1 = 0.31, C_{DES1} = 0.78, C_{DES2} = 0.61, C_{d1} =$

20 and $C_{d2} = 3$. The model constants are $\alpha_1 = 5/9$, $\beta_1 = 0.075$, $\sigma_{k1} = 0.85$, $\sigma_{\omega 1} = 0.5$, $\alpha_1 = 0.44$, $\beta_1 = 0.0828$, $\sigma_{k2} = 1$ and $\sigma_{\omega 2} = 0.856$. α, β, σ_k and σ_ω are computed by the blending function F_1 as $\alpha = \alpha_1 . F_1 + \alpha_2 . (1 - F_1)$.

2.4 Free Surface Modeling

REX uses an unsteady single-phase level set method to model the free surface (Carrica et al. 2007a). The level set function ϕ is defined as the signed distance to the interface in the whole domain, positive in water and negative in air. Thus, $\phi = 0$ represents the free surface. The level set function ϕ must satisfy the transport equation with no mass interfacial transfer:

$$\frac{\partial \phi}{\partial t} + \boldsymbol{u} . \nabla \phi = 0 \tag{2.18}$$

Due to the big difference in viscosity and density between air and water the problem can be simplified to solving equations in the water phase only. By this simplification the jump conditions at free surface must be treated as a boundary condition enforced explicitly in a single-phase level set approach. The jump condition in any direction tangential to the free surface is (Carrica et al. 2007a)

$$[\mu(\nabla \boldsymbol{u} . \boldsymbol{n}) . \boldsymbol{t} + \mu(\nabla \boldsymbol{u} . \boldsymbol{t}) . \boldsymbol{n}] = 0 \tag{2.19}$$

By neglecting the viscosity in air, the boundary conditions at the interface for velocity are obtained as

$$\nabla \boldsymbol{u} . \boldsymbol{n} = 0 \tag{2.20}$$

In the normal direction the jump condition can be expressed as:

$$[p_{abs} - 2\mu(\nabla \boldsymbol{u}.\boldsymbol{n}).\boldsymbol{n}] = 0 \tag{2.21}$$

where $\boldsymbol{n} = -{}^{\nabla\phi}/_{|\nabla\phi|}$ is the unit normal vector on the free surface from water into air. As a good approximation the pressure can be considered as constant in the air (the atmospheric pressure). Also, assuming that the contribution of the turbulent kinetic energy to the free surface is negligible, the dynamic free surface boundary condition can be written as

$$p_{int} = \frac{z_{int}}{Fr^2} \tag{2.22}$$

The re-initialization of the level set function is an important step to keep it a smooth distance function and have a transition region uniform in thickness. For the single-phase level set approaches, since the normal is used in the boundary conditions and in the air it used to extend velocities and turbulent quantities, then the normal must be evaluated at the interface accurately. To satisfy these requirements the level set function is reinitialized periodically everywhere but at the interface by solving:

$$\boldsymbol{n}.\nabla\phi = sign(\phi_0) \tag{2.23}$$

where $\boldsymbol{n}$ in this case is the normal pointing to the fluid being reinitialized and ϕ_0 is the level set function prior to re-initializing. $\boldsymbol{n}$ was given by Eq. (2.21) for air and negative of the same equation for water. Therefore, equation (2.23) is an Eikonal equation propagating information outwards from the interface. Also, Eq. (2.23) is nonlinear because n is a function of ϕ and requires iterations to converge.

2.5 Kinematics of Motions

Ship motions are described in terms of an Earth-fixed inertial reference coordinate frame and a ship-fixed frame, as shown in Fig. 2.1.d. The full six degrees of freedom are considered in this thesis to predict the ship motions during the maneuvers. The fluid flow equations are solved in the Earth-fixed coordinate system. Ship motions are represented by translations and rotations with respect to the inertial frame, and the linear and angular velocity and the forces an moments with respect to ship-fixes frame. Orientation and position of the ship are computed by linear translations and the Euler angles of roll, pitch and yaw, as shown in Fig. 2.1.a, b, c:

$$\boldsymbol{\eta} = (\boldsymbol{\eta}_1, \boldsymbol{\eta}_2) = (x, y, z, \phi, \theta, \psi) \tag{2.24}$$

The linear and angular velocities are solved in the ship reference system as:

$$\boldsymbol{\nu} = (\boldsymbol{\nu}_1, \boldsymbol{\nu}_2) = (u, v, w, p, q, r) \tag{2.25}$$

where u , v and w are the surge, sway and heave velocities of the ship, and p, q and r are the roll, pitch and yaw angular velocities in the ship system. Time rates of change in the Euler angles can be related to the angular velocities in the ship system by using the transformation matrix (Fossen 2011)

$$v_2 = \begin{bmatrix} 1 & 0 & -sin\theta \\ 0 & cos\phi & cos\theta sin\phi \\ 0 & -sin\phi & cos\theta cos\phi \end{bmatrix} \dot{\boldsymbol{\eta}} S_2 = \boldsymbol{J}_2^{-1} \dot{\boldsymbol{\eta}}_2 \tag{2.26}$$

and for the linear velocities:

$$v_1 = \boldsymbol{J}_1^{-1}\dot{\boldsymbol{\eta}}_1$$

$$= \begin{bmatrix} cos\psi cos\theta & sin\psi cos\theta & -sin\theta \\ -sin\psi cos\phi + sin\phi sin\theta cos\psi & cos\psi cos\phi + sin\phi sin\theta sin\psi & cos\theta sin\phi \\ sin\theta sin\psi + cos\phi sin\theta cos\psi & -sin\phi cos\psi + cos\phi sin\theta sin\psi & cos\theta cos\phi \end{bmatrix} \quad (2.27)$$

where J_1^{-1} is the rotation matrix which projects a vector from the Earth-fixed system into the ship-fixed system.

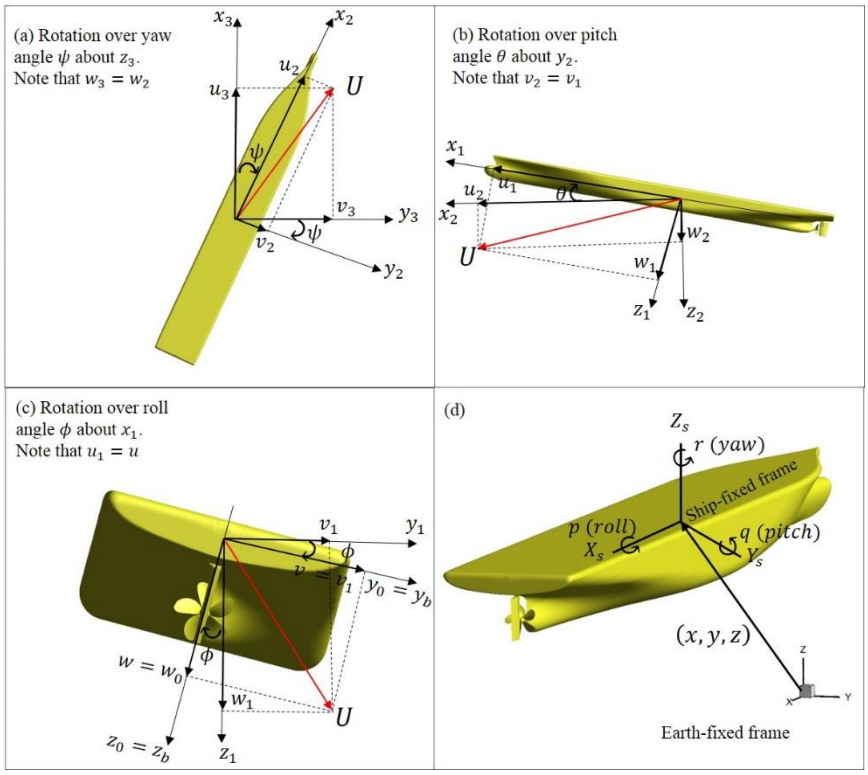

Figure 2.1 (a), (b) and (c) Euler angle rotation sequence (zyx convention). The ship is rotated from Earth-fixed coordinate system$(x_3, y_3, z_3)$to Body-fixed coordinate system(x_b, y_b, z_b). (d): CFD customary Earth- and ship-fixed reference coordinate system.

The inertia tensor is diagonal if it is assumed that the principal axes of inertia are coincident with the ship-fixed coordinate system. The components of inertia tensor are $(I_{xcg}, I_{ycg}, I_{zcg})$ with respect to the center of gravity. In some situations the center of

rotation of the ship is different than the center of gravity such as a ship rolling about an axis that does not pass through the center of gravity. In this case the moments of inertia described with respect to the center of rotation as:

$$I_x = I_{xcg} + m(y_G^2 + z_G^2)$$

$$I_y = I_{ycg} + m(x_G^2 + z_G^2) \tag{2.28}$$

$$I_z = I_{zcg} + m(x_G^2 + y_G^2)$$

where $\boldsymbol{X}_G = \boldsymbol{X}_{rot} - \boldsymbol{X}_{cg}$. Therefore, the rigid body equations read:

$$m[\dot{u} - vr + wq - x_G(q^2 + r^2) + y_G(pq - \dot{r}) + z_G(pr + \dot{q})] + \zeta_u u = X$$

$$m[\dot{v} - wp + ur - y_G(r^2 + p^2) + z_G(qr - \dot{p}) + x_G(qp + \dot{r})] + \zeta_v v = Y$$

$$m[\dot{w} - uq + vq - z_G(p^2 + q^2) + x_G(rp - \dot{q}) + y_G(rq + \dot{p})] + \zeta_w w = Z \tag{2.29}$$

$$\left[I_x\dot{p} + \left(I_z - I_y\right)qr + m\{y_G(\dot{w} - uq + vp) - z_G(\dot{v} - wp + ur)\}\right] + \zeta_p p = K$$

$$\left[I_y\dot{q} + (I_x - I_z)rp + m\{z_G(\dot{u} - vr + wq) - x_G(\dot{w} - uq + vp)\}\right] + \zeta_q q = M$$

$$\left[I_z\dot{r} + \left(I_y - I_x\right)pq + m\{x_G(\dot{v} - wp + ur) - y_G(\dot{v} - vr + wq)\}\right] + \zeta_r r = N$$

where ζ is a damping coefficient which is obtained from friction on the ship mounts in the experimental setup, or it can be added as an artificial form of inhibiting oscillations. If the cross-inertia terms are nonzero in the inertia tensor, the same translation shown in Eq. (2.28) can be used to diagonalize the inertia tensor:

$$I_{xy}^{cg} = -mx_G y_G$$

$$I_{xz}^{cg} = -mx_G z_G \tag{2.30}$$

$$I_{yz}^{cg} = -my_G z_G$$

In Eq. (2.30), if a symmetry plane is present the number of unknowns may exceed the number of equations. For example, if there is a symmetry about $y = 0$, which is a common case, only I_{xz}^{cg} in above equation is nontrivial and (xg, zg) are unknowns. To solve this problem an extra assumption as $xg = zg$ is needed. Since in most situations $I_{xz} \ll I_{xx}$ or I_{zz}, this correction is usually negligible. In particular, in the case of an acceleration leading to a steady state, all accelerations and rotational velocities are zero in the final condition, so the exact values used for mass and inertia tensor are immaterial.

Forces and moments are initially computed in the Earth-fixed system, where the fluid flow equations are solved. Forces and moments in the ship-fixed system are computed by integrating the forces on the ship's hull and all appendages including propellers, plus the gravitational force. In order to properly compute the area, forces and moments on grids overlapping on solid surfaces, the code USURP (Boger and Dryer 2006) is used as a preprocessing step to find weights for each cell. USURP computes the weights in such a way that overlapping cells are not double counted, yielding correct integrated values. Forces in the Earth-fixed system for are computed from summation of the viscous and hydrostatic and piezometric pressure forces

$$\mathbf{F}_e = \int_{ship} \left[\left(\frac{\nabla \mathbf{u} + \nabla \mathbf{u}^T}{2Re} \right) - \left(p - \frac{z}{Fr^2} \right) \mathbf{I} \right] . d\mathbf{a}_e + m\mathbf{g} \tag{2.31}$$

The total moments are calculated from integrating the elemental forces with the distance to the center of gravity r as:

$$\mathbf{L}_e = \int_{ship} \mathrm{r} \times \left\{ \left[\left(\frac{\nabla \mathbf{u} + \nabla \mathbf{u}^T}{2Re} \right) - \left(p - \frac{z}{Fr^2} \right) \mathbf{I} \right] . d\mathbf{a}_e \right\} + \mathbf{x}_G \times m\mathbf{g} \tag{2.32}$$

These forces and moments are then projected into the ship-fixed system using Eq. (2.27)

$$\mathbf{F} = \mathbf{J}_1^{-1} \mathbf{F}_e = (X, Y, Z) \tag{2.33}$$

$$\mathbf{L} = \mathbf{J}_1^{-1} \mathbf{L}_e = (K, M, N) \tag{2.34}$$

For the appendages, such as rudders and propellers, the same procedure is used to obtain forces and moments. Once the forces have been computed, the dynamic equations for the rigid-body motions are solved numerically using a third-order predictor/corrector implicit scheme (Carrica et al. 2007b). The new position and attitude of the ship are obtained by integrating the velocities, Eq. (2.29), the rates of change in Euler angles and velocities in ship-fixed system, Eqs. (2.26) and (2.27), over time. The output of the motion solver gives the new position and attitude of the ship, while the angular position of the rudder and propeller are obtained from controllers, to be discussed later. Once these parameters are available the grids are moved. The grids that move with appendages are rotated around the rotation axis as

$$\mathbf{x}_n = \begin{bmatrix} r_x^2(1-c\beta)+c\beta & r_x r_y(1-c\beta)-r_z s\beta & r_x r_z(1-c\beta)-r_y s\beta \\ r_x r_y(1-c\beta)-r_z s\beta & r_y^2(1-c\beta)+c\beta & r_y r_z(1-c\beta)-r_x s\beta \\ r_x r_z(1-c\beta)-r_y s\beta & r_y r_z(1-c\beta)-r_x s\beta & r_z^2(1-c\beta)+c\beta \end{bmatrix} (\mathbf{x}_{in} - \mathbf{r}_1) + \mathbf{r}_1 \tag{2.35}$$

where $\mathbf{x}_{in}$ is the initial position of a point in the appendage before applying any transformation, $\mathbf{r}_1$ is the location of any point along the appendage's axis of rotation, and

(r_x, r_y, r_z) is the unit rotation axis vector. The translation and rotation of those grids belonging to the appendages that move with ship are obtained from

$$\mathbf{x}_{ship} = (\mathbf{J}_1^{-1})^T(\mathbf{x}_N - \mathbf{x}_{rot}) + \mathbf{x}_{rot} + \boldsymbol{\eta}_1 \tag{2.36}$$

To better capture the free surface, background and refinement grids are generated and these grids are only allowed to surge, sway and yaw by imposing zero heave, roll and pitch, forcing them to maintain alignment with the free surface.

2.6 Dynamic Overset Approach

Simulation of bodies in relative motion and simplification of structured grid generation for complex geometries, such as fully appended ships and submarines, can be achieved using the overset grids technique. Overset grids enables separate overlapping grids to move independently almost without limitations. The connections between these grids are formed by interpolation at appropriate cells or points to couple the solution on the different grids. Those points located outside the domain of interest, such as inside a body, are excluded from the computations and marked as holes. Fringe or receptor points surround the hole points and require boundary values to be applied. Those boundary values are provided by donor cells which supply information by interpolating from a donor grid to the fringe point. For any variable ϕ the trilinear interpolation from the donor cell is expressed as

$$\phi = \sum_{i=1}^{n} \omega_i . \phi_i \tag{2.37}$$

where ω_i is the interpolation or weight coefficient and ϕ_i is the donor value for each donor point i in the cell. When a fringe point cannot find a valid donor cell, the fringe point is

labeled an orphan and the flow solver typically uses an averaging procedure to provide values in place of the interpolated values (Noack 2005). This situation usually happens in an overset grid system where the overlap between grids is insufficient to provide adequate donors for all the fringe points. Orphan points are unfavorable because they can reduce the coupling between overset grids. There are some techniques to avoid orphan points such as refining grid in the body normal direction which reduces the region that is marked as hole points and increases the active elements on that region. Refining the grid may not be feasible for all cases since it increases the number of grid points. In such situation the best solution may be to add an auxiliary grid to provide donor cells. Figure 2.2 shows an example of overlapping of a boundary layer grid and a background grid. Blue points are marked as blank or hole points, red points marked as active points and green points marked as interpolated points.

The Structured, Unstructured, and Generalized overset Grid AssembleR (SUGGAR) code, or its evolution Suggar++ (Noack et al. 2009), are used to obtain the overset domain connectivity between the overlapping grids as mentioned above. The information is contained in the *xintout* file with Pegasus format. For maneuvering simulations, dynamic overset is needed, in which case Suggar and REX exchange information with MPI. For dynamic motion conditions, the relative positions between overset grids changes every time step, requiring re-computation of the domain connectivity information (DCI) repeatedly. To avoid this costly process, Suggar runs in separate processors and the communication between REX and Suggar is handled with MPI. In the standard (no-lag) procedure for each time step, REX computes the flow solution first, then integrates the forces and moments and predicts the motions for the next time step. Once

Suggar receives the predicted motions it starts computing the DCI, and REX needs to wait until Suggar completes the computation of the DCI to start computation of the next time step or non-linear iteration. The no-lag procedure implies an essentially serial operation of SUGGAR and REX, where REX needs to wait for SUGGAR to complete the domain connectivity before it can read the overset information, while SUGGAR needs the relative positions between grids before it can start the computations. For most coarse grid, say about three million grid points, the cost is acceptable since SUGGAR takes about 5–25% of the total computational time, depending on the complexity of the overset assembly. For large cases SUGGAR may take longer than REX for a non-linear iteration and slow-down the computation significantly. To overcome this problem a lagged mode is a proper option as described in Carrica et al. (2010b). In this mode, SUGGAR is launched immediately after the transfer of the overset DCI to REX is completed. In lagged mode the transfer of the motions to SUGGAR and the transfer of the overset DCI to REX occur simultaneously. Since the final motions are not yet available, the last available position of the grids is provided to SUGGAR. As the time step converges, the difference in position of the grids between non-linear iterations decreases, resulting in SUGGAR and REX using essentially (exactly in perfect convergence) the same grid positions. Therefore, there is no penalty for using an implicit lagged mode if time step convergence is achieved.

If the time step is small or if a steady state solution is desired, then an explicit update of the motions can be used. In this mode the time step is computed using the motions provided by the predictor with the forces from the previous time step. The lagged mode can also be used in conjunction with the explicit mode, using motions from previous time steps to predict the grid positions at the current time, using for SUGGAR a first order

extrapolation. In this case SUGGAR has time to complete the overset assembly in the span it takes REX to perform a complete time step. The detailed procedure is shown in Fig. 2.3.

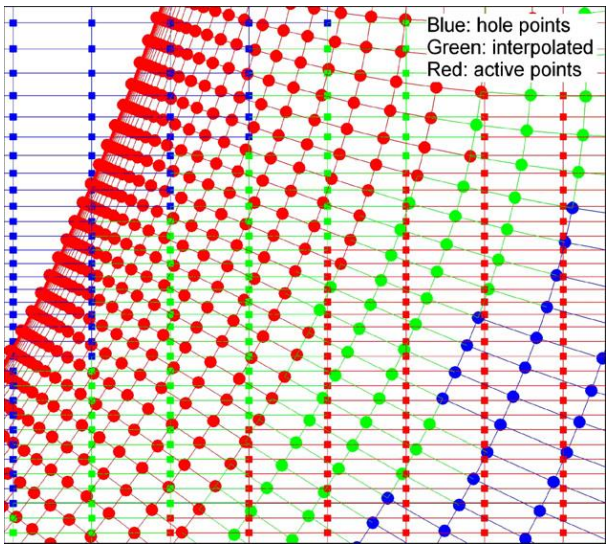

Figure 2.2 Overset grid arrangement points (Carrica 2007b).

2.7 Controllers

REX has several controllers available to facilitate simulation of self-propulsion, maneuvers, autopilots, etc. Feedback controllers are based on Proportional-Integral-Derivative actuators (PID), where the control surface is moved according to an error signal arising from the deviation from the target controlled variable (Carrica et al. 2008b). Limiting rate and action on the actuators are also implemented in REX. Passive controllers are also available, and are used to perform maneuvers such as zigzag, turning circles and horizontal or vertical overshoots.

Controllers offer a flexible way of imposing simple maneuvers, replicating experimental conditions, and analyzing the ship performance under different situations.

Controllers impose a variety of ramps in ship forward speed and propeller rotational speed, turning and zig-zag maneuvers, proportional integral derivative (PID) speed control (controlling a propeller body force model or a fully modeled rotating propeller), PID heading control (controlling rudder angle), PID autopilot (using simultaneously speed and heading control), waypoint control (using autopilot with variable heading), point track (to control a vehicle following a moving point), and others.

The controllers are logical, based on on/off signals and limiting action parameters, or active PID type. Limiters of action use physical limits of the actuators to add reality to the resulting actuator setting. For instance, a rudder has a maximum and minimum operational angle, and a maximum allowed rudder rate. PID controllers involve three separate parameters; the proportional value that determines the reaction to the current error, the integral value that determines the reaction based on the sum of recent errors and the derivative value that determines the reaction to the rate at which the error has been changing. The weighted sum of these three actions is used to adjust the actuator using the classical action law:

$$\psi = Pe + I\int_0^t e\,dt + D\frac{de}{dt} \tag{2.38}$$

where ψ is an action parameter, for instance the rudder angle, and e is the error of the controlled value respect to the target value (for instance heading respect to desired heading), given by:

$$e = \psi - \psi_{\text{target}} \tag{2.39}$$

By "tuning" the three constants in the PID controller algorithm, the controller can provide control action designed for specific process requirements. The PID controller parameters are constant throughout the computation, or may be programmed to change.

2.8 Numerical Methods

To accommodate complex geometries, generalized curvilinear coordinates are used. The governing equations are transformed from the physical domain in Cartesian coordinates (x, y, z, t) into the computational domain in non-orthogonal curvilinear coordinates (ξ, η, ζ, τ) (Thompson et al., 1985). Equations (2.1), (2.2), (2.3), (2.4) and (2.18) are re-written in the transformed domain as

$$\frac{1}{J}\frac{\partial}{\partial \xi^j}\left(b_i^j u_i\right) = 0 \tag{2.40}$$

$$\frac{\partial u_i}{\partial \tau} + \frac{1}{J} b_j^k \left(u_j - \frac{\partial x_j}{\partial \tau}\right)\frac{\partial u_i}{\partial \xi^k} = -\frac{1}{J} b_j^k \frac{\partial p}{\partial \xi^k} + \frac{1}{J}\frac{\partial}{\partial \xi^j}\left(\frac{1}{J}\frac{b_i^j b_i^k}{Re_{eff}}\frac{\partial u_i}{\partial \xi^k}\right) + \left(\frac{1}{J} b_j^k \frac{\partial v_t}{\partial \xi^k}\right)\left(\frac{1}{J} b_j^l \frac{\partial u_i}{\partial \xi^l}\right) + s_i \tag{2.41}$$

$$\left(\frac{\partial k}{\partial \tau} + \frac{1}{J} b_j^k \left(u_j - \frac{\partial x_j}{\partial \tau}\right)\frac{\partial k}{\partial \xi^j}\right) = \frac{1}{J}\frac{\partial}{\partial \xi^j}\left(\frac{1}{J}(\nu + \sigma_k \nu_t) b_i^j b_i^k \frac{\partial k}{\partial \xi^k}\right) + P_k - \frac{k^{\frac{3}{2}}}{l_{DDES}} \tag{2.42}$$

$$\left(\frac{\partial \omega}{\partial \tau} + \frac{1}{J} b_j^k \left(u_j - \frac{\partial x_j}{\partial \tau}\right)\frac{\partial \omega}{\partial \xi^j}\right) = \frac{1}{J}\frac{\partial}{\partial \xi^j}\left(\frac{1}{J}(\nu + \sigma_\omega \nu_t) b_i^j b_i^k \frac{\partial \omega}{\partial \xi^\omega}\right) + \frac{\alpha P_k}{\nu_t} - \beta\omega^2 + 2(1 - F_1)\sigma_{\omega 2}\left(\frac{1}{J} b_j^k \frac{\partial k}{\partial \xi^j} \cdot \frac{1}{J} b_j^k \frac{\partial \omega}{\partial \xi^j}\right)/\omega \tag{2.43}$$

$$\frac{\partial \phi_i}{\partial \tau} + \frac{1}{J}\left(u_j - \frac{\partial x_j}{\partial \tau}\right)\frac{\partial \phi_i}{\partial \xi^k} \tag{2.44}$$

where J and b_i^j are Jacobian and transformation matrices, respectively.

The second order finite Euler backward difference scheme is used to discretized temporal terms.

$$\frac{\partial \phi}{\partial t} = \frac{1}{\Delta t}\left({}^{3}/_{2}\,\phi^n - 2\,\phi^{n-1} + {}^{1}/_{2}\,\phi^{n-2}\right) \tag{2.45}$$

where ϕ is the general variable. For the spatial discretization, second-order upwind for RANS or fourth-order upwind biased for DES and DDES schemes are used for the convective terms.

The mass conservation is enforced by a strong pressure/velocity coupling, using projection algorithms.

Non-linear iterations are performed within each time step to properly couple turbulence, level set, motions and the non-linear convection terms in the momentum equations and the object motions. At the beginning of a non-linear iteration REX obtains the overset connectivity information for the grids through receives of the information sent by the SUGGAR processors based on the latest motions of the grids which provided by the flow solver. Once this is done and the grids are moved to the current position, turbulence and level set are solved using the latest velocity available. Then the velocity is solved implicitly, the pressure matrix is assembled and the pressure solved. Afterwards the velocity is updated with the new pressure field to obtain a solenoidal velocity field. In a projection scheme the non-linear iteration is complete, but if a PISO algorithm is used to

couple pressure and velocity then some iterations are needed. Once the flow field for the non-linear iteration is obtained, forces and moments are computed. If the residuals for the non-linear loop are acceptably small (typically 10-3) then the solution is converged for the time step and the motions for the next time step are predicted. With the new motions available SUGGAR can initiate computation of the DCI for the new grid position. If the time step did not converge the motions are corrected and SUGGAR is started for the new non-linear iteration.

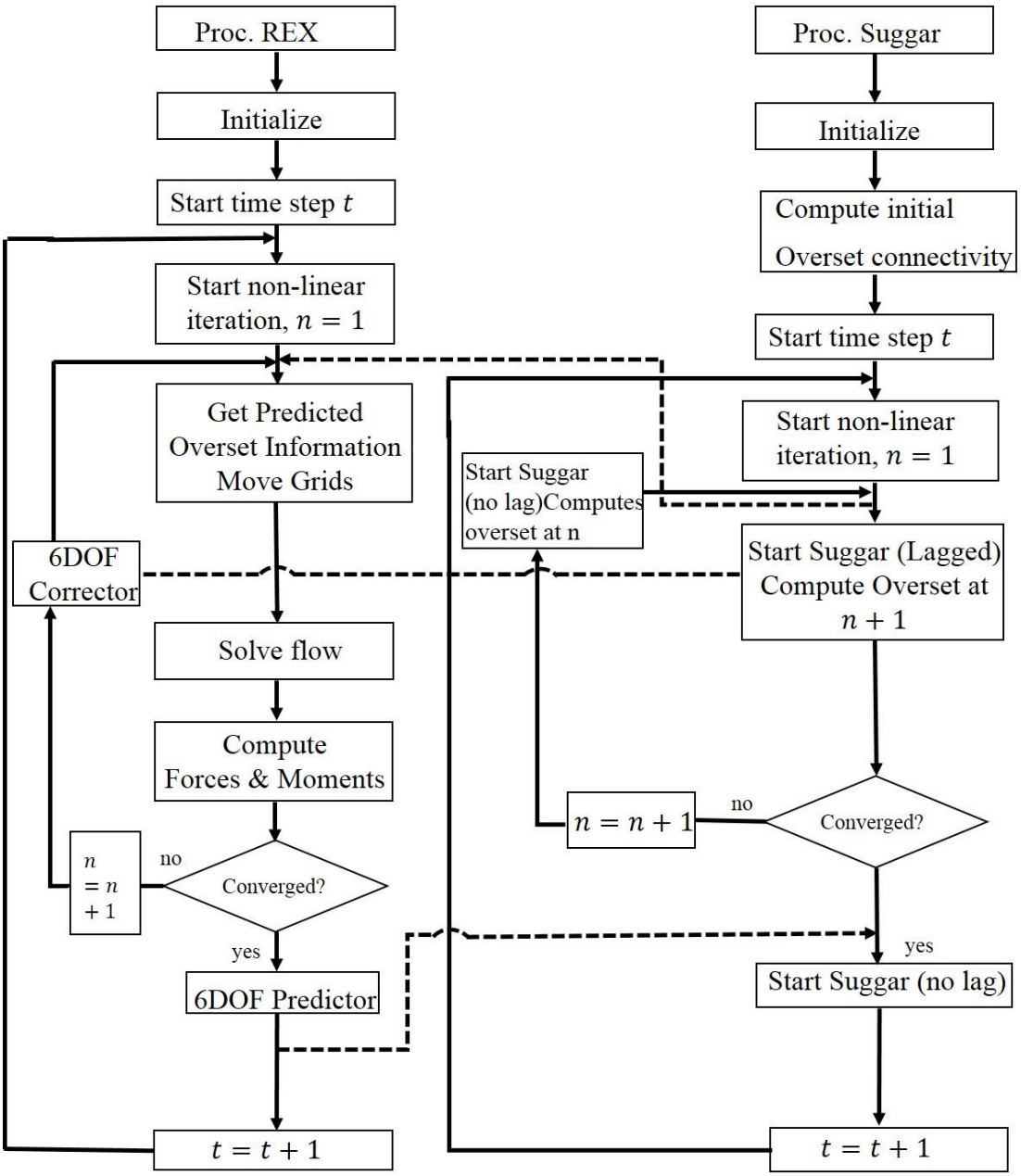

Figure 2.3 Flow chart depicting exchanges between REX and Suggar in no lagged and lagged mode as described in Carrica et al. (2010b).

CHAPTER 3

DIRECT SIMULATIONS OF ZIGZAG MANEUVER FOR A CONTAINER SHIP IN DEEP WATER

3.1 Overview

In this chapter the simulations of zigzag maneuvers of the Potsdam Model Basin (SVA) Korean container ship (KCS) model with moving rudder and rotating propeller are presented. The discretized propeller approach is used for propulsive computations. To overcome the difficulties of simulating the moving semi-balanced horn rudder which characterizes by extremely tight gaps between with the fix part and moving part of the rudder, the dynamic overset technique with a hierarchy of bodies is used. A Delayed Detached Eddy Simulation turbulence model based on Menter's SST is used in order to resolve propeller/rudder interaction with more resolution. The standard 10/10 zigzag maneuver and the modified 15/1 zigzag maneuver are considered for simulations. Both simulations are performed at model scale in deep, calm water, for approach velocities corresponding to a Froude number 0.26. To achieve self-propulsion condition at approach speed of 24 knot a PI speed controller is used. The controller acts on the propeller rotational speed while the ship is free to surge, heave, roll and pitch. Once the ship achieves self-propulsion the propeller rotational speed is fixed and the ship is free to start move in 6DOF while the maneuver starts.

Notice that most studies for free maneuvering predictions use a prescribed body force propeller; in most cases control surfaces such as rudders are replaced by side forces and in some cases instead of using real moving rudder, fixed rudders are used. These

simplifications are undesirable because the propeller-rudder interactions and capturing propeller vortical structures will be ignored while they may have significant effects on maneuvering performance.

3.2 Simulation Design

3.2.1 Geometry and Simulation Conditions

KCS is a container ship developed by the Korean Maritime and Ocean Engineering Research Institute (MOERI) in Korea. Figure 3.1 shows the views of ship model and its geometry, and main particulars of the model are listed in Table 3.1. All variables in this chapter are non-dimensionalized using a reference velocity U_0 taken to be the ship service speed and a length scale taken to be the length between perpendiculars L_{pp}. The simulation conditions are defined based on the two dimensionless numbers: the Reynolds number $Re = \frac{U_0 L_{pp}}{\upsilon}$ and the Froude number $Fr = \frac{U_0}{\sqrt{g L_{pp}}}$, where υ is the kinematic viscosity of water and g is the acceleration of gravity. Therefore, the dimensionless propeller rotational speed, forces and torque are $n^* = \frac{n L_{pp}}{U_0}$, $F^* = \frac{F}{\rho U_0^2 L_{pp}^2}$ and $M^* = \frac{M}{\rho U_0^2 L_{pp}^3}$, respectively, where ρ is the water density.

For both 15/1 and 10/10 zigzag maneuver simulations, the Reynolds number at the nominal approach speed of 24 knots (in self-propulsion) is 7.51×10^6 in model scale, corresponding to a Froude number of 0.26. The reference coordinate system is defined as: x the longitudinal axis pointing to stern, y pointing to starboard and z pointing upwards with $z = 0$ at calm water line. At initial condition and when the ship is at rest the Earth

system is coincident with the Ship system. All flow equations are solved in Earth system and computations are performed based on these equations.

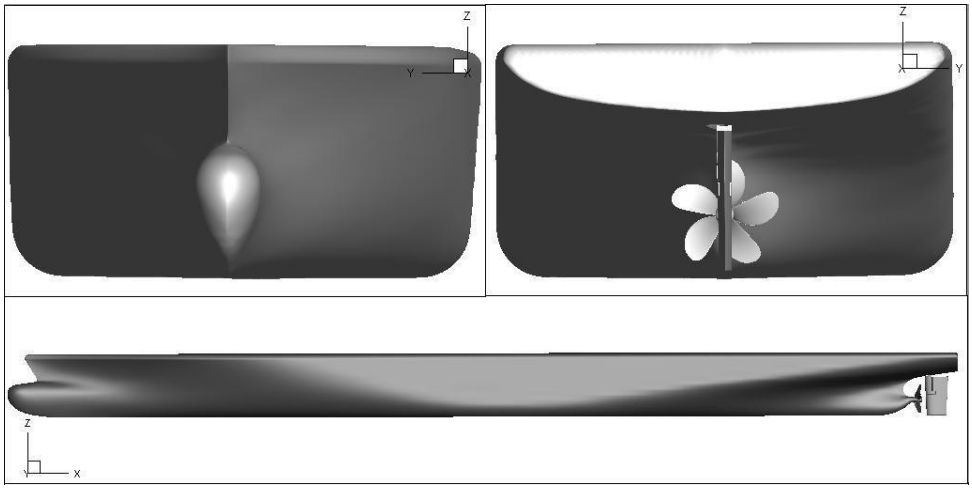

Figure 3.1 Fully appended KCS geometry.

Table 3.1 : Main particulars of the KCS model.

Main Particulars		**Full Scale**
Length of waterline	$L_{wl}(m)$	232.5
Length between perpendiculars	$L_{pp}(m)$	230.0
Maximum beam of waterline	$B_{wl}(m)$	32.2
Draft	$T\ (m)$	10.8
Depth	$D\ (m)$	19.0
Displacement*	$\Delta\ (m^3)$	52030
Block coefficient (CB)	$\Delta/(L_{pp}B_{wl}T)$	0.6505
Longitudinal Center of Gravity	$L_{CG}(m)$	118.4
Wetted area $\boldsymbol{w/o}$ rudder	$S_w(m^2)$	9424
Midship section coefficient (CM)		0.9849
Vertical center of gravity (from free surface)	$Z_{CG}\ (m)$	3.346/2.846
Metacentric height	$GM\ (m)$	0.6/1.1
Moment of inertia	K_{xx}/B	0.40
Moment of inertia	$K_{yy}/L_{pp}, K_{zz}/L_{pp}$	0.25
Propeller center, long. Location (from FP)	x/L_{pp}	0.9825
Propeller center, vert. location (below WL)	$-z/L_{pp}$	0.02913
Service speed (knots)	U	24
Froude number	Fr	0.26

For the 15/1 modified zigzag maneuver (Case 1) the center of gravity is such that the metacentric height is $0.6\,m$, corresponding to a vertical location of the center of gravity of $3.346\,m$. For the 10/10 standard zigzag maneuver (Case 2) the metacentric height is $1.1\,m$, for a vertical location of the center of gravity of $2.846\,m$. Following the experimental conditions for Cases 1 and 2, the propeller from SVA is used for providing propulsion. The propeller is a 5 bladed, variable pitch design with diameter $7.9\,m$. Table 3.2 summarizes the propeller's principal particulars, showing that for the cases in this thesis the pitch to diameter ratio is 0.997. The details of the rudder is provided in Table 3.2 as well. The rudder type used for both simulations is a semi-balanced horn rudder with a maximum turning rate of 2.32 degrees/s in full scale.

Table 3.2: Details of propeller and horn rudder.

Model	**Full Scale**	**SVA**
Scale	1.000	52.667
Propeller		
Type	FP	CP
No. of Blades	5	5
D (m)	7.9	0.150
P/D (0.7R)	0.997	0.700
Rotation	Right Hand	Right Hand
Hub Ratio	0.180	0.227
A_e/A_0	0.800	0.700
Rudder	Semi-balanced horn rudder	
S rudder (m^2)	115	0.0415
Lat. Area (m^2)	54.45	0.0196
Turn rate (deg/s)	2.32	16.8

3.2.2 Geometries and Grids

The KCS overset grid topology is shown in Fig. 3.2. The cross sections exhibiting the refinements at free surface and propeller/rudder region. The overset grid system consists of 38 grid blocks, including grids for hull, propeller, rudder, refinements and

background. These 38 blocks are distributed in 168 processors and listed in Table 3.3. The total number of grid points is 24.6 million. 70% of the total grid points belong to refinement blocks to resolve the flow around the propeller and rudder and on the wake to resolve vortical structures and flow features in those regions, and better capture the hull/propeller/rudder interactions critical to predicting maneuvering forces and moments. In order to obtain appropriate overlapping at the gap between the rudder's horn and moving part of the rudder and also at the zone between propeller blades and the rudder, fine enough grids are required to obtain valid interpolations between overset grids.

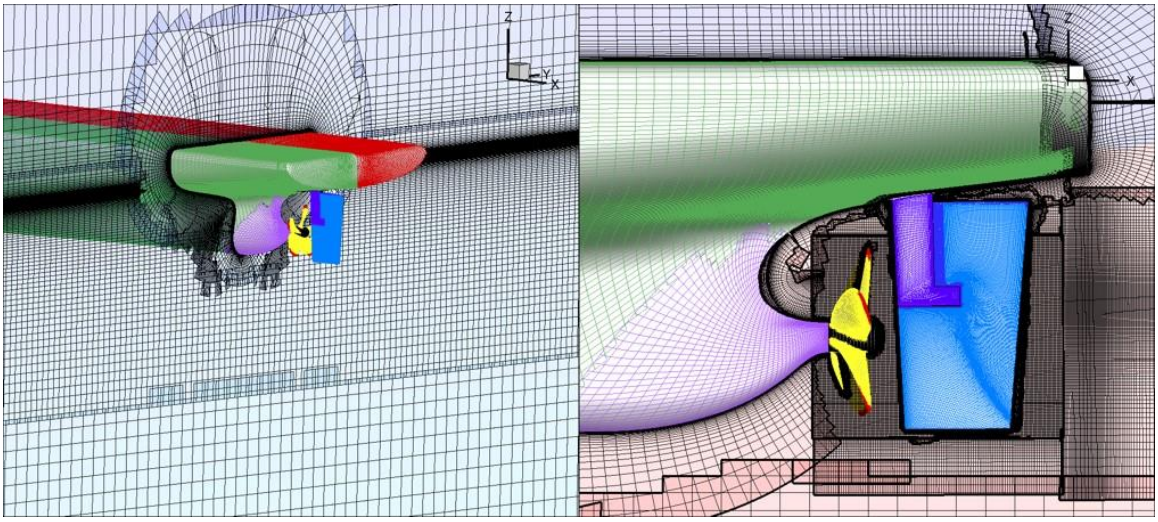

Figure 3.2 Overset grid topology.

Propeller and rudder grids are handled using overset grids. The commercial grid generation software Gridgen is used to generate volume grids from each surface grids which conformed to the appendages. Grid spacing on solid boundaries is designed to handle boundary layers up to $Re = 20 \times 10^6$ with the Shear Stress Tensor (SST) turbulence model integrating all the way to the wall.

The hierarchy of bodies used to run the simulation is shown in Table 3.3. The ship body is solved as a rigid body in 6DoF, and contains all grids defining the geometry and the refinements that follow the ship in all degrees of freedom. Rudder and propeller grids are children to the ship, and move according to the control laws for these appendages. All propeller grids rotate together as a rigid body with one degree of freedom, the rotational angle controlled by the speed controller. These propeller grids form a dynamic overset group for which overset interpolations between members are computed only once at the beginning of the run. The rudder is constructed similarly and forms a second dynamic overset group, with rudder angle controlled by the zigzag controller. A third dynamic overset group is formed by all ship and refinement grids belonging to the ship body excluding the rudder and propeller. Finally, the grids connecting the ship to the far-field boundary conditions, called Background and Refinement grids in Table 3.3, follow the ship but are not allowed to pitch, heave or roll so that the refinements in these grids, designed to resolve the free surface, stay horizontal. The simulations were conducted using 3 Suggar groups.

After generating the grids and setting up inputs and boundary conditions, the overset connectivity code Suggar is used to obtain the overset domain connectivity between overlapping grids. Once the valid interpolations is achieved (no orphan points) for different propeller and rudder angles, Usurp (Boger and Dryer 2006) is ran to obtain the information of overset panels for force integration.

Table 3.3: Details of the grids and decomposition information.

Grid	Size	Grid Points	Belongs to body	Processors
Boundary layer starboard 1	244×55×89	1179 K	Ship	8
Boundary layer starboard 2	241×58×53	740 K	Ship	5
Stern starboard	61×48×51	149 K	Ship	1
Hub starboard	71×41×51	148 K	Ship	1
Boundary layer port1	241×55×89	1179 K	Ship	8
Boundary layer port2	241×58×53	740 K	Ship	5
Stern port	61×48×51	149 K	Ship	1
Hub port	71×41×51	148 K	Ship/Propeller	1
Propeller hub	101×32×91	294 K	Ship/Propeller	2
Propeller blades	5×79×51×74	5x298 K	Ship/Propeller	10
Propeller tips	5×51×41×71	740 K	Ship	5
Refinement wake	79×136×135	1450 K	Ship	10
Refinement	241×142×101	3456 K	Ship	24
Background	181×141×91	2322 K	Ship	16
Rudder stem refinement	61×45×109	299 K	Ship	2
Rudder stem starboard	61×55×89	298 K	Ship	2
Rudder stem port	61×55×89	298 K	Ship	2
Rudder stem top	55×45×61	150 K	Ship	1
Rudder stem bottom	119×41×61	297 K	Ship	2
Refinement gap top	26×103×55	147 K	Ship	1
Rudder gap	73×35×175	447 K	Ship/Rudder	3
Rudder top	113×36×37	150 K	Ship/Rudder	1
Rudder starboard	211×47×89	882 K	Ship/Rudder	6
Rudder port	211×47×89	882 K	Ship/Rudder	6
Rudder cap top	71×41×51	148 K	Ship/Rudder	1
Refinement propeller/rudder	201×172×151	5220 K	Ship	36
Refinement rudder bottom	121×117×21	297 K	Ship	2
Refinement rudder port	117×21×121	298 K	Ship	2
Refinement rudder starboard	117×21×121	297 K	Ship	2
Refinement rudder top	117×121×21	297 K	Ship	2
Total		24.6 M		168

In order to find the longitudinal location of the center of gravity, the static wetted area and the mass of the ship, a pre-processing hydrostatic computation is performed with code REX in static condition with zero resulting pitching moment and weight balancing buoyancy. Though these values are usually provided for design conditions, CFD values can deviate a small amount (typically less than 0.1%) due to the fact that the geometry was discretized. Table 3.4 shows the CFD and EFD results for hydrostatic conditions. The

resulting dimensionless values for longitudinal location of the center of gravity, mass and static wetted area are 0.509825, 0.679849 and 0.180419, respectively.

Table 3.4 Hydrostatic results of KCS in full scale.

Parameter	CFD	EFD
Displacement (m^3)	51543	51978
Longitudinal Center of Gravity (m)	118.5	118.4

3.3 Self-Propulsion

Before starting the standard maneuvering simulation, the ship requires to reach self-propulsion condition at the approach speed. Once the self-propulsion condition is achieved, then the maneuver can start with constant propeller rotational speed (RPS) or torque. Since the experimental results report constant RPS for maneuvering so the constant RPS is used in simulations as well.

Typical self-propulsion tests are conducted in a model captive to the carriage of a towing tank. The net towing force is measured when the experiments are run for a certain target speed at different propeller rotational speeds. The goal is to obtain the propeller rotational speed which zeroes the towing force by balancing propeller thrust with total resistance which is the necessary condition for self-propulsion. Implementing similar approach in computational fluid dynamics results in high computational cost and requires several runs at different propeller rotational speed to achieve the self-propulsion point and shows this method is not a very efficient approach. An alternative method proposed by Carrica et al. (2010a) is used in this thesis. This method is based on a PID-type speed

controller that varies the propeller RPS to achieve the target Froude number and a single run is adequate for self-propulsion computation.

The dimensionless proportional and integral constants were set to 60 and 40, respectively. The dimensionless target speed was set to 1 (24 knots at full scale) and the initial dimensionless RPS was set to 45 (corresponding to 143 RPM in full scale), with maximum and minimum set to 45 and 25 (80 RPM in full scale), respectively. The dimensionless time step was set to $\Delta t = 0.00025$, which corresponds to approximately 3.3 degrees of propeller rotation per time step at self-propulsion condition. It took approximately 160 hours of wall clock time to achieve self-propulsion.

The self-propulsion computations are performed with a nonzero initial propeller RPS and ship motions are free to surge, heave, roll, and pitch and restrained from yaw and sway motions. Rudder motions are also imposed to straight condition in controller. In free models a perfect straight ahead condition will result in some level of roll, yaw, sway and drift, which have been neglected in this work. A wide range of initial conditions for the different zigzag maneuver runs are examined to estimate the symmetry of the ship and possible initial values of roll, yaw, sway, and drift which don't show a clear trend on the self-propulsion values of roll, yaw, sway and drift.

KCS is a very long and heavy ship with the low propulsion to weight ratio, so it would take a long time to achieve self-propulsion due to the high inertia of the model. In order to compensate the high inertia effect and achieve faster convergence to self-propulsion the surge rigid motion equation is modified to reduce the inertia by a factor of 20, allowing much faster convergence to self-propulsion with the final result unaffected since the inertia term goes to zero in steady state.

The time history of the propeller rotational speed and the ship velocity is shown in Fig. 3.3. Self-propulsion at the target speed of 24 knots is achieved for a propeller rotational speed of 118 RPM in CFD compared to the experimental value of 116.1 RPM. Notice that for all cases reported in Steinwand (2006) with nominal approach speed of 24 knots the actual approach speed was slightly lower in average that the target speed at 23.7 ± 0.5 knots, using only the standard deviation to compute the 95% uncertainty in the data. In all cases the propeller rotational speed was 116.1 RPM. Assuming constant thrust and resistance coefficients, and increase from 116.1 RPM to 117.6 RPM would be necessary in the experiments to increase the speed from 23.7 to 24 knots.

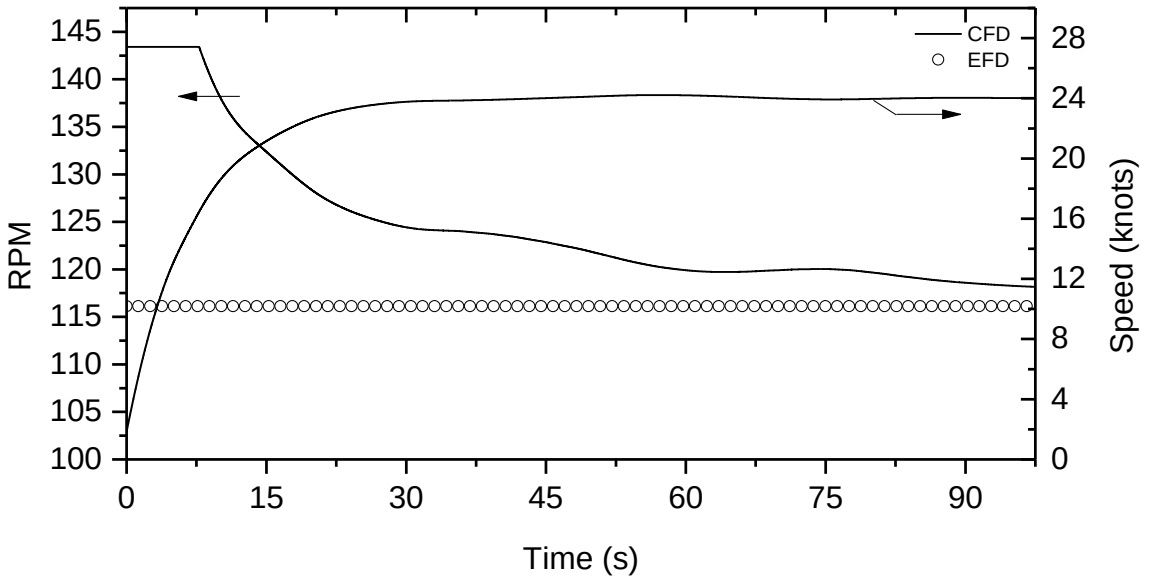

Figure 3.3 Time history of ship speed and propeller rotational speed for self-propulsion computation.

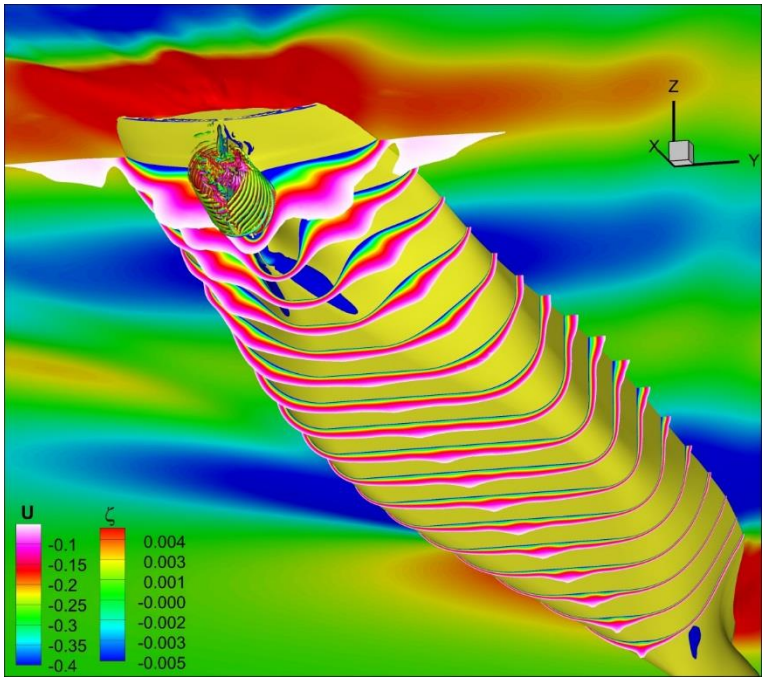

Figure 3.4 Free surface elevation and cross sections showing the boundary layer at self-propulsion.

Fig. 3.4 depicts a view of the flow field at self-propulsion, which shows cross sections at constant x planes colored with velocity and free surface colored with elevation. The cross sections showing the development of the boundary layer during the self-propulsion. Isosurfaces of the second invariant of the rate of strain tensor $Q = 20000$ colored with velocity are shown in Fig. 3.4. The thickening of the boundary layer at the stern due to the adverse pressure gradient, where the hull contracts to leave room for the propeller and rudder is clear, with a resulting wake factor $1 - W_T = 0.8$ and a nominal wake $W_n = 0.723$ (Carrica et al. 2010b).

3.4 Direct Simulation Results and Discussion

3.4.1 Zigzag Maneuvers

In this section the results for standard 10/10 zigzag maneuver and modified 15/1 zigzag maneuver are presented. Same grid setup and time step are used for both simulations. In this thesis a validation and verification study is performed for the first time for free running ship maneuver in shallow water and results will be presented later in Chapter 4.

The zigzag maneuvers are started from the self-propulsion condition and simulations are conducted with a zigzag maneuver controller. In maneuvering conditions ship is free to move in six degree of freedoms and rudder executes according to a rudder controller that limits the rudder rate to the experimental value and changes rudder direction according to the check heading specified in the maneuver. As discussed in section 3.3, the propeller RPS is retained constant at the self-propulsion value for the whole maneuver. For the 15/1 modified zigzag maneuver a total of 75000 time steps with $\Delta t = 0.00025$ were used which took about 500 wall clock hours and it resulted in approximately two periods of the maneuver. For the standard 10/10 zigzag maneuver 44000 time steps with $\Delta t = 0.00025$ were used and it took about 290 wall clock hours to complete the maneuver.

The standard zigzag maneuver as recommended by ITTC (2002), measures the maneuverability of a ship by obtaining the main parameters of the maneuver, the overshoot angle of the ship (the excess angle between the maximum ship's heading and the check heading angle), the maximum yaw rate and the period (time to complete a cycle). The modified zigzag maneuver is similar to the standard zigzag maneuver but the check angle

is very small, typically one degree, to evaluate course-keeping qualities. The typical standard zigzag maneuver is expressed according to ITTC (2002). The maneuver is achieved by turning the rudder alternately by a given degrees to either side at a deviation yaw angle from the initial course. For example in 10/10 maneuver after the self-propulsion is obtained with zero rudder angle and at approach speed, the rudder is deflected to 10 deg. to port or starboard and holds until the ship turns 10 deg. Then rudder is deflected 10 deg. to the other side and holds until the ship turns 10 deg. or -10 deg. This process continues until a total of 5 rudder executes have been completed. Fig. 3.5 displays key parameters in standard zigzag maneuver.

For all the following discussions on maneuvering results the coordinate system is defined as: positive yaw when ship heads to starboard, positive rudder angle when turning to starboard. Positive pitch when ship bows up, and positive roll angle when ship rolls to port.

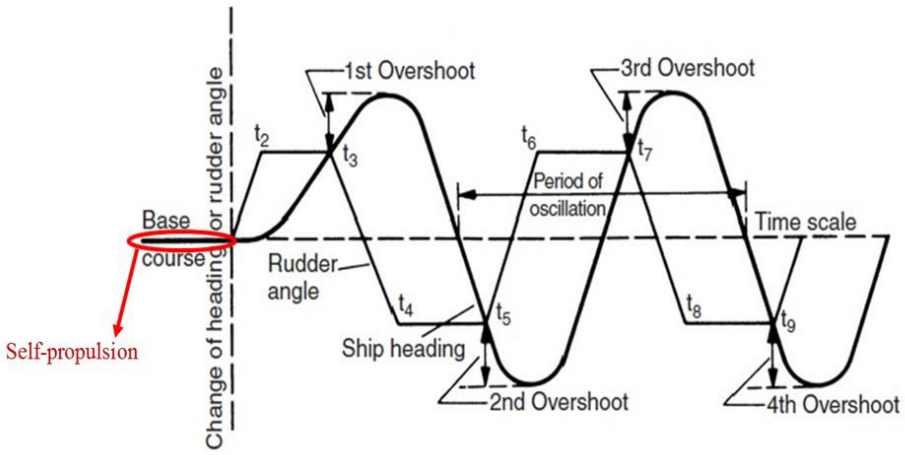

Figure 3.5 Standard zigzag maneuver, ITTC 2002.

3.4.2 Motion Variables in Zigzag Maneuver

Figures 3.6 and 3.7 illustrate the time histories of yaw, yaw rate and rudder angle for the 15/1 modified maneuver and the 10/10 standard maneuver, respectively. The agreement between CFD predictions and EFD measurements is very good in terms of time to check yaw, period and reach, with some underestimation of the yaw rate and thus the overshoot. In contrast with CFD, EFD initial conditions contain some degrees of yaw and yaw rate, so it is hard to make valid comparisons using the start time of the maneuver as the zero for both CFD and EFD, since in both cases conditions are different. Instead the time is measured from the start of the CFD maneuver and the EFD results are synchronized at the beginning of the rudder execute at 104 s in Fig. 3.6 and at 133 s in Fig. 3.7. In both cases these times are corresponding to the first execute of rudder from port to starboard. This is valid approach since the differences in initial conditions between CD and EFD are already damped at this stage of the maneuver.

As can be seen in Fig. 3.6 for the 15/1 maneuver, after 4th rudder execute, the yaw and yaw rate reach periodic condition, though results of ship velocity show that the periodic condition has not been reached. Ship speed results will be discussed in section 3.4.3. Note that the experimental data has a starting yaw rate of 0.03 degrees/s, which causes some level of drift of the data towards starboard. Conversely, the CFD yaw rate is exactly zero at the beginning of the simulation since the self-propulsion computation used to obtain the approach speed was restricted from any yaw motion. The maximum and minimum yaw rates are marked with points (a) and (b) in Fig. 3.6, respectively, and reach absolute values of 0.85 degrees/s and 0.895 degrees per second for CFD and EFD, respectively. All critical maneuvering parameters are summarized in Table 3.5.

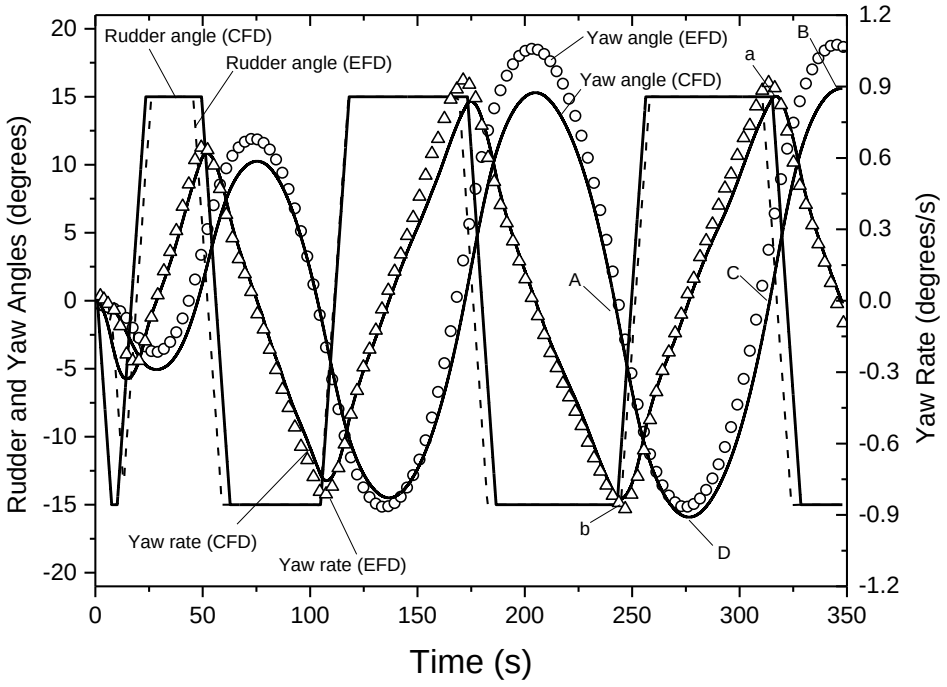

Figure 3.6 Yaw and rudder angles and yaw rate for 15/1 modified zigzag maneuver. (A) and (C): 0 yaw points, (B) and (D): maximum and minimum yaw points, respectively. (a) and (b) maximum and minimum yaw rate, respectively.

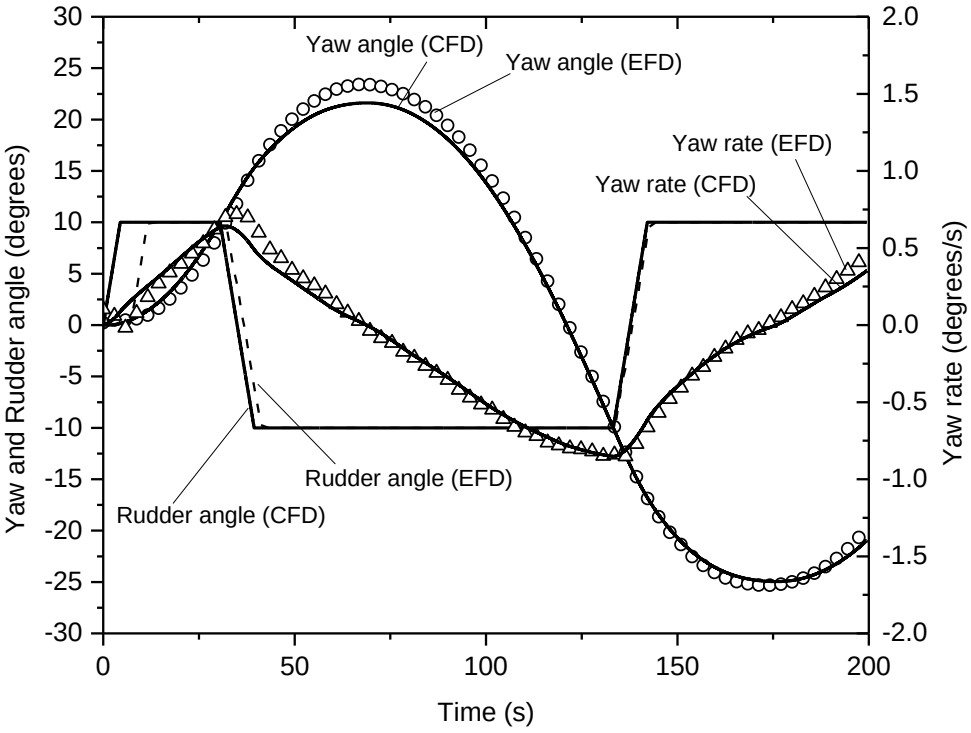

Figure 3.7 Yaw and rudder angles and yaw rate for 10/10 standard zigzag maneuver.

In Fig. 3.6, points A and C represent zero yaw angles when the ship turns from starboard to port and port to starboard respectively. The maximum and minimum yaw angles are labeled B and D, respectively. Notice that comparison of maximum and minimum yaw is difficult because of the drifting to port of the EFD model (to positive yaw), but average between maximum and minimum results in a peak in yaw of 15.8 degrees for CFD and 16.7 degrees for EFD, indicating an overshoot of 14.8 degrees and 15.7 degrees for CFD and EFD, respectively. CFD under-predicts the overshoot then by 5.7%. The period predicted by CFD is 141.9 s, very close to the experimental period of 141.2 s. Finally Table 3.5 shows the time for the first and third execute. Variations in initial conditions for yaw and yaw rates cause significant differences in the time for the first

execute, as can be seen in Fig. 3.6 and Table 3.5, as high as 54%. By the time the third execute is reached the initial conditions have been overcome by the transients of the maneuver and the error in time for the execute decreases to 6.5%. Since the EFD and CFD periods are very close, the error in time to execute decreases almost linearly reaching 3.4% for the sixth execute.

Table 3.5 Parameters for the 15/1 modified zigzag maneuver.

	First Execute (s)	**Third Execute (s)**	**Period (s)**	**Overshoot Angle (deg)**	**Yaw Rate $(\dot{\psi}_{max} - \dot{\psi}_{min})/2$ (deg/s)**
EFD	6.6	98.1	141.2	15.7	0.895
CFD	10.2 (+54%)	104.5 (+6.5%)	141.9 (+0.5%)	14.8 (-5.7%)	0.85 (-5%)

Table 3.6 Parameters for the 10/10 zigzag maneuver.

	First Execute (s)	**Second Execute (s)**	**Period (s)**	**Overshoot Angle (deg)**	**Yaw Rate $(\dot{\psi}_{max} - \dot{\psi}_{min})/2$ (deg/s)**
EFD	34.8	126.6	212.2	15.32	0.786
CFD	39.6 (+14%)	133.5 (+5.4%)	213.1 (+0.4%)	14.96 (-2.4%)	0.747 (-5%)

Figure 3.7 shows the time histories of yaw, yaw rate, and rudder angles for the 10/10 standard maneuver. The experimental data is presented for 200 s of full scale time, and thus computations were conducted only for that period. The trends are similar to those observed for the modified zigzag maneuver, but the overshoot angle error decreases to 2.4%. The errors are comparable to other integral computational ship hydrodynamics

results, typically within 3~5% of experimental data for resistance and self-propulsion computations. Table 3.6 summarizes the 10/10 maneuvering variables.

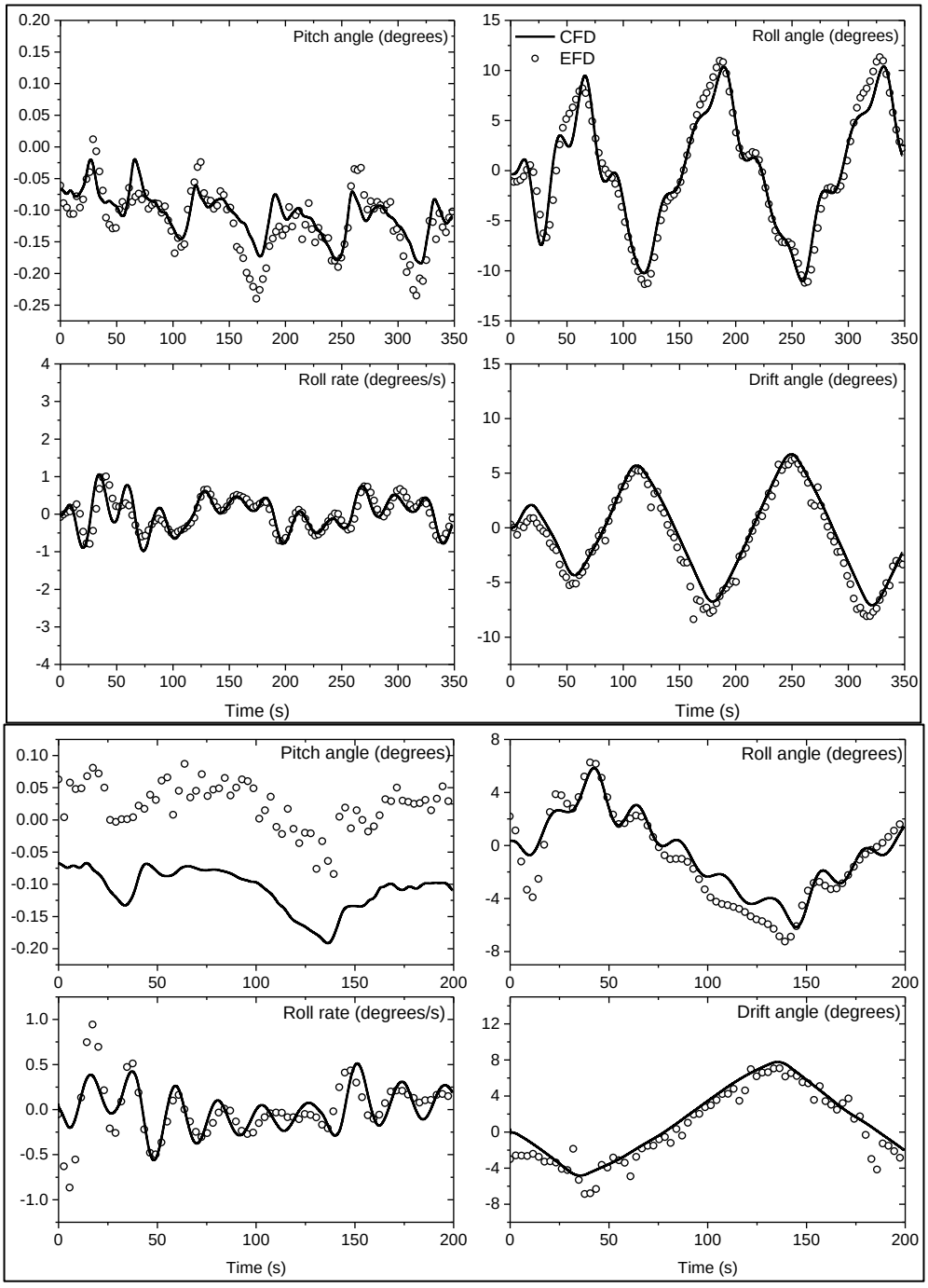

Figure 3.8 Pitch, roll and drift angles and roll rate for 15/1 (top 4 plots) and 10/10 (bottom 4 plots) zigzag maneuvers.

Since this is the standard maneuver, so results can be compared against International Maritime Organization (IMO) standards. For the first overshoot the standard requires an overshoot of less than 14.31 degrees, with CFD predicting 11.6 degrees and EFD reporting 13.4 degrees, in both cases satisfying the IMO requirements. IMO requires for the second overshoot a maximum of 31 degrees, which is easily satisfied by CFD (14.96 degrees) and EFD (15.32 degrees).

Figure 3.8 depicts the roll rate, roll, pitch and drift angle for both maneuvers. The results for the 15/1 zigzag maneuver, showing good agreement with experiments for all variables, however the maximum roll angle is slightly under-predicted. It should be noted that, the pitch angles are very small but the trends are still consistent with experiments. The roll rate, related to the roll damping, is also very consistent with experimental data. The 10/10 zigzag maneuver results for pitch show CFD with small but negative pitch and EFD with small but positive pitch. Relative pitch motions respect to the pitch angle at approach speed are well predicted, but EFD pitch at approach condition ($t = 0$) is inconsistent with the value shown for the 15/1 maneuver for the same nominal conditions. All other parameters compare well with EFD, with the exception of roll and roll rate at the beginning of the maneuver, where data shows an initial condition with over 2 degrees of roll angle and a large initial roll rate.

3.4.3 Ship Speed, Forces and Moments

The time evolution of the ship speed for both maneuvers are shown in Fig. 3.9. The velocity of the ship decreases quickly as the maneuver progresses due to the added resistance by the rudder and turning of the hull. Although, there is some uncertainty on

how accurately the nominal approach speed has been achieved in EFD, CFD follows the behavior of EFD fairly well. For the 15/1 maneuver, every time the ship reaches peak roll angle the ship velocity decreases considerably, with a sharper speed loss when the ship rolls to port.

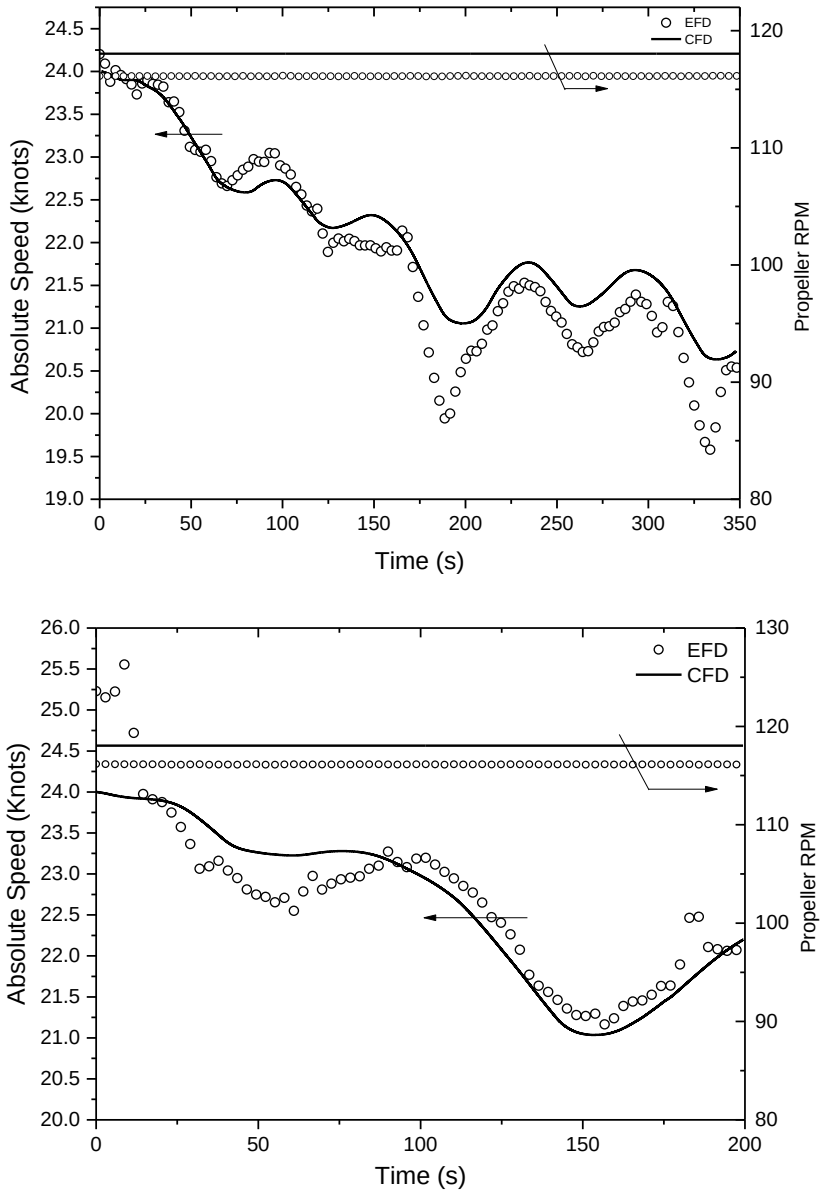

Figure 3.9 Ship speed and propeller RPM for 15/1 (top) and 10/10 (bottom) zigzag maneuvers.

The main discrepancies in speed between CFD and EFD For 10/10 maneuver are observed at the beginning of the maneuver with higher approach speed of 25.2 knots in experiment instead of nominal 24 knots.

The speed loss is also correlated with the drift angle, as expected, but the maximum speed loss occurs approximately 15 s after the drift angle reaches a minimum. This behavior, though captured in CFD, is particularly striking in EFD. The 10/10 maneuver also shows a stronger, though less evident, velocity decrease when rolling to port. In both maneuvers the zigzag has not reached periodic behavior, since the velocities are still dropping.

In contrast with the negative influence of the roll and drift motions on the speed loss which due to increase in the ship resistance during the maneuver, changes in propeller forces have an significant impact on increasing thrust as the velocity decreases and therefore, the local propeller advance coefficient decreases.

Figure 3.10 depicts the time histories of propeller thrust and torque for both zigzag maneuvers with excellent agreement between CFD and EFD. By decreasing the ship speed and consequently the local advance coefficient regression, the propeller average thrust shows increase during the maneuver. However, large low-frequency fluctuations occur, with increases in thrust and torque that correlate negatively with yaw rate. While this indicates that thrust and torque are maximum when the ship turns to port at maximum rate, it is also evidence of the asymmetries that a single screw propeller can cause, in this case with peak to peak fluctuations of 25% of the average thrust and torque. In addition, high frequency fluctuations in thrust and torque that correlate to the blade passage frequency are presented, clear both in CFD. The EFD data acquisition rate is not high enough to resolve

this blade passage frequency, presenting considerable aliasing, but the amplitudes appear to be reasonable close to the CFD predictions, with the exception of the thrust for the 10/10 maneuver. Thrust and torque fluctuations due to the passage of the blades through different regions of the wake and are described in detail in Castro et al. (2011).

Rudder resistance and yaw moment from CFD results for both maneuvers are shown in Fig. 3.11. Every time the rudder is executed there is a minimum in rudder resistance as the rudder crosses aligns with the flow. Otherwise the rudder resistance can reach 800 KN when operated to port in the 15/1 maneuver, about 20% of the thrust coming from the propeller. This significant resistance provides a major source of momentum loss that has a consequent speed loss as shown in Fig. 3.9.

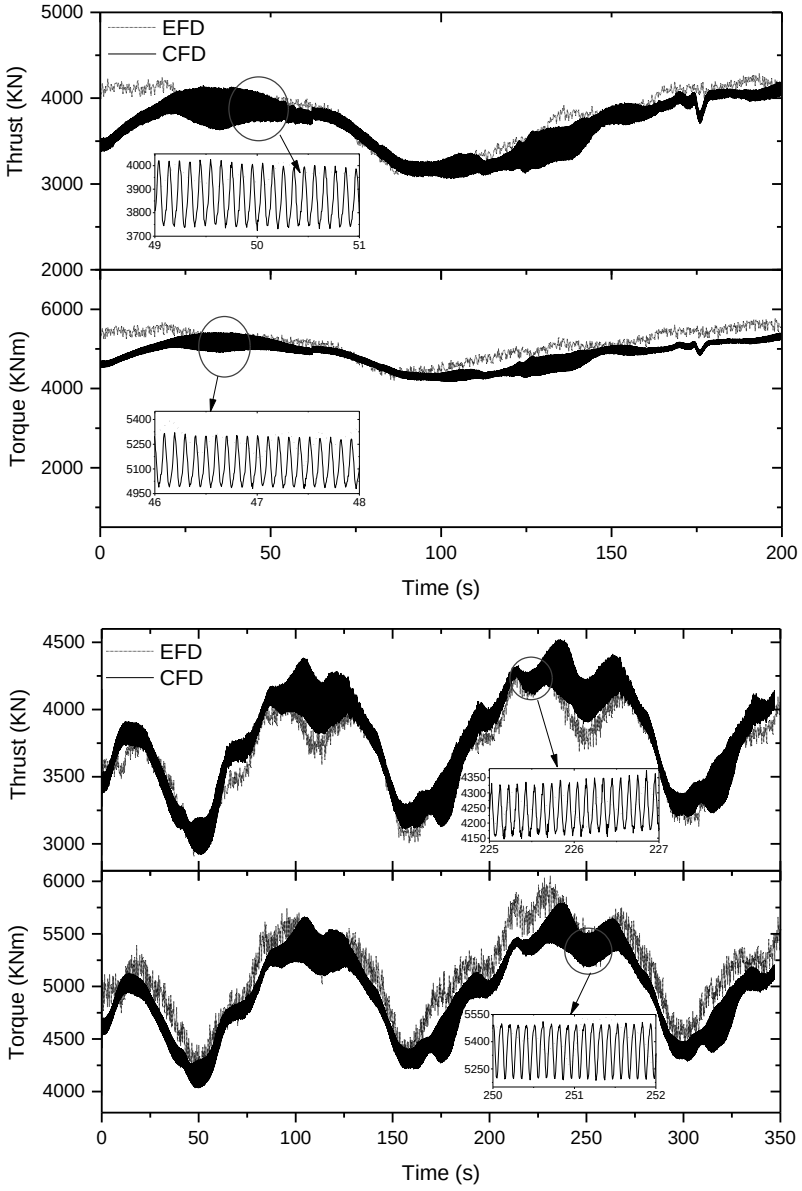

Figure 3.10 Propeller thrust and torque for 15/1 (top) and 10/10 (bottom) zigzag maneuvers.

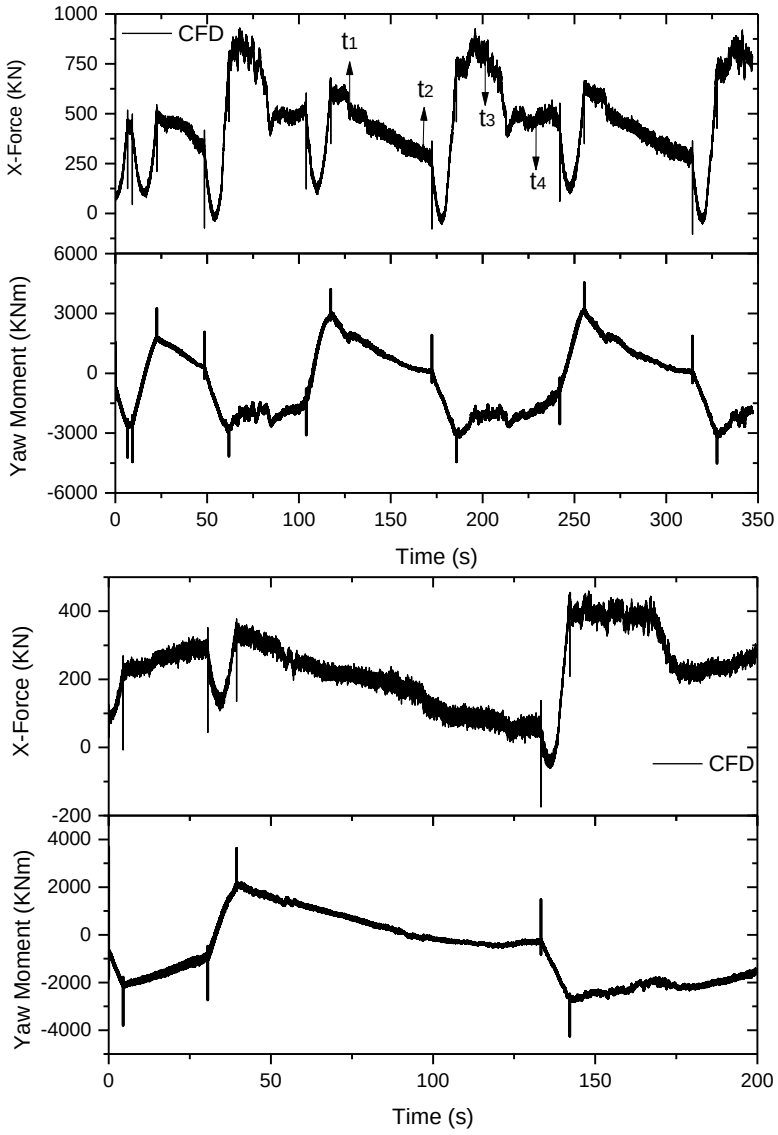

Figure 3.11 Rudder forces and moment for 15/1 (top) and 10/10 (bottom) zigzag maneuvers. On top figure $t_1 = 126\ sec, t_2 = 165\ sec, t_3 = 203\ sec$ and $t_4 = 233\ sec$.

Inspecting Figs. 3.9 and 3.11 for the 15/1 maneuvers, there is a strong correlation between speed recoveries in Fig. 3.9 and decrease in rudder resistance in Fig. 3.11 when the rudder is being executed. More strikingly, there is a correlation between strong velocity losses when the rudder is operated to port and peaks that are observed in rudder resistance

for these events. A close inspection to Fig. 3.11 reveals that the rudder resistance has a fairly smooth decrease from a maximum when the rudder is operated from port to starboard and kept at starboard (times t_1, t_2 at $126\ s, 165\ s$). In contrast, rudder forces are much higher when the rudder is operated from starboard to port and as is kept at port (times t_3, t_4 at $203\ s, 233\ s$) it suffers a transition with a sudden decrease of resistance. The significant drops in ship speed discussed in section 3.4.3 can possibly be explained by this large increase in resistance. This would mean also that CFD can only partially capture this effect, since the predicted decrease in speed is significantly less than the experimental observations. The peak observed in rudder resistance can be explained by increased angle of attack with the rudder to port and flow separation.

Figure 3.12 shows the flow around the rudder as streamlines on horizontal cross sections at three depths corresponding to 70% of the propeller radius above the propeller hub, at the propeller hub and 70% radius below the propeller hub. At the end of each rudder execute the angle of attack of the rudder is maximum (times t_1 to starboard and t_3 to port), and separation is observed for both rudder to starboard or port at hub height. At this location the angle of attack is much higher when the rudder is actuated to port than when is at starboard, and separation is much more violent. Above the hub, the angle of attack is much smaller with the rudder to starboard, since the swirl caused by the right-handed propeller tends to cancel the drifting flow coming from starboard as the ship still has a yaw rate to port. The opposite occurs when the rudder is executed to port, with the

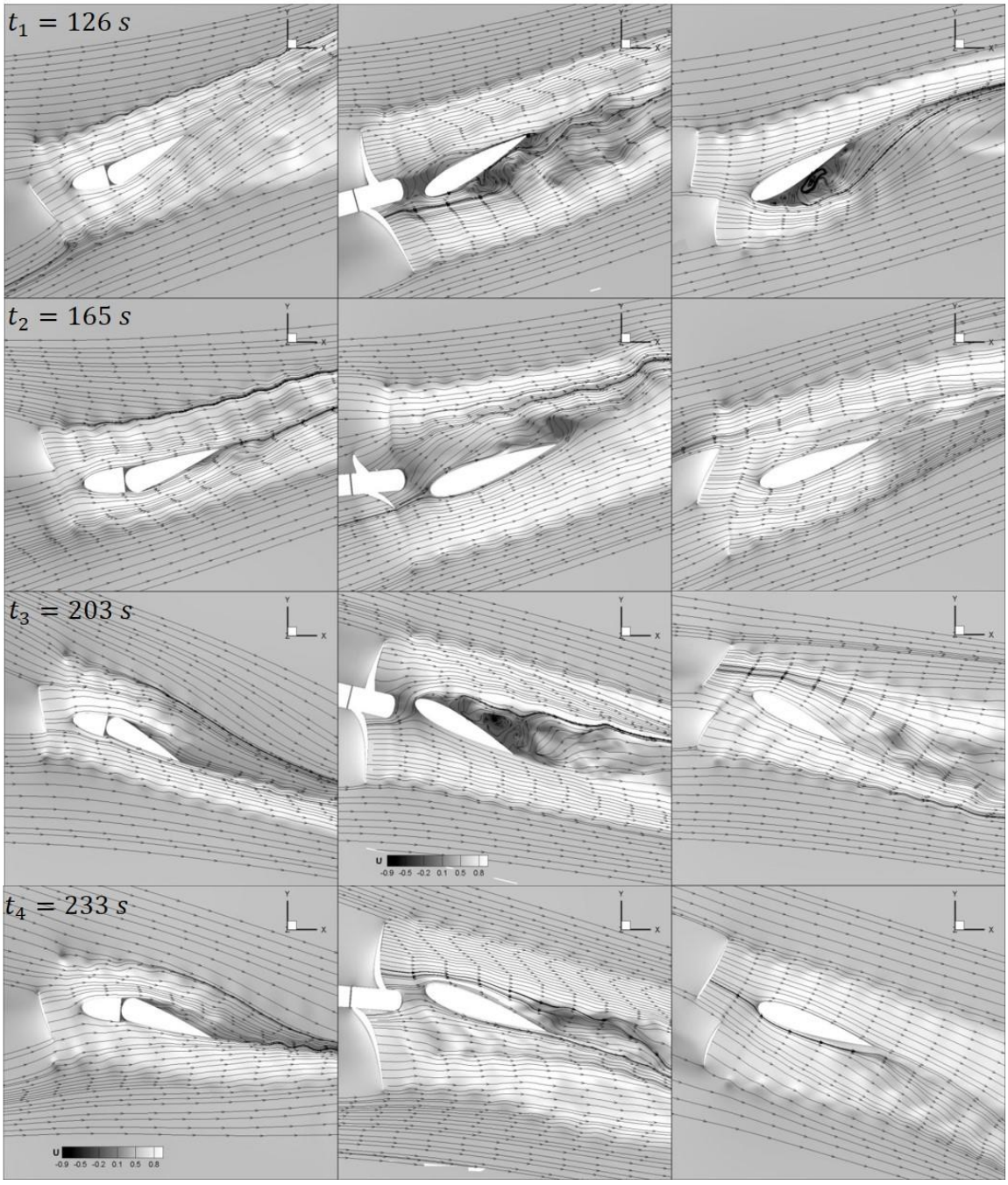

Figure 3.12 Streamlines around the rudder at different sections of rudder, r/R=0.7 (left), r/R=0 (center), r/R=-0.7. Times $t_1 - t_4$ are indicated in Fig. 3.11.

propeller-induced swirl and the lateral velocity acting in the same direction and increasing the angle of attack. The analysis is inverted for the cross section below the propeller hub.

In that location the angle of attack is higher when the rudder is in the starboard position with the swirl and the lateral velocity acting on the same direction. Once the ship changes yaw rate to align with the rudder direction the angle of attack decreases and so does the resistance, with the flow showing moderate or no separation. The same behavior is observed for the 10/10 maneuver. The yaw moment shows a slight but clearly noticeable decrease when separation occurs to port, indicating a reduction in rudder efficiency. Of interest is also the predicted increase on force and moment unsteadiness when separation occurs, which implies increased vibration when the rudder is actuating to port.

3.4.4 Flow Field in Zigzag Maneuver

Though experiments are invaluable and for many applications cannot be replaced by CFD, CFD is undeniably attractive to provide analysis and visualization of the flow. Figure 3.13 shows the free surface colored with axial ship velocity for the 15/1 maneuver at four instants during the maneuver corresponding to zero yaw crossing from starboard to port and port to starboard, and for maximum and minimum yaw. It is clear that the velocity at the free surface presents the expected low velocity ship wake extending close to the ship, but farther out the high-speed wake of the propeller reaches the free surface. This is particularly true for positive yaw with the propeller turned to port (Fig. 3.13B), where the interaction of the propeller wake with the rudder send high-speed flow closer to the free surface. A closer look at the interaction of the propeller wake with the rudder is provided in Fig. 3.14, which shows isosurfaces of $Q = 20000$ for points C (zero yaw) and D (minimum yaw) in Fig. 3.6, where the rudder is 15 degrees to starboard. Since the propeller is right handed (rotates clockwise looking forward from the stern), the induced swirl in the

propeller wake induces an upward flow on the port side of the rudder and downward on the starboard side. This is clear in the cross section downstream of the rudder in Fig. 3.14C. Also of notice is the highly fragmented vortical system coming from the propeller hub, formed by interaction of the mostly axially swirling hub vortex with the necklace and trailing vortices produced by each blade.

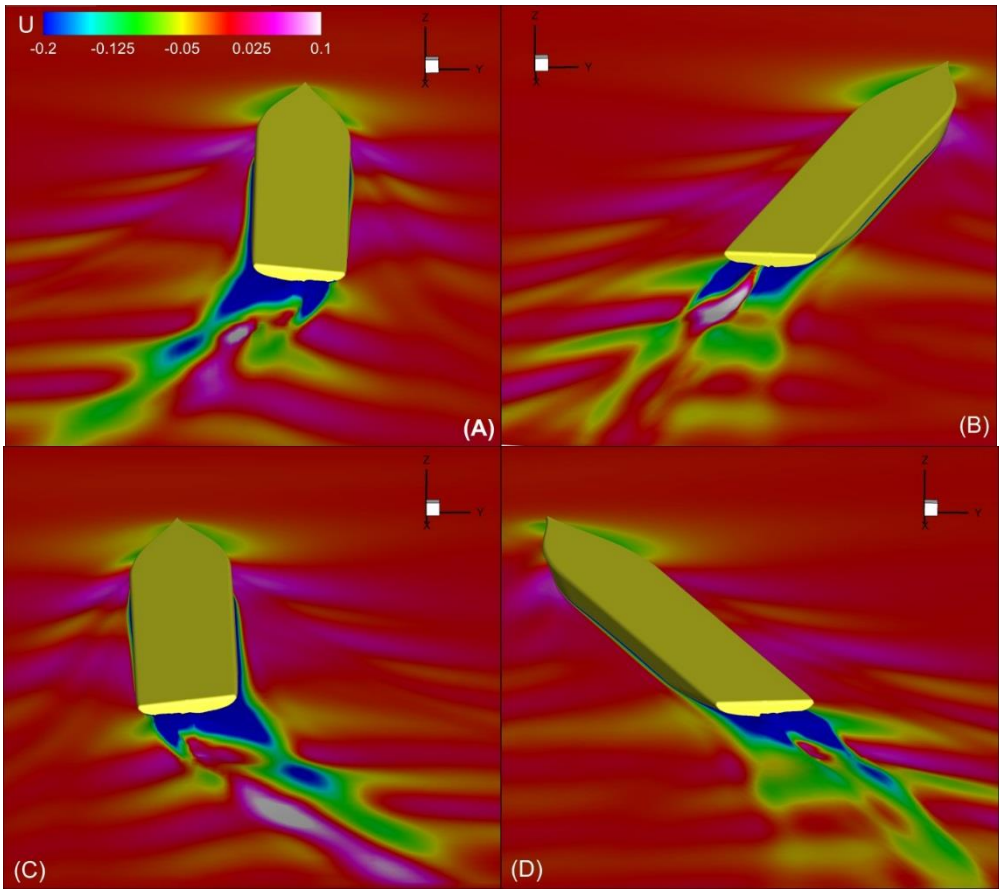

Figure 3.13 Free surface colored with U-velocity for different stages of the 15/1 maneuver. (A) and (C) show zero yaw, (B) and (D) are maximum and minimum yaw, respectively, as shown in Fig. 3.6.

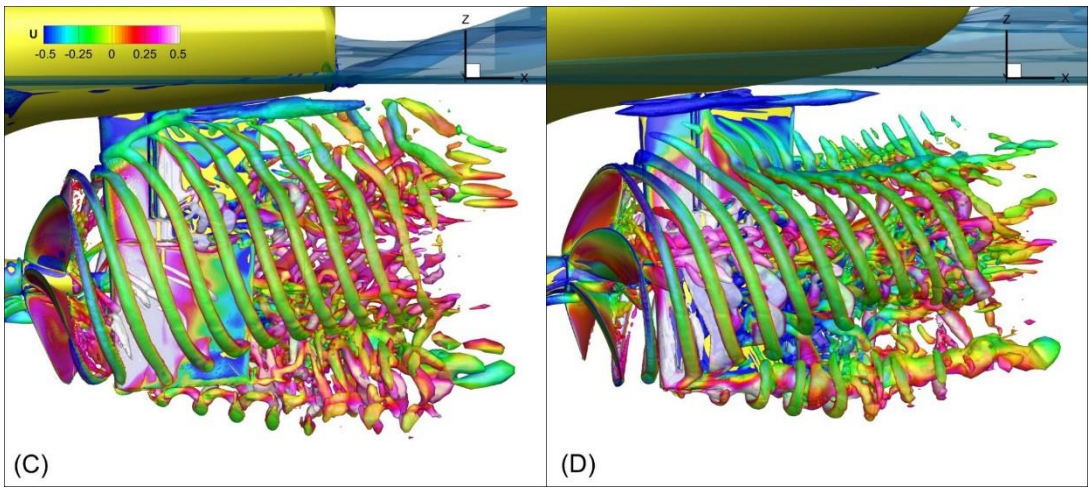

Figure 3.14 Close-up view of the propeller and rudder with isosurfaces of Q=20000 colored with axial velocity for zero yaw (C) and minimum yaw (D), with points (C) and (D) shown in Fig. 3.6.

The main vortical structures observed in the flow in the propeller/rudder region are shown in Fig. 3.15, again for the 15/1 maneuver. Vortices are represented as isosurfaces of $Q = 5000$. The propeller produces strong tip and hub vortices, transported downstream as far as the refinement grid designed to resolve their size is active. At high lift (Figs. 3.15B and 15D where the yaw is maximum and minimum, respectively) the tip of the rudder creates an energetic vortex that pushes the propeller tip vortices to roll around it. At lower ruder loads (Figs. 3.15A and 15C) the interaction between the propeller and rudder tip vortices is weaker, though still noticeable. A necklace vortex can be observed where the root of the rudder meets the hull, stronger when the rudder is under heavier load.

The interaction of the propeller tip vortices, clear in Fig. 3.14, is also evident in the views shown in Fig. 3.15. An additional deformation of the propeller tip vortices is produced by interaction with the keel vortex, as shown in Figs. 3.15A and 15C where the

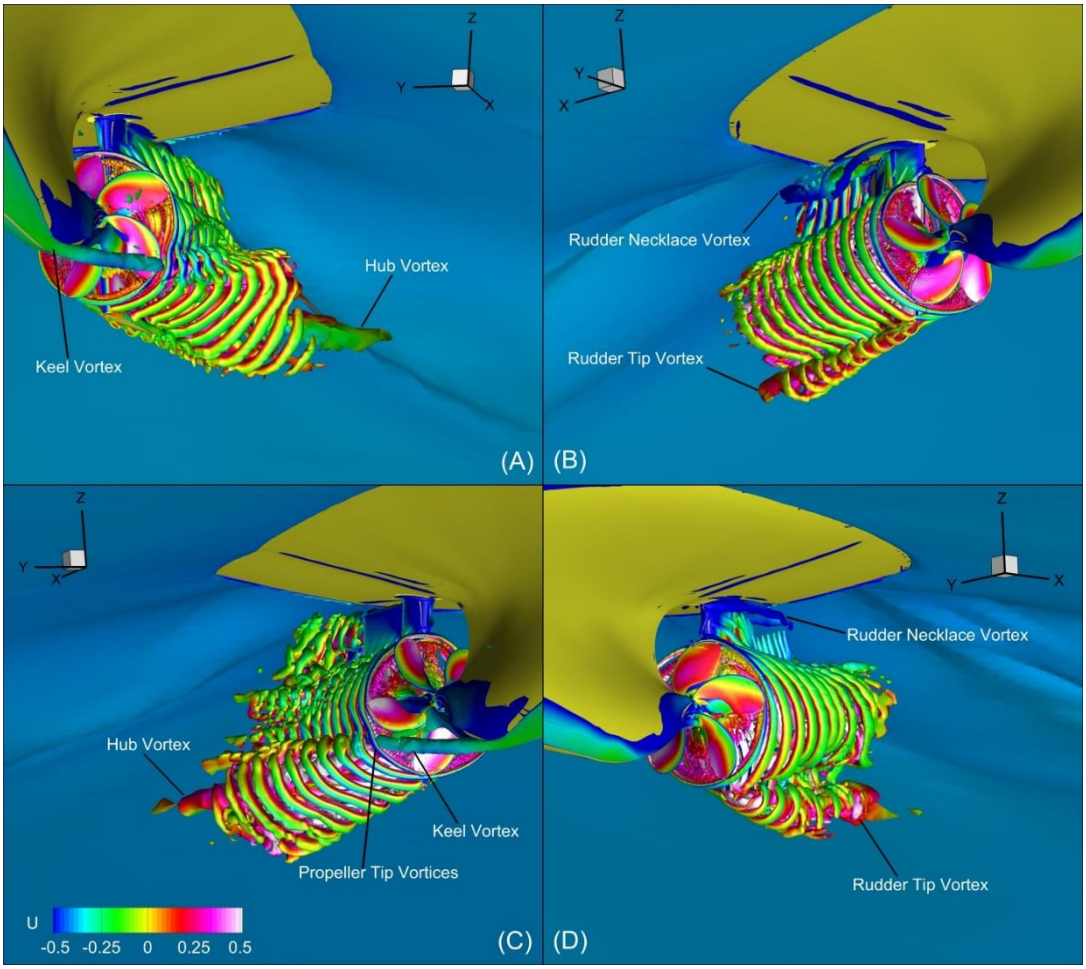

Figure 3.15 Isosurfaces of Q=5000 colored with dimensionless U-velocity for the 15/1 maneuver. (A) and (C) show zero yaw, (B) and (D) are maximum and minimum yaw, respectively, with points (A), (B), (C) and (D) shown in Fig. 3.6.

yaw rate peaks. In Fig. 3.15A the keel vortex has negative axial vorticity and low axial velocity, and as is transported through the propeller and into the wake it swirls the propeller tip vortices creating a bulge in the propeller wake and pushing it down.

The dimensionless vorticity magnitude and the free surface colored by elevation are shown in Fig. 3.16 for the 15/1 maneuver. At point (A) in Fig. 3.6 (Fig. 3.16A) the ship is experiencing zero yaw and the yaw rate peaked after a period of having the rudder 15

degrees to port. The ship and propeller wakes are aligned following essentially the trajectory of the ship. In Fig. 3.16D the yaw is minimum, occurring about 30 s after the rudder was deflected to starboard (see Fig. 3.6). At this time ship's wake near the free surface is redirected by the rudder to starboard while the propeller wake still follows the ship trajectory, effectively splitting the wake in two directions. This behavior is hinted in Fig. 3.13 that shows the velocity at the free surface.

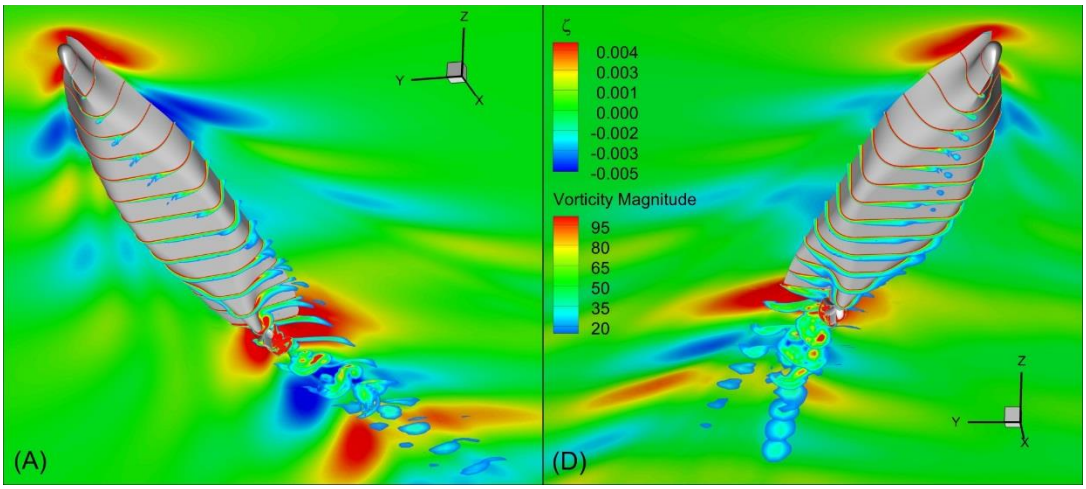

Figure 3.16 Vorticity Magnitude showing the boundary layer during the 15/1 maneuver. (A) Zero yaw and (D) minimum yaw, with points (A) and (D) as shown in Fig. 3.6. Free surface colored with elevation.

3.5 Summary

Simulation of the KCS 15/1 modified zigzag maneuver and 10/10 standard zigzag maneuver with semi-balanced horn rudder and propeller are presented. The results show good agreement between CFD and experimental data for motions, motion rates, propeller forces and moments. Direct CFD simulations provided significant insight of the hydrodynamics occurring during the maneuver that could be very difficult to measure in experiment, such as velocity, pressure fields, and three dimensional vortical structures. The

main differences between CFD and experiments was observed in the prediction of the absolute speed, where experiments show a significant speed decrease when the rudder is operated to port. These speed decreases are significantly weaker in CFD, indicating that modeling of the rudder flow needs improvement. The flow around the rudder is extremely complex, as the rudder is located downstream of the propeller and its inflow contains a variety of vortical scales that makes turbulence modeling specially challenging.

CHAPTER 4

DIRECT SIMULATIONS AND UNCERTAINTY ANALYSIS of KCS ZIGZAG MANEUVER in SHALLOW WATER

4.1 Overview

The ship is designed for operating in deep water but it has to operate also in shallow water when it approaches to harbor. When ship encounters shallow water the flow around the ship hull will change. The velocity of flow beneath the ship bottom increase in shallow water compared with deep water condition. Flow velocity increase because there is a narrow passage for flow between ship bottom and sea bed. As flow velocity increases there is a reduction in bottom pressure which is the source of upward buoyancy force. Due to unfavorable pressure reduction along the ship length, increase in sinkage and trim of the ship may arise. Ship resistance increases, so there is an uncontrolled reduction in the speed. Accordingly, the behavior of ship maneuvering becomes more important in shallow water region where the available water depth is limited and the ship feels forces due to the interaction with the environment (other ships, banks, etc.). Larger ship size such as container ship or tanker leads to more restricted maneuvering space as the harbors and access channels cannot follow the pace of increasing ship size.

In this chapter the behavior of the Korean container ship (KCS) on a zigzag maneuver in shallow water is studied numerically and results are compared with experimental towing tank data. The condition under investigation involves the ship advancing at $Fr = 0.095$ with a depth to draft ratio $H/T = 1.2$. Experiments were

performed at Flanders Hydraulics Research in the shallow water towing tank. The shallow water benchmark data produced by FHR and Ghent University as a resource to validate experiments and CFD computations can be found in the report of the 27th ITTC Maneuvering Committee (2014). The

Direct CFD simulations were initially performed blind at the nominal rudder rate of 16.8 deg/s using direct discretization of moving rudder and propeller, including the tank bottom no-slip condition but neglecting the tank walls. A grid study was conducted for the self-propulsion condition for the propeller RPM, thrust, torque and lateral force, and for the roll and pitch motions, using grids of 8.7 (coarse), 24.6 (medium) and 71.3 (fine) million points. For the first time a grid study was also performed for the zigzag maneuver at the nominal rudder rate evaluating the maximum and minimum values of propeller thrust, torque and lateral force roll, pitch, yaw, roll rate, yaw rate and drift throughout the maneuver. A simulation was then executed on the medium grid at the actual rudder rate achieved in the experiments, and comparisons and analysis of the results were performed. The grid study suggests that forces, moments and motions can be fairly well predicted with the coarser grid, and that the medium grid results are very close to those for the fine grid, but flow details do not seem to converge for the levels of refinement used. The standard verification procedures result in large grid uncertainties, even though plots of time evolution of different variables show good grid convergence performance. The study shows that CFD predictions match satisfactorily the experimental results for most variables, but under-predict yaw and yaw rate.

4.2 KCS Conditions in Shallow Water

The main particulars of the KCS are summarized in Table 4.1. At the nominal self-propulsion approach speed of 0.62 m/s in model scale the Reynolds number is $Re = \frac{U_0 L_{pp}}{v} = 2.74 \times 10^6$, corresponding to $Fr = \frac{U_0}{\sqrt{g L_{pp}}} = 0.095$, where U_0 is the ship service speed and L_{pp} is the length between perpendiculars. ρ is the water density, v is the kinematic viscosity of water and g is the acceleration of gravity. The reference coordinate system attached to the ship follows the standard in the REX, with x the longitudinal axis pointing to stern, y pointing to starboard and z pointing upwards with $z = 0$ at calm water line. All units are in model scale in this chapter unless otherwise stated.

The metacentric height is $11.39\,mm$, corresponding to a vertical location of the center of gravity of $63.5\,mm$ above the waterline in model scale. The 5 blade SVA propeller with variable pitch and a diameter of $0.15\,m$ is used for ship's propulsion system. The propeller's principal particulars are given in Table 4.2. The rudder is a semi-balanced horn design with details provided also in Table 4.2.

Experiments and simulations are performed for shallow water condition with depth to draft ratio $h/T = 1.2$ where h is the distance between ship's water line and sea bed and T is the ships' draft. The modified 20/5 zigzag is performed at constant propeller rotational speed, obtained from self-propulsion at the approach speed, and executing the rudder initially to starboard at the nominal rudder rate of $16.8\,deg/s$. These were the conditions for the blind simulations requested in SIMMAN 2014, but experiments were finally performed with a rudder rate of $8.35\,deg/s$ and slightly different moments of inertia, see Table 4.1.

Table 4.1 Main particulars of the KCS model.

Main Particulars		Model Scale (CFD/EFD)	Full Scale
Length of waterline	$L_{wl}(m)$	4.414	232.5
Length between perpendiculars	$L_{pp}(m)$	4.367	230
Maximum beam of waterline	$B_{wl}(m)$	0.611	32.2
Draft	$T\ (m)$	0.205	10.8
Depth	$D\ (m)$	0.246	19
Displacement*	$\Delta\ (m^3)$	0.3562	52022
Block coefficient (CB)	$\Delta/(L_{pp}B_{wl}T)$	0.651	0.651
Wetted area w/o rudder	$S_w(m^2)$	3.4357	54.5
Midship section coefficient (CM)		0.984	0.985
Longitudinal center of Buoyancy	$LCB\ (\%\ of\ L_{pp})$, Fwd+	-1.48/-1.49	-1.48
Metacentric height	$GM\ (m)$	0.011	0.6
Moment of inertia	K_{xx}/B	0.40 / 0.45	0.4
Moment of inertia	K_{zz}/L_{pp}	0.25 / 0.24	0.25
Service speed	U (m/s)	0.62	4.5
Froude number	Fr	0.095	0.095

Table 4.2 Details of propeller and horn rudder.

Model	SVA
Scale	52.667
Propeller	
Type	CP
No. of Blades	5
D (m)	0.150
P/D (0.7R)	0.700
Rotation	Right Hand
Hub Ratio	0.227
A_e/A_0	0.700
Rudder	
S rudder (m^2)	0.0415
Lat. Area (m^2)	0.0196
Nominal turning rate (deg/s)	16.8

4.3 FHR Free-Running Test

The experimental tests results are provided by Flanders Hydraulics Research (FHR) towing tank. The towing tank for maneuvers in shallow water has a usable length of 68 m, a width of 7 m and a water depth that can be varied to a maximum of 0.5 m. The carriage of the towing tank can be operated both in captive mode (the motions of the ship are forced in the three horizontal degrees of freedom), or in free running mode. In the free-running test, the towing carriage is used to accelerate the ship model and to track its position once released. After test completion, the ship model is caught again and decelerated. Figure 4.1 shows the KCS model in free-running test. In between tests, the ship model is always moved to the next position in a captive way, after which a waiting period of 2000 s is needed for the water in the tank to settle. The limited available width restricts the possible maneuvers that can be performed in the tank (Carrica et al. 2016)

KCS model was used for running tests in both captive and free running conditions, but simulation results are only compared with free running tests. All the free running tests were executed with depth to draft ratio $\frac{h}{T} = 1.2$. Table 4.3 summarizes the KCS free running test results at FHR.

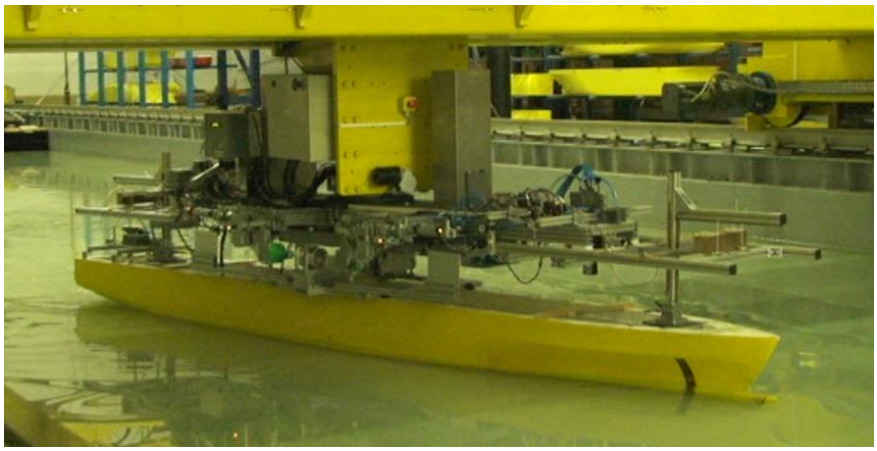

Figure 4.1 Ship model tested in free-running mode.

Table 4.3 KCS free running tests performed at FHR.

Test	Nominal approach speed (m/s)	Nominal propeller rate (rpm)	Repetitions	Sampling frequency (Hz)
Start of 35 degree turn to port	0.62	331.5	7	40
Start of 35 degree turn to starboard	0.62	331.5	6	40
10/2.5 zigzag test, starting to port	0.62	331.5	11	40
10/2.5 zigzag test, starting to starboard	0.62	331.5	10	40
20/5 zigzag test, starting to port	0.62	331.5	10	40
20/5 zigzag test, starting to starboard	**0.62**	**331.5**	**10**	**40**

Due to geometric limitations, modified zigzag tests were executed to limit the lateral path of the ship model and to limit possible tank wall effects. According to the experiment reports, the tests were conducted in 2010 following the relevant ITTC procedures but the test results were reprocessed in 2014 because the accuracy in output frequency of experimental data was not high enough to make comparisons with the CFD results. The resolution of filtering the rudder angle measurements were too coarse so it was very difficult to determine the rudder executions during the maneuvering experiments.

Also, the nominal rudder rate of 16.8 deg/s was not achievable during the experimental test due to friction issues.

To evaluate uncertainty, ten test repetitions were executed. ITTC recently issued a new guideline (ITTC Quality Systems Manual, 2014) on sensitivity analysis for free running tests. The new guideline discusses propagation of the uncertainty on the initial conditions, which at FHR fluctuate little due to the captive acceleration procedure used in experiment. Even if the initial conditions are not well controlled (within certain limits), the KVLCC2 example presented in the ITTC guideline shows that the number of test repetitions is far more important in determining the uncertainty than possible deviations in initial conditions. It is interesting to note, in addition, that experiments at FHR show much larger standard deviations for KVLCC2 than for KCS experiment, even though the acceleration and release mechanisms used in the experiments is the same for both models. A more detailed discussion on this topic is provided by Eloot et al. (2015).

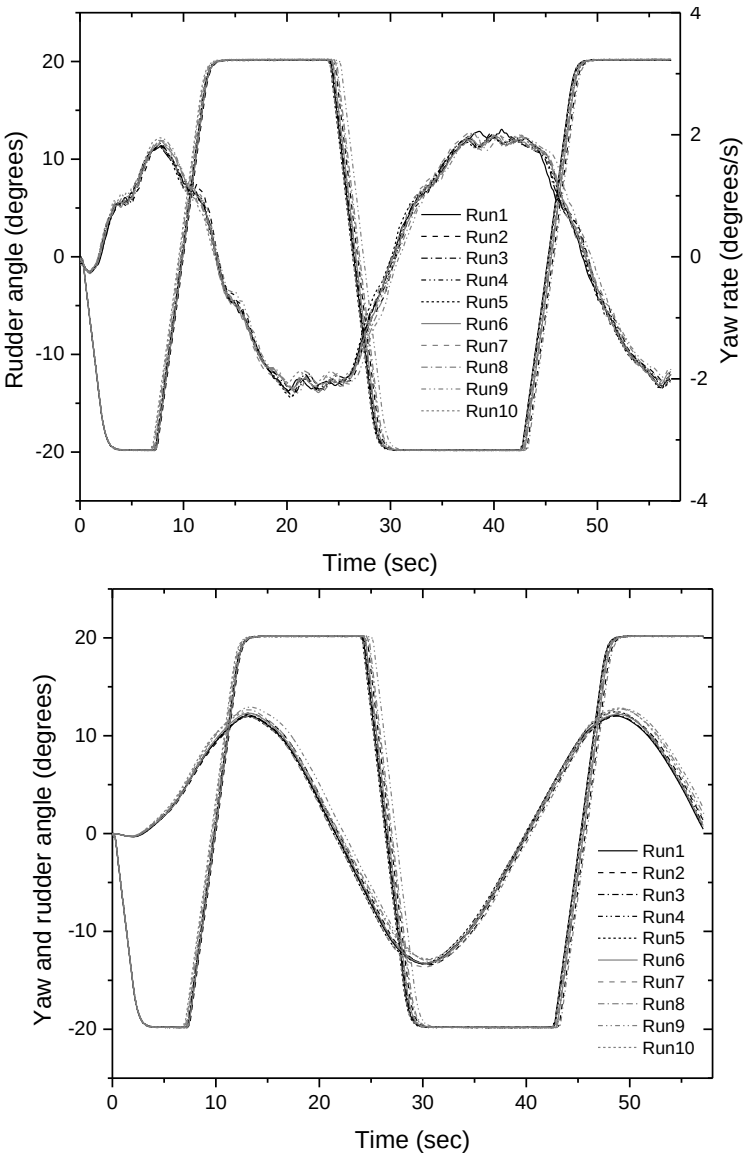

Figure 4.2 20/5 zigzag maneuver with start to starboard: yaw and rudder angles and yaw rate time series measured during ten repeated tests.

Figure 4.2 shows time histories of yaw angle, rudder angle and yawing rate for ten tests of the 20/5 zigzag maneuver. As previously stated, the initial conditions are very well controlled with a very repeatable experimental rudder angle rate, resulting in also highly repeatable experimental results. Once the prescribed yaw angle change of 5 degrees is detected for the first rudder execute, small deviations in rudder angle setting and yaw angle

change can be observed. The time difference in zero crossing between the ten tests is largest at the second rudder angle execute, but remains smaller than 1 second (5% of the maneuver time to the zero crossing). The statistical results of the ten tests are shown in Table 4.4 with relative deviations situated between 0.46% for the period and 2.75% for the first overshoot.

Table 4.4 Averages and standard deviations for ten repeated 20/5 zigzag tests.

Quantity	Unit	Mean	Standard Deviation	Relative	Delta
Period	(s)	40	0.183	0.46%	0.60
Time to 1st heading deviation (HD)	(s)	7	0.125	1.78%	0.40
Travelled distance to 1st HD	(m)	4.316	0.090	2.09%	0.29
Time between 1st HD and max heading (MH)	(s)	6.17	0.157	2.54%	0.60
Travelled distance between 1st HD and MH	(m)	3.692	0.082	2.23%	0.31
Time between 2nd HD and max heading (MH)	(s)	6.11	0.110	1.80%	0.30
Travelled distance between 2nd HD and MH	(m)	3.421	0.062	1.80%	0.15
Max. heading 1	(°)	11.990	0.330	2.75%	1.02
Max. heading 2	(°)	-12.739	0.234	1.84%	0.81

4.4 Grid and Simulation Design

The grid overset topology of KCS is shown in Figure 4.3. The grid system is similar to deep water case except modification in background grid in order to satisfy the shallow water depth. The overset grid system consists of 38 grid blocks for medium and fine grids, including grids for hull, propeller, rudder, refinements and background. These 38 blocks are distributed in 168 and 352 processors for medium and fine grids, respectively, as listed in Table 4.5 for the fine grid. The coarse grid consists of 40 grid blocks distributed in 71 processors, needing two more blocks to ensure enough overlap in the area of the hull stern shaft hub and the region above the water in air. The total number of grid points for the coarse, medium and fine grids are 8.7, 24.6 and 71.3 million, respectively. Same refinement

grids as deep water case are considered here at propeller/rudder region to ensure the overlapping is fine enough to obtain donor cells and valid interpolations between grids.

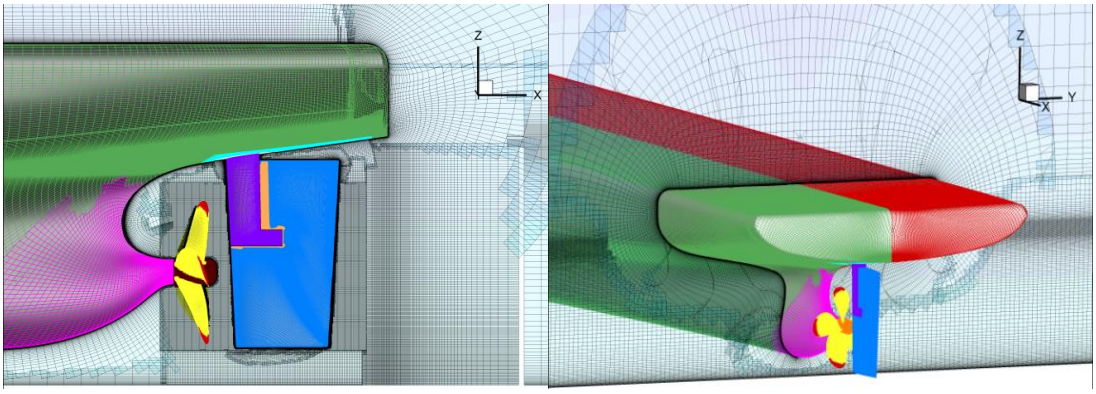

Figure 4.3 Overset grid system topology, medium grid shown.

The code Suggar is used to compute the overset domain connectivity, initially as a preprocessing step to assure proper overlap and grid quality, and then dynamically at run time as the ship, propeller and rudder move. Table 4.5 also shows the hierarchy of bodies used to run the simulation. The ship body is solved as a rigid body in 6DoF, and contains all grids defining the geometry and the refinements that follow the ship in all degrees of freedom. Rudder and propeller grids are children to the ship, and move according to the control laws for these appendages. Three Suggar groups including propeller, rudder, and ship/refinements are used for this simulation. Background and Refinement grids which connecting the ship to the far-field boundary conditions are listed in Table 4.5. These grids are restricted to move only in 3 degrees of freedom and they cannot move with ship in pitch, heave or roll motions during the simulations.

Table 4.5 Details of the fine grid system and decomposition information.

Grid	Size	Grid Points	Belongs to body	Processors
Boundary layer starboard 1	340×77×125	3273 K	Ship	18
Boundary layer starboard 2	340×81×74	2038 K	Ship	10
Stern starboard	85×67×71	404 K	Ship	2
Hub starboard	99×57×71	401 K	Ship	2
Boundary layer port1	340×77×125	3273 K	Ship	18
Boundary layer port2	340×81×74	2038 K	Ship	10
Stern port	85×67×71	404 K	Ship	2
Hub port	99×57×71	401 K	Ship/Propeller	2
Propeller hub	142×44×128	800 K	Ship/Propeller	4
Propeller blades	5×111×71×104	5x820 K	Ship/Propeller	20
Propeller tips	5×71×51×99	5x401 K	Ship	10
Refinement wake	111×191×190	4028 K	Ship	20
Refinement	340×200×142	9656 K	Ship	48
Background	255×198×128	6463 K	Ship	36
Rudder stem refinement	85×63×153	819 K	Ship	4
Rudder stem starboard	85×77×125	818 K	Ship	4
Rudder stem port	85×77×125	818 K	Ship	4
Rudder stem top	77×63×85	412 K	Ship	2
Rudder stem bottom	167×57×85	809 K	Ship	4
Refinement gap top	36×145×77	402 K	Ship	2
Rudder gap	102×49×247	1235 K	Ship/Rudder	7
Rudder top	159×50×51	405 K	Ship/Rudder	2
Rudder starboard	297×66×125	2450 K	Ship/Rudder	14
Rudder port	297×66×125	2450 K	Ship/Rudder	14
Rudder cap top	99×57×71	401 K	Ship/Rudder	2
Refinement propeller/rudder	283×242×213	14587 K	Ship	75
Refinement rudder bottom	170×165×29	813 K	Ship	4
Refinement rudder port	165×29×170	813 K	Ship	4
Refinement rudder starboard	165×29×170	813 K	Ship	4
Refinement rudder top	165×170×29	813 K	Ship	4
Total		**71.3 M**		**352**

Before starting the simulations, a pre-processing hydrostatic computation is conducted to obtain the longitudinal location of the center of gravity, the mass and the static wetted area of the ship in static condition. After the correct values are obtained, the input files for REX and Suggar need to be modified with the new values. Table 4.6 summarizes the nominal and actual CFD and EFD values for the longitudinal location of the center of gravity and the displacement.

Table 4.6 Hydrostatic results for medium grid.

Parameter	CFD	EFD (nominal)	EFD (actual)
Displacement (m^3)	0.3528	0.3562	0.3561
Longitudinal Center of Gravity (m)	0.5098	0.5092	0.5096

The simulation does not include the walls of the towing tank where the experiments were performed, but uses a no-slip boundary condition at the bottom. All simulations are performed in the earth coordinate system, thus the boundary conditions are inlet at the upstream and side boundaries ($U = V = W = 0, \frac{\partial P}{\partial n} = 0$), fixed non-slip at the bottom (in this case same as inlet), moving non-slip at all solid surfaces ($\boldsymbol{U} = \dot{\boldsymbol{x}}, \frac{\partial P}{\partial n} = 0$) and exit at the downstream boundary ($\frac{\partial^2 U}{\partial n^2} = 0, \frac{\partial^2 V}{\partial n^2} = 0, \frac{\partial^2 W}{\partial n^2} = 0, \frac{\partial P}{\partial n} = 0$).

The PI controller on the propeller rotational speed is used for self-propulsion computations to achieve the target velocity $U_0 = 0.62\ m/s$ as described by Eqs. (2.38) and (2.39). The self-propulsion state is obtained when propeller rotational speed and ship speed reach steady state condition. To improve convergence to self-propulsion, the inertia of the ship was decreased by a factor of 10 during the computations, which increases the acceleration of the ship but has no effect on the results once the steady-state is reached. For zigzag simulations the actual inertia of the system is used.

One ship reaches the self-propulsion condition the zigzag maneuvers are started from this point. During the zigzag maneuvers the propeller rotational speed is maintained constant at the self-propulsion value. The zigzag maneuver controller is activated to execute the rudder according to the specified values of rudder rate and rudder angle and checking the ship heading in the maneuver. Since this simulation is performed based on

20/5 zigzag maneuver, the rudder first executes to 20 deg. and holds until the ship heading reaches 5 deg. and then rudder turns to the other side. As mentioned earlier, CFD simulations were initially performed blind at the nominal rudder rate of 16.8 deg/s. A simulation was then executed on the medium grid at the actual rudder rate achieved in the experiments (8.35 deg/s), and comparisons and analysis of the results were performed. A total of 52000 time steps with time step of $\Delta t = 1.56\, ms$ were used to get approximately one period for the 20/5 modified zigzag maneuver for coarse and medium grids and a total of 53000 time steps with $\Delta t = 1.3\, ms$ were used for fine grid.

4.5 Grid Studies for Self-propulsion and Zigzag Maneuver

4.5.1 Self-Propulsion and Maneuvering Verification

A grid study was performed to estimate the grid numerical uncertainties of the solutions for self-propulsion and for the 20/5 zigzag maneuver at the nominal rudder rate according to the procedure presented in Stern et al. (2001) and Wilson et al. (2004). This simulation was performed in a blind fashion, and then compared with experimental data at SIMMAN 2014. Due to experimental limitations already described, the rudder rate in the experiments was lower than the nominal rate. The simulations were repeated at the experimental rudder rate using the medium grid, but the grid study was not repeated due to cost and the considerable similarity for both conditions. Both CFD and EFD results for the experimental rudder rate are presented in the next section.

The first step for estimation of the grid uncertainty (U_G) is the convergence study. Solutions on three systematically refined grids with refinement ration R_G are required:

$$r_G = \frac{\Delta x_2}{\Delta x_1} = \frac{\Delta x_3}{\Delta x_2} \tag{4.1}$$

where the subscripts 1, 2 and 3 represent the fine, medium and coarse grids and Δx is the grid spacing. Three convergence conditions are possible, defined as:

$$R_G = \frac{\varepsilon_{12}}{\varepsilon_{23}} = \frac{S_2 - S_1}{S_3 - S_2}$$
$$= \begin{cases} 0 < R_G < 1 & : Monotonic\ convergence \\ -1 < R_G < 0 & : Oscillatory\ convergence \\ R_G > 1, R_G < -1 : & Divergence \end{cases} \tag{(4.2}$$

In grid divergence condition no uncertainty can be estimated. In oscillatory grid convergence the uncertainty is estimated by

$$U_G = |1/2(S_U - S_L)| \tag{4.3}$$

where S_U and S_L are the maximum and oscillation minimum of the solutions from the coarse, medium, and fine grids. In monotonic convergence the generalized Richardson extrapolation is used to estimate the grid error $\delta^*_{RE_G}$ and the order of accuracyP_G,

$$\delta^*_{RE_G} = \frac{\varepsilon_{G_{21}}}{r_G^{P_G} - 1} \tag{4.4}$$

$$P_G = \frac{\ln\left(\varepsilon_{G_{32}}/\varepsilon_{G_{21}}\right)}{\ln(r_G)} \tag{4.5}$$

When $\delta^*_{RE_G}$ and P_G are known the grid uncertainty is estimated. There are two procedures to estimate the grid uncertainty based on the range of the correction factor,C_G, which is given as:

$$C_G = \frac{r_G^{P_G} - 1}{r_G^{P_{Gest}} - 1} \tag{4.6}$$

where P_{Gest} is the limiting or theoretical accuracy of the applied numerical method. If $C_G \approx 1$ the solutions are close to the asymptotic range. In this case the sign of the error is known, and the numerical error δ_{SN}^*, benchmark S_C and uncertainty U_{GC} can be calculated as:

$$\delta_{SN}^* = C_G \delta_{RE_G}^* \tag{4.7}$$

$$S_C = S - \delta_{SN}^* \tag{4.8}$$

$$U_{GC} = \begin{cases} \{(2.4(1 - C_G)^2 + 0.1)\left|\delta_{RE_G}^*\right|, & |1 - C_G| < 0.125 \\ |1 - C_G|\left|\delta_{RE_G}^*\right| & , |1 - C_G| \geq 0.125 \end{cases} \tag{4.9}$$

If $C_G >> 1$ only the numerical uncertainty is calculated as

$$U_G = \begin{cases} (9.6(1 - G_C)^2 + 1.1\left|\delta_{RE_G}^*\right|, |1 - G_C| < 0.125 \\ (2|1 - G_C| + 1)\left|\delta_{RE_G}^*\right| & , |1 - G_C| \geq 0.125 \end{cases} \tag{4.10}$$

Table 4.7 summarizes the three grids and the design y^+ of the first boundary layer grid point. An appropriate refinement ratio of $r_G = \sqrt{2}$ is used here.

Grid studies were performed on propeller forces and moments and motion parameters. It should be noted that the solutions on all three grids are run only to the point where the zigzag maneuver covers the first two overshoots.

Table 4.7 Grid dimensions and y^+ values for refinement study.

Grid	Grid Points	y^+
1- Coarse	8.7 M	1.4
2- Medium	24.6 M	1
3- Fine	71.3 M	0.7

Figure 4.4 shows the time history of the propeller rotational speed and the ship velocity as self-propulsion is obtained for all three grids. Self-propulsion at the target speed of 0.62 m/s is achieved at 338.7 RPM, which compares to the experimental value of 331.5 RPM. Figure 4.5 depicts evolution of forces and torque on the propeller during the self-propulsion. All three grids show similar results with slightly higher thrust and torque for coarse grid. For propeller y-force high frequency fluctuations are captured in all three grids. Table 4.8 shows verification results in propeller RPM, forces, torque and pitch and roll angles at self-propulsion.

Table 4.8 Grid convergence for forces, moment and motions at self-propulsion. δ_G^*, $U_{GC}$and U_G are $\%S_2$.

Variable	Coarse Grid	Medium Grid	Fine Grid	R_G	P_G	C_G	δ_G^*	U_{GC}	S_C	U_G	Convergence Type
RPM	338.87	338.76	338.7	0.33	3.2	2.03	0.01	0.005	338.7	0.02	Monotonic
Q_P	132.1	126.8	125.4	0.26	3.8	2.8	1.1	0.71	125.4	1.15	Monotonic
F_{P_y}	0.0726	0.088	0.0925	0.29	3.5	2.4	-5.1	2.99	0.0925	8.67	Monotonic
θ	-0.011	-0.0133	-0.014	0.54	1.75	0.83	-9.02	-1.80	-0.014	-10.8	Monotonic
T_P	5.48	5.4	5.352	0.68	1.1	0.47	1.01	1.15	5.344	1.04	Monotonic
$\emptyset$	0.135	0.108	0.121	-0.23						12.5	Oscillatory

The grid study shown in Table 4.8 shows monotonic convergence for RPM with $R_G = 0.33$, propeller torque and side force with R_G of 0.15 and 0.4 respectively. The pitch angle also converged monotonically with R_G of 0.54.

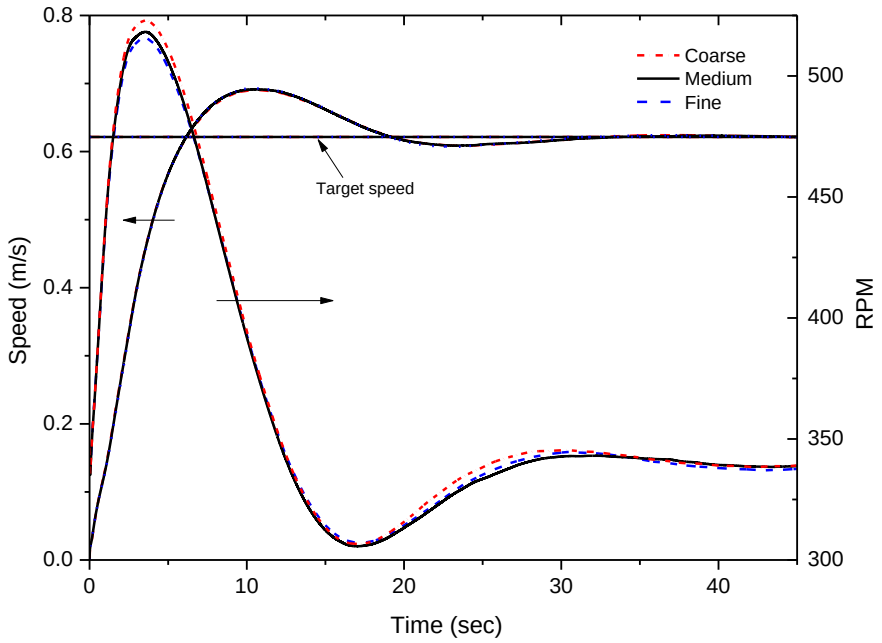

Figure 4.4 Time history of ship speed and propeller rotational speed for the self-propulsion computation for Coarse, Medium and Fine grids.

The roll angle and propeller thrust show oscillatory convergence with $R_G = -0.23$ and -0.48, respectively. The U_G is around $1\%S_2$ for all variables, except for roll and pitch angles and the propeller side force, which are one order of magnitude larger closer to $10\%S_2$, though these variables are very small in self-propulsion and thus subject to large relative errors. The average of the grid uncertainty for the most relevant self-propulsion variables (RPM, propeller thrust and torque) is about $U_G = 0.75\%$, suggesting that the effects of the grid changes are small on the results for the present range of grid sizes.

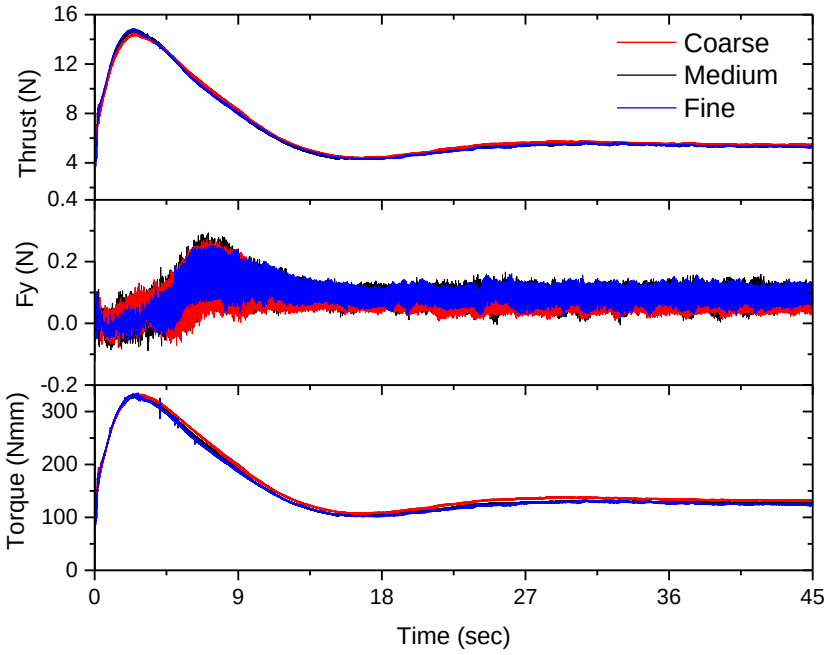

Figure 4.5 Time history of propeller thrust, side force and torque for the self-propulsion computation for Coarse, Medium and Fine grids.

Table 4.9 summarizes the results of the grid study for the 20/5 zigzag maneuver at the nominal rudder rate. The verification study is performed for the first time on naturally transient flow problem such as maneuvering. Special care must be taken to select proper variables to perform grid study. For motions, forces and moments results, the verification parameters are maximums and minimums of roll, pitch, yaw, drift angles, roll rate, yaw rate, and propeller thrust, torque and side force at minimum and maximum yaw rate . The grid study shows monotonic convergence for maximum roll angle, maximum and minimum pitch angles, minimum yaw angle and propeller side force with R_G of 0.013, 0.42, 0.13, 0.35 and 0.074, respectively. The minimum roll angle, minimum and maximum roll rate show oscillatory convergence with $R_G = -0.38$, $R_G = -0.014$ and $R_G = -0.054$, respectively. Maximum yaw angle and maximum and minimum yaw rate also

display oscillatory convergence with $R_G = -0.43$, $R_G = -0.3$ and $R_G = -0.69$, respectively. Maximum and minimum drift angle variables also show oscillatory convergence with $R_G = -0.44$ and $R_G = -1.74$. The propeller thrust at maximum and minimum yaw rate converged oscillatorily with $R_G = -5.6$ and $R_G = -0.33$. Propeller torque at minimum yaw rate also shows oscillatory convergence with $R_G = -0.018$.

In contrast to self-propulsion grid study, several propeller forces and torque parameters show monotonic divergence for the zigzag maneuver. In addition the minimum drift angle exhibits oscillatory divergence. The nature of the time evolution dependence of the flow, and thus forces and integrated motion quantities, complicates the grid study, highlighting the difficulties of using the classic grid convergence procedures designed for steady-state problems when analyzing transient flows like a zigzag maneuver. Inspection of Figs. 4.6-4.10 show good grid convergence, with significant similarity between medium and fine grids, but with the coarse grid deviating more, most notably for the roll angle shown in Fig. 4.8. This may indicate that the coarse grid is too coarse for asymptotic behavior, and that an even finer grid is needed for the study, which with the refinement ratio $r_G = \sqrt{2}$ would result in approximately 200 M grid points, prohibitive for the computational resources available for this research.

Table 4.9 Grid convergence for forces, moment and motions variables for the zigzag maneuver at nominal rudder rateδ_G^*, U_{GC} and $U_G$are $\%S_2$.

Variable	Coarse Grid	Medium Grid	Fine Grid	R_G	P_G	C_G	δ_G^*	U_{GC}	S_C	U_G	Convergence Type
$\emptyset_{max}$	2.074	1.73	1.725	0.013	12.57	77.08	0.25	0.25	1.72	0.51	Monotonic
$\emptyset_{min}$	-1.78	-1.87	-1.84	-0.38						-2.5	Oscillatory
θ_{max}	-0.002	-0.00295	-0.00335	0.42	2.5	1.375	-13.56	-3.7	-0.0034	-17.26	Monotonic
θ_{min}	-0.02174	-0.02026	-0.02006	0.13	5.77	6.4	-0.002	0.001	8.44	0.003	Monotonic
ψ_{max}	8.29	8.44	8.38	-0.43						-0.9	Oscillatory
ψ_{min}	-8.23	-8.51	-8.60	0.35	3.03	1.86	-0.004	0.002	1.67	0.02	Monotonic
$\dot{\phi}_{max}$	1.36	1.53	1.52	-0.054						5.53	Oscillatory
$\dot{\phi}_{min}$	-1.43	-1.492	-1.490	-0.0135						0.66	Oscillatory
$\dot{\psi}_{max}$	1.38	1.47	1.46	-0.106						-14.15	Oscillatory
$\dot{\psi}_{min}$	-1.52	-1.60	-1.58	-0.277						-8.26	Oscillatory
β_{max}	1.579	1.673	1.632	-0.44						2.8	Oscillatory
β_{min}	-1.79	-1.82	-1.77	-1.74						-1.17	Oscillatory Divergence
$T_{P_{X,\dot{\psi}_{max}}}$	5.31	5.21	5.08	1.411	-0.99	-0.29	2.58	11.42	5.08	14	Monotonic Divergence
$T_{P_{X,\dot{\psi}_{min}}}$	4.92	4.91	4.81	15.356	-7.88	-0.93	2.09	4.33	4.81	6.42	Monotonic Divergence
$F_{P_{y,\dot{\psi}_{max}}}$	0352	0.352	0.316	170.33	-14.82	-0.99	10.16	20.4	0.32	30.54	Monotonic Divergence
$F_{P_{y,\dot{\psi}_{min}}}$	-0.486	-0.459	-0.438	0.77	0.75	0.298	4.55	-10.73	-0.44	-15.29	Monotonic
$Q_{P,\dot{\psi}_{max}}$	131.45	125.39	122.3	0.518	1.90	0.93	2.5	0.19	122.25	2.69	Monotonic
$Q_{P,\dot{\psi}_{min}}$	120.88	119.75	116.52	2.84	-3.01	-0.65	2.69	6.85	116.52	9.54	Monotonic Divergence

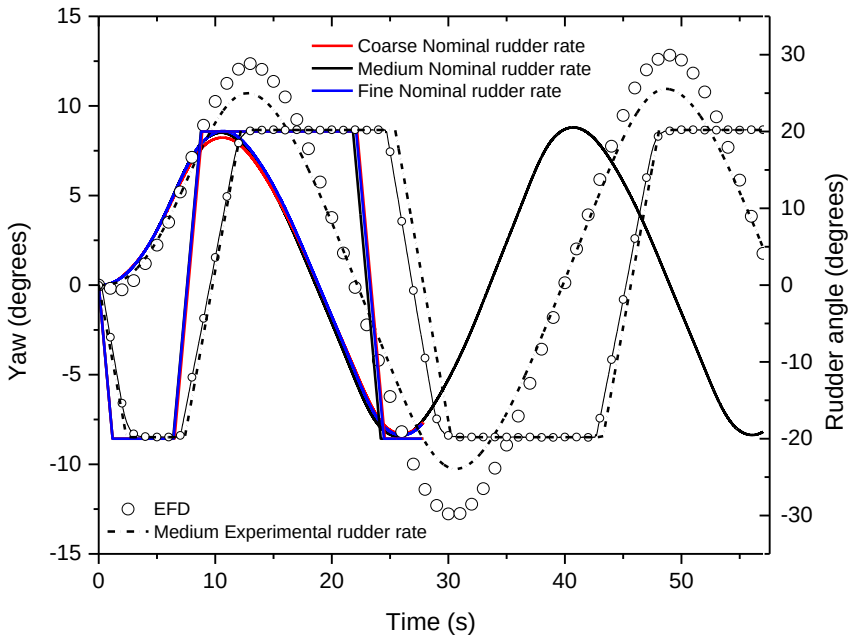

Figure 4.6 Yaw and rudder angles for the 20/5 zigzag maneuver at nominal rudder rate for Coarse, Medium and Fine grids, and at the experimental rate for the medium grid and EFD. The experimental rudder rate is shown in lines with small white circle.

The grid uncertainties are higher than for the self-propulsion analysis, with U_G for the parameters that exhibit monotonic convergence ranging from $-17.26\%S_2$ to $2.69\%S_2$ in which the minimum is for maximum pitch angle and the maximum is for propeller torque at maximum yaw rate. The average grid uncertainty for monotonic convergence is $U_G = 2.6\%$, slightly higher than the experimental standard deviation. Grid uncertainties are higher for parameters showing oscillatory convergence.

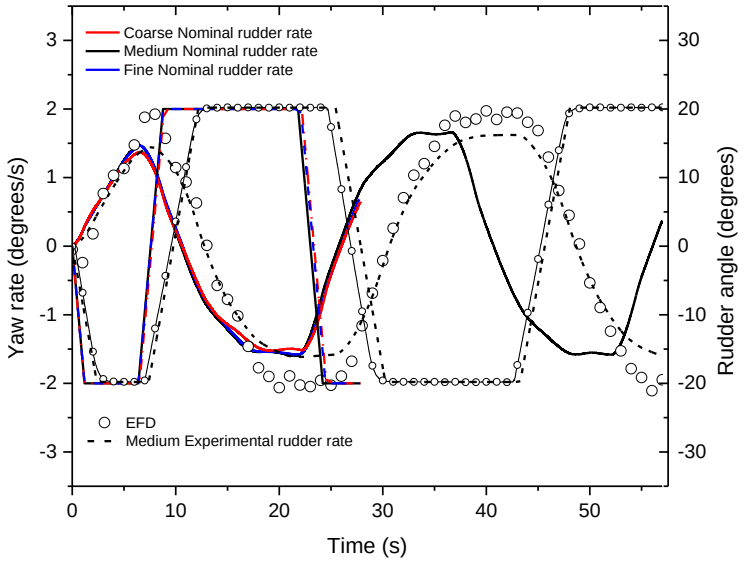

Figure 4.7 Yaw rate and rudder angle for the 20/5 zigzag maneuver at nominal rudder rate for Coarse, Medium and Fine grids, and at the experimental rate for the medium grid and EFD. The experimental rudder rate is shown in lines with small white circle.

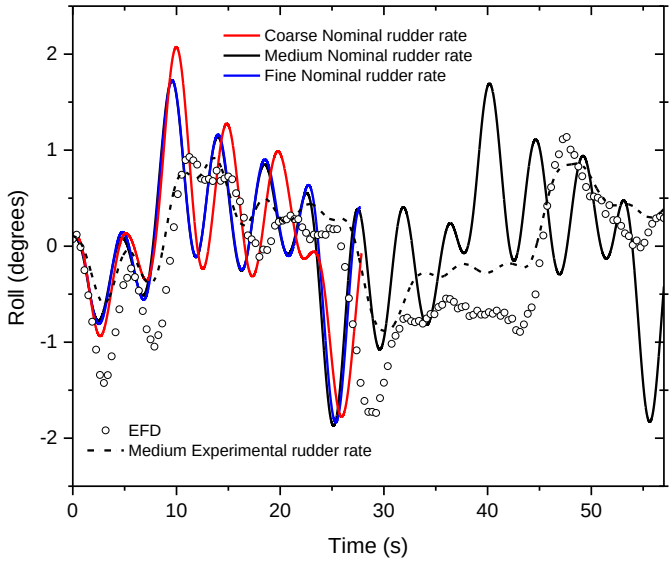

Figure 4.8 Roll angle for the 20/5 zigzag maneuver at nominal rudder rate for Coarse, Medium and Fine grids, and at the experimental rate for the medium grid and EFD.

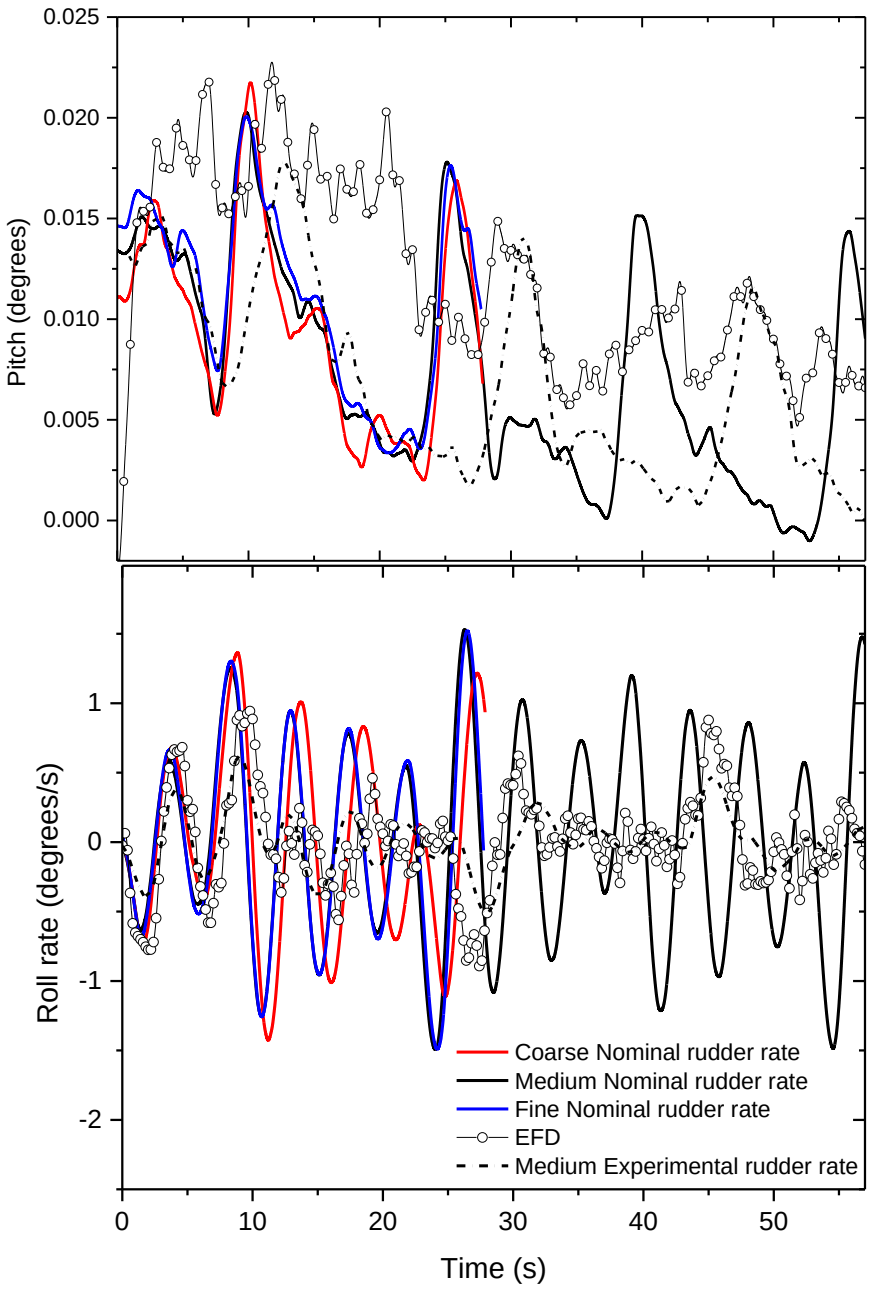

Figure 4.9 Pitch angle and roll rate for the 20/5 zigzag maneuver at nominal rudder rate for Coarse, Medium and Fine grids, and at the experimental rate for the medium grid and EFD.

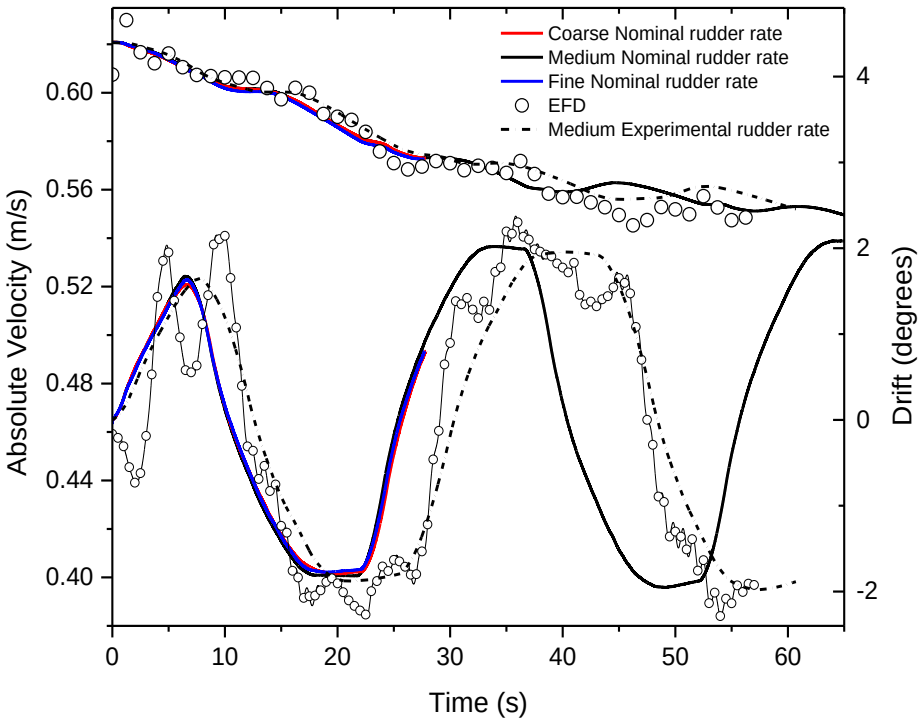

Figure 4.10 Ship absolute velocity and drift angle for the 20/5 zigzag maneuver at nominal rudder rate for Coarse, Medium and Fine grids, and at the experimental rate for the medium grid and EFD.

Time histories of yaw, yaw rate and rudder angle for the 20/5 zigzag maneuver are shown in Figs. 4.6 and 4.7 show. All grids predict very similar values of yaw and yaw rate as the peak values for these variables converged in monotonic or oscillatory form. Figure 4.8 shows the roll angles for all grids. As can be seen, the difference between the peaks in roll angle for coarse and medium grids is about 16.6% and between the coarse and fine grids this value is about 16.8%. It is clear that the medium and fine grids are predicting the roll angles for the duration of the maneuver with less than 0.25% difference. Figure 4.9 shows the evolution of the pitch angle and roll rate during the maneuver. Notice that pitch angles are very small and the differences between grids are most noticeable for this quantity, but the trends are still consistent for coarse, medium and fine grids. The roll rate

shows trends more consistent with the roll angle, where the medium and fine grid results are almost coincident throughout the maneuver, but the coarse grid sees differences with the other two grids that increase in time. The ship absolute velocity and drift angle are shown in Fig. 4.10. After one zigzag period the ship has not yet reached periodic behavior, with the absolute velocity still decreasing and the drift angle increasing. Here the drift angle is very similar between the grids, but the velocity drops faster for the fine grid than for the medium and coarse grids.

Fig. 4.11 depicts the time histories of propeller thrust and torque for the zigzag maneuver for all grids. Coarse grid results shows higher thrust and torque respect to the medium and fine grid, while the propeller lateral forces are fairly similar for all grids. The propeller torque is the quantity that seems most dependent on the grid refinement used. The difference between the propeller torques at maximum yaw rate for coarse and medium grids is about 4.8% and between the coarse and fine grids is about 7.5% which results in monotonic convergence. The propeller torques at minimum yaw rate also show 0.94% difference between the coarse and medium and 3.7% between the coarse and fine grids with monotonic divergence. As can be seen, the convergence of the propeller torque is remarkably affected by time evolution of this parameter in the presence of highly transient flows in maneuver. Fig. 4.12 shows the rudder resistance and yaw moment during the maneuver. All grids predict the minimum resistance, lateral forces on rudder, rudder response to execution time, and rudder yaw moments, consistently.

Figure 4.13 shows velocity and pressure contours at self-propulsion, maximum yaw rate and minimum yaw rate for all grids. These contours are at downstream of the propeller at $x/L = 1.01$. More detailed flow field can be captured by refining the grids from coarse

to fine due to resolving smaller scales but finer grid do not converge in finer features as the grid is resolved. This condition is more obvious in velocity field since it doesn't produce the fast transients that the pressure sees as it adjusts to conserve mass. This result is expected since LES regions will only converge as the grid approaches the dissipation length, and according to the refinement ratio used in this study it requires approximately 200 M grid points for fine grid in order to achieve convergence.

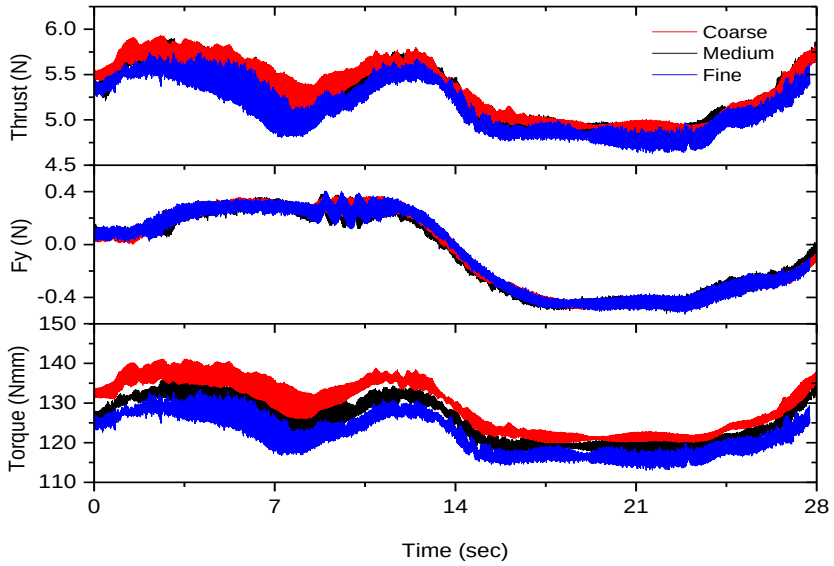

Figure 4.11 Time histories of propeller thrust, side force and torque for the 20/5 zigzag maneuver at nominal rudder rate for Coarse, Medium and Fine grids.

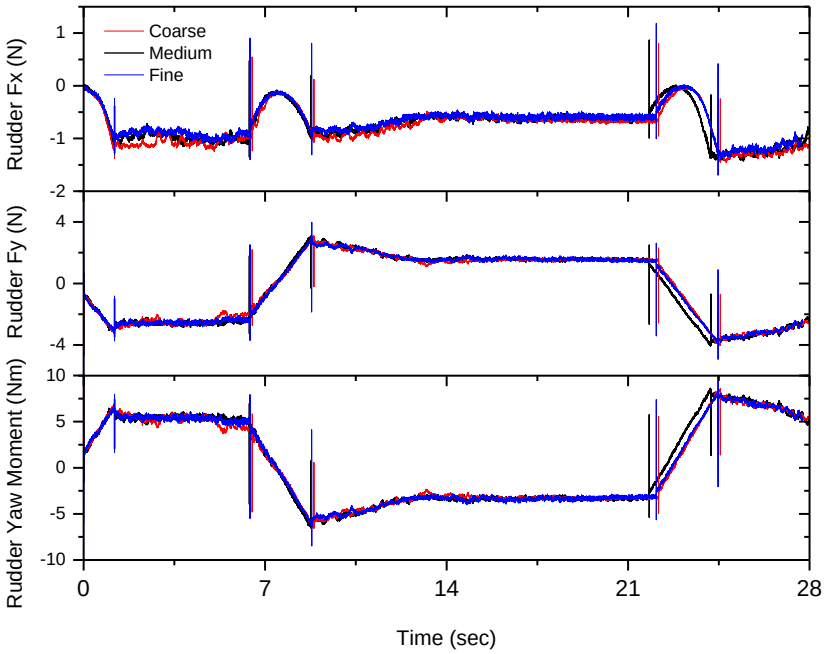

Figure 4.12 Time histories of rudder X-force, Y-force and yaw moment for the 20/5 zigzag maneuver at nominal rudder rate for Coarse, Medium and Fine grids.

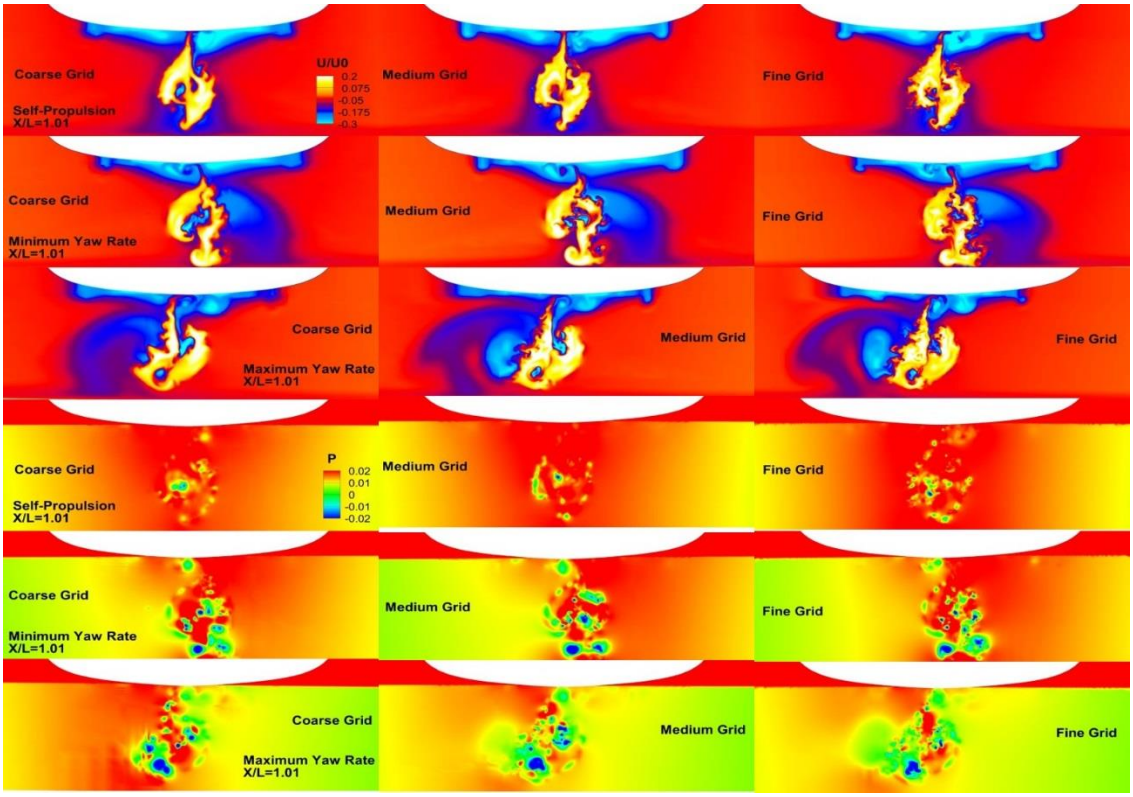

Figure 4.13 Velocity (top figures) and Pressure (bottom figures) contours at X/L=1.01 at self-propulsion (top), minimum yaw rate (center) and maximum yaw rate (bottom) for coarse, medium and fine grids. Vertical axis range: -0.05< Z/L<0.1, horizontal axis range:$-0.09 < Y/L < 0.09$.

4.5.2 Self-Propulsion Validation

Validation is described as a process for estimating simulation modeling uncertainty U_{SM} by using benchmark experimental data and estimating the magnitude and sign of the modelling error δ_{SM}. Therefore, experimental error and uncertainty must be taken into account in addition to the numerical errors and uncertainties in calculation of total validation uncertainty.

Validation was conducted for propeller RPM, thrust and torque, and pitch and roll angles at self-propulsion. Since the available experimental data is for a different rudder

rate, the validation cannot be carried out for the zigzag maneuver. Table 4.10 summarizes the comparison error, validation uncertainty, experimental data uncertainty, and simulation numerical uncertainty for self-propulsion. The comparison error E is defined as the difference between experimental data D and simulation S values

$$E = D - S = \delta_D - (\delta_{SM} + \delta_{SN}) \tag{4.11}$$

where δ_{SM} and δ_{SN} are modelling and numerical errors respectively. To characterize if validation has been achieved, the comparison error E is compared to the validation uncertainty U_V given by:

$$U_V^2 = U_D^2 + U_{SN}^2 \tag{4.12}$$

where U_D is experimental uncertainty and U_{SN} is simulation numerical uncertainty. If $|E| < U_V$, the combination of all the errors in D and S is smaller than U_V and validation is achieved at the U_V level. If $|E| \geq U_V$, modelling improvements are needed (Wilson et al. 2004). Approaches to estimate experimental uncertainties are based on the procedure presented in Coleman and Steele (1999).

As can be seen in Table 4.10, for RPM, $|E| > U_V$ such that it is not validated at $|E| = 2\%D$. For Q_P, T_p, θ and $\emptyset$, $|E| < U_V$ such that these variables are validated at uncertainty validation levels of $U_V = 3.26\%D, 3.01\%D, 935\%D$ and $63.8\%D$, respectively. The pitch angle is validated at a very large relative validation uncertainty level due to the very small absolute value and large $U_{SN} = 61\%D$. The same occurs, but to a lesser extent, with the roll angle.

An experimental uncertainty analysis was conducted for the validation parameters including key elemental errors for propeller RPM, propeller torque and thrust, pitch and roll angles at self-propulsion. Table 4.11 summarizes the experimental errors and total uncertainties of variables listed above. The total uncertainty is computed following the methodology described in ANSI/ASME PTC 19.1 (2005) as:

$$U_{B_{Tot}} = \sqrt{B_L^2 + B_R^2 + B_S^2} \tag{4.13}$$

$$U_{P_{Tot}} = \sqrt{P_{Curve\ fit}^2 + P_{Repeatability}^2} \tag{4.14}$$

$$U_D = t_{\nu,95}\sqrt{U_{B_{Tot}}^2 + U_{P_{Tot}}^2} \tag{4.15}$$

where $U_{B_{Tot}}$ and $U_{P_{Tot}}$ represent total bias or systematic error and total precision or random error, respectively. Calibration errors comporise those elemental errors occurred during the calibration of measuring system, and include the standard or reference value used in calibration (B_S), and the calibration process or curve fit ($P_{Curve\ fit}$). B_L and B_R in equation (4.13) represent linearity and resolution errors, respectively. Repeatability or random error ($P_{Repeatability}$) is calculated based on the ten experiment runs for each variable. Details of experiment uncertainty are presented in Table 4.11. In the experiment the propeller rate was calibrated with a device that measures in steps of 1 RPM. Also, for the self-propulsion test the resulting linearity uncertainty of 2 measured RPM is obtained. Torque and thrust are measured with dynamometer with the linearity within 1% of the load. 1.5% of the measured shaft torque is reported for linear uncertainty. For angle measurements

experiment suggested 0.01 and 0.02 degrees for roll and pitch angles uncertainty, respectively.

Table 4.10 Validation at self-propulsion.

Variable	S	D	E	E%	U_V%	U_D%	U_{SN}%
RPM	338.7	331.5	-7.18	-2.2	0.743	0.742	0.0164
Q_P	125.4	128.9	3.53	2.7	3.26	2.72	1.786
θ	-0.0145	-0.0024	0.012	-514.1	934.9	932.9	60.98
T_P	5.352	5.348	0.004	0.08	3.01	2.06	2.192
$\emptyset$	0.121	0.307	0.186	60.6	63.8	63.6	4.401

Table 4.11 Experimental uncertainties self-propulsion.

Variable	B_L	B_R	B_S	$P_{Curve\ fit}$	$P_{Repeatability}$	U_B	U_P	U_D
RPM	1	0.5	-	-	0.029	1.12	0.029	2.46
Q_P	0.97	0.332	0.3225	0.583	1.026	1.075	1.18	3.51
θ	-	0.01	-	-	0.00043	0.01	0.00043	0.022
T_P	0.025	0.015	-	-	0.0405	0.029	0.0405	0.11
$\emptyset$	-	0.005	-	-	0.0886	0.005	0.0886	0.195

4.6 20/5 Shallow water Zigzag Maneuver Results and Discussion

CFD results for the 20/5 zigzag maneuver at the experimental rudder rate of 8.35 deg/s are used to compare with experimental data. Same Figs. 4.6-4.10 which already discussed in the context of the grid study, are cited here for maneuvering results and discussions.

The time histories of yaw and rudder angles, depicted in Fig. 4.6, show that use of the experimental rudder angle improves dramatically the phase response of the simulation, which matches very well the experiments. Using the actual experimental rudder rate in CFD results in the larger yaw amplitudes respect to the nominal rudder rate, but still are lower than the maximum and minimum values in the experiment. Inspecting Fig. 4.7 depicts that the maximum and minimum yaw rate remains under-predicted by CFD and does not improve when using the slower experimental rudder execution rate respect to the nominal rudder rate. In general, the agreement between CFD predictions and EFD measurements is very good in terms of time to check yaw, period and reach, with some underestimation of the yaw rate and thus the yaw overshoot. Table 4.12 summarizes the main characteristics of the modified zigzag maneuver including the overshoots, period, and yaw rate extremums. The yaw angles are 12.3 and 12.7 degrees for the EFD first and second overshoot, respectively, while CFD results show 10.7 and 10.3 degrees, respectively, indicating an underestimation in the CFD predictions of 13% and 18.9%, respectively. The period of the maneuver is 39.9 s, with CFD predicting a value only 0.2% smaller at 39.8 s. The maximum yaw rate peaks reaches to 1.99 deg/s for EFD and 1.62 deg/s for CFD and the yaw period is about 40 s for both EFD and CFD.

Table 4.12 Parameters for the 20/5 modified zigzag maneuver.

	First Overshoot (degrees)	**Second Overshoot (degrees)**	**Yaw Period (s)**	**First Yaw Rate Peak (degrees/s)**	**Second Yaw Rate Peak (degrees/s)**	**Yaw Rate $(\dot{\psi}_{max} - \dot{\psi}_{min})/2$ (degrees/s)**
EFD	12.3	12.7	39.9	1.95	1.98	1.99
CFD	10.7 (-13%)	10.3 (-18.9%)	39.8 (-0.2%)	1.44 (-26.1%)	1.62 (-18.2%)	1.63 (-18.1%)

It should be noted that, there is a variation in initial conditions of experimental data and maneuvering is started with an initial yaw rate of 0.04 degrees/s, which results in some level of drift of the data towards starboard. In contrast with experiment, the CFD yaw rate is exactly zero at the beginning of the simulation since the self-propulsion computation was restricted from any yaw motion.

There are possible sources of error that can be considered for the discrepancies in prediction of yaw and yaw rates in CFD results, including under-prediction of rudder yaw moment due to separation in CFD and possibly not present in the experiments, over-prediction of the hull yaw moments, effects of neglecting the walls of the tank, etc. The first two sources of errors can be mostly attributed to turbulence modeling. The effects of the walls are purely geometric and can be evaluated through appropriate inclusion of the walls in the simulation, though is not done in the present work.

Figs. 4.8-4.10 depicts the time evolution of Roll motion, Roll rate, pitch, absolute velocity and drift angles and show good agreement between EFD and CFD, though the minimum roll angle is under-predicted. As expected, CFD predictions show remarkable improvement once the experimental rudder is used in computations. Notice that the pitch angles are very small but the CFD trends are still consistent with experiments, which show a bow up tendency every time the rudder is executed. EFD results show 0.005 degrees higher average trim than CFD with smaller amplitude of pitch fluctuations, possibly due to wave reflection on the boundaries. The roll rate, related to the roll damping, is also very consistent with experimental data. Both CFD and EFD results show good agreement of drift angle in terms of amplitude and phase. As expected, the drift angle results have a very similar trend with the yaw rate. Fig. 4.10 also depicts the ship speed during the maneuver

and as the maneuver progresses the velocity of the ship decreases rapidly due to the increase of resistance. Even though there is some uncertainty on how accurately the nominal approach speed has been achieved in EFD, CFD follows the behavior of EFD fairly well.

Time histories of propeller thrust and torque during the zigzag maneuver are shown in Fig. 4.14 and CFD results show excellent agreement with EFD. Similar to simulations in deep water, due to the ship speed loss and reduction in the propeller advance coefficient, the average thrust slowly increases with time. In addition, CFD results depict high frequency oscillations in both thrust and torque that correlate to the blade passage frequency. Since the sampling rate in experiment is not high enough, the EFD cannot resolve these frequencies.

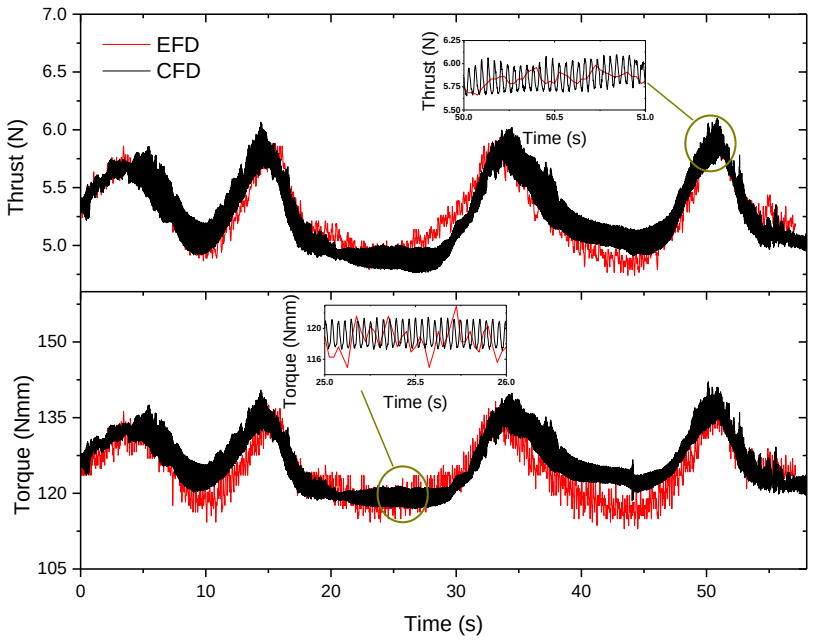

Figure 4.14 Propeller thrust and torque for the 20/5 zigzag maneuvers at the experimental rudder rate for medium grid and EFD.

Figure 4.15 shows vortical structures represented by isosurfaces of Q=5000 in interaction with the moving rudder. This figure was produced with result from the fine grid at the nominal rudder rate, but the fundamental interaction is the same as with the medium grid at the experimental rudder rate. The interaction between propeller and rudder is considerable, especially when the rudder is deflected. As can be seen, the propeller trailing edge, tip and hub vortices transport to the downstream and being stretched by the rudder.

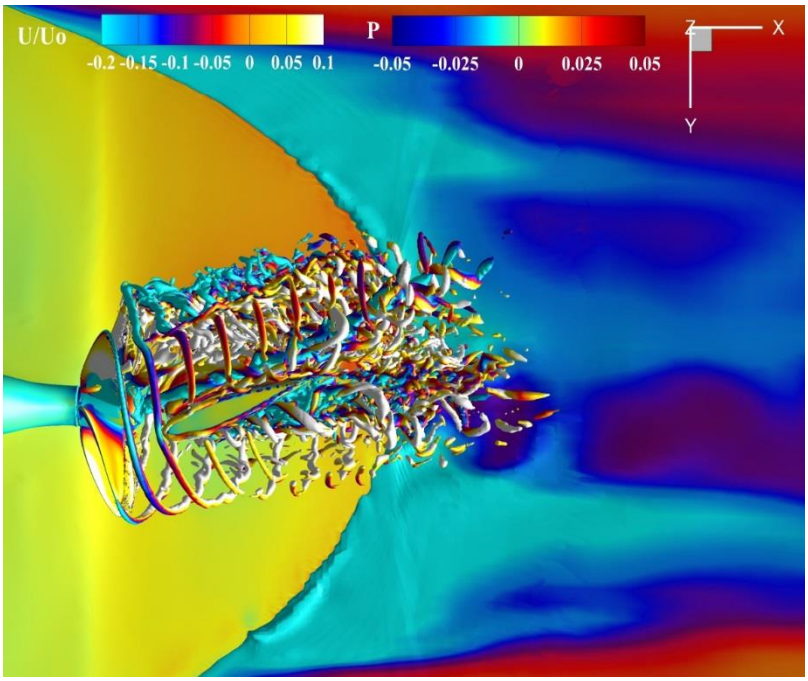

Figure 4.15 Bottom view of the propeller/rudder interaction.

Vorticity magnitude at horizontal sections at the depth of the propeller hub center ($z/R = 0$) and $0.7R$ above and below it, and axial cross sections at the trailing edge of the rudder are shown in Figures 4.16 and 4.17. The solutions are selected at minimum (approximately 31 s in Fig. 4.6) and maximum yaw (49 s through the maneuver), minimum

yaw rate (25 s in Fig. 4.7) and maximum yaw rate (42 s), and zero yaw when ship is turning to port (22 s in Fig. 4.6) and turning to starboard (40 s).

The flow around the rudder and at the bottom portion of it ($z/R = -0.7$) does not show significant separation for most of the above mentioned points, except the massive stall at the minimum yaw rate point. Notice for the maximum yaw rate and the zero yaw turning to starboard points that the interaction between the trailing edge vortices and the rudder causes distinct stretching and strengthening of the vorticity going from leading edge to trailing edge of the rudder. Since the rudder horn is fixed and does not rotate, the top section of the rudder ($z/R = 0.7$) adds additional interactions to the vortical structures coming from propeller. The presence of the rudder horn makes the system to work as a cambered foil with a smaller angle of attack, but still showing signs of separation for the points of maximum yaw, minimum yaw rate and zero yaw to port. The cross section at ($z/R = 0$) shows remarkably stronger vorticity, caused by the presence of the hub vortex. This hub vortex/propeller interaction does not necessarily cause separation, as seems to occur at the points of minimum yaw, minimum yaw rate and zero yaw turning to port. Separation is observed, however, at maximum yaw, while the bottom portion of the rudder separates at minimum yaw. This discrepancy is caused by the swirl introduced by the propeller, which flows starboard to port at the bottom of the propeller and port to starboard at the top, adding to the drift occurring during the maneuver.

Fig. 4.18 shows the boundary layer as cross sections colored with vorticity magnitude at different instants of the maneuver. Since the maneuver is performed in shallow water condition, there is a strong interaction between the bottom, bilge vortex and propeller wakes that introduces instabilities in propeller vortical structures. This condition

is more evident at the minimum and maximum yaw rate conditions happening from the zero yaw points until the minimum and maximum yaw rates are reached. An additional interaction is observed between the bow and the bottom that generates a strong vortex due to the differences in relative side velocity at that region.

4.7 Summary

A 20/5 zigzag maneuver for the container ship KCS with discretized rotating propeller and moving rudder was performed in shallow water and results were compared with high resolution experimental data. For the first time the validation and verification study was conducted for the self-propulsion and maneuvering conditions. Since the grid study analysis performed at the nominal rudder rate, a maneuvering simulation with the actual experimental rudder rate for medium grid was repeated and results were compared with EFD. This study shows that experimental repeatability is excellent and this high repeatability was achieved by controlling very well the initial conditions.

The self-propulsion validation and verification study shows good grid convergence for the most relevant variables including RPM and propeller thrust and torque. The grid study for the zigzag maneuver was conducted using the same classical procedures designed for steady-state processes, and causes much higher grid uncertainties than the self-propulsion study. Several propeller parameters exhibiting divergence, indicating the complication of performing grid studies on naturally transient conditions such as ship maneuvers.

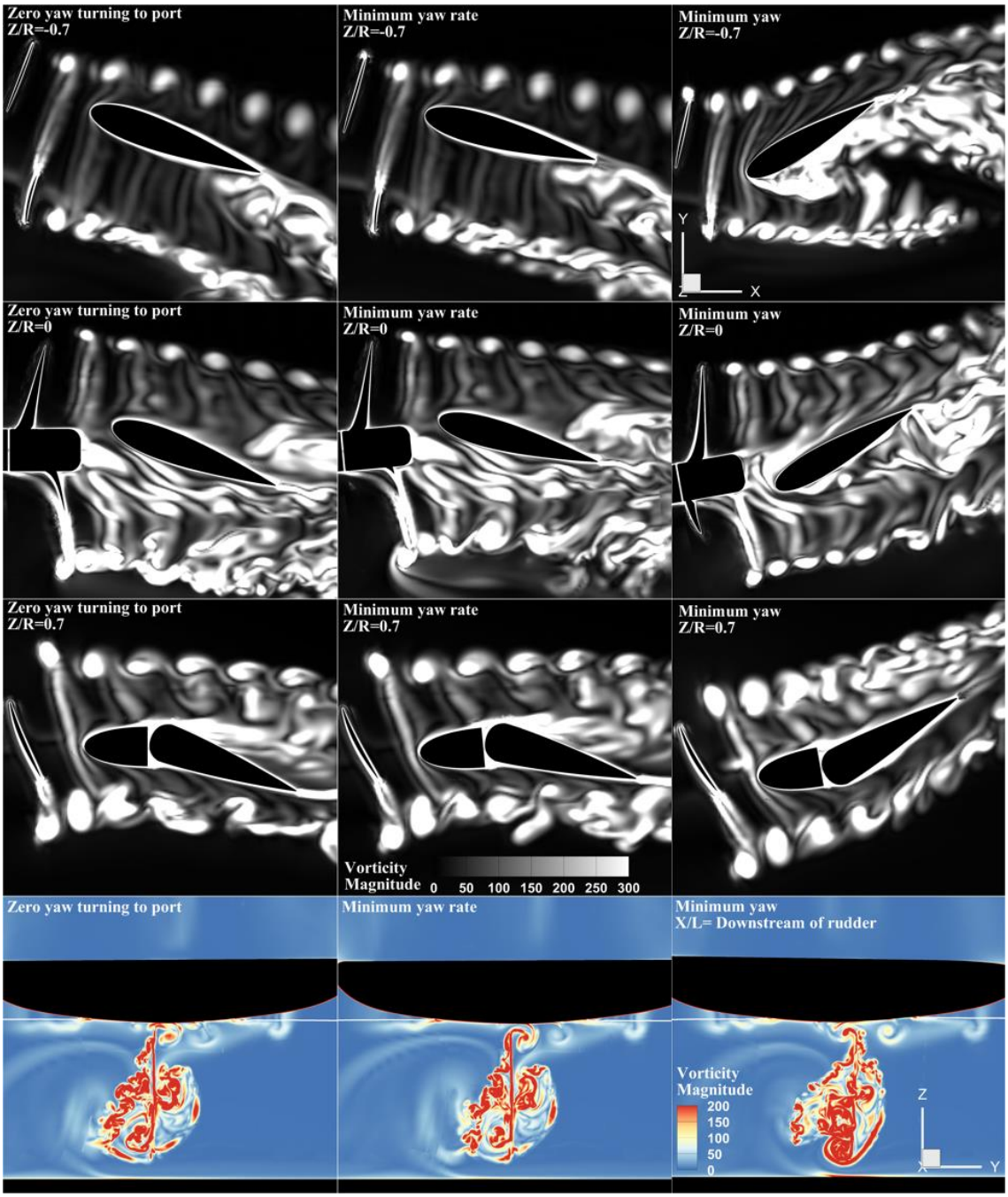

Figure 4.16 Horizontal sections 0.7R below the propeller axis (Z/R=-0.7, top row), at the propeller axis (Z/R=0, second row), and 0.7R above the propeller axis (Z/R=0.7, third row), and axial cross section at the trailing edge of the rudder (bottom row), showing vorticity magnitude at instantaneous points of zero yaw turning to port, minimum yaw rate and minimum yaw.

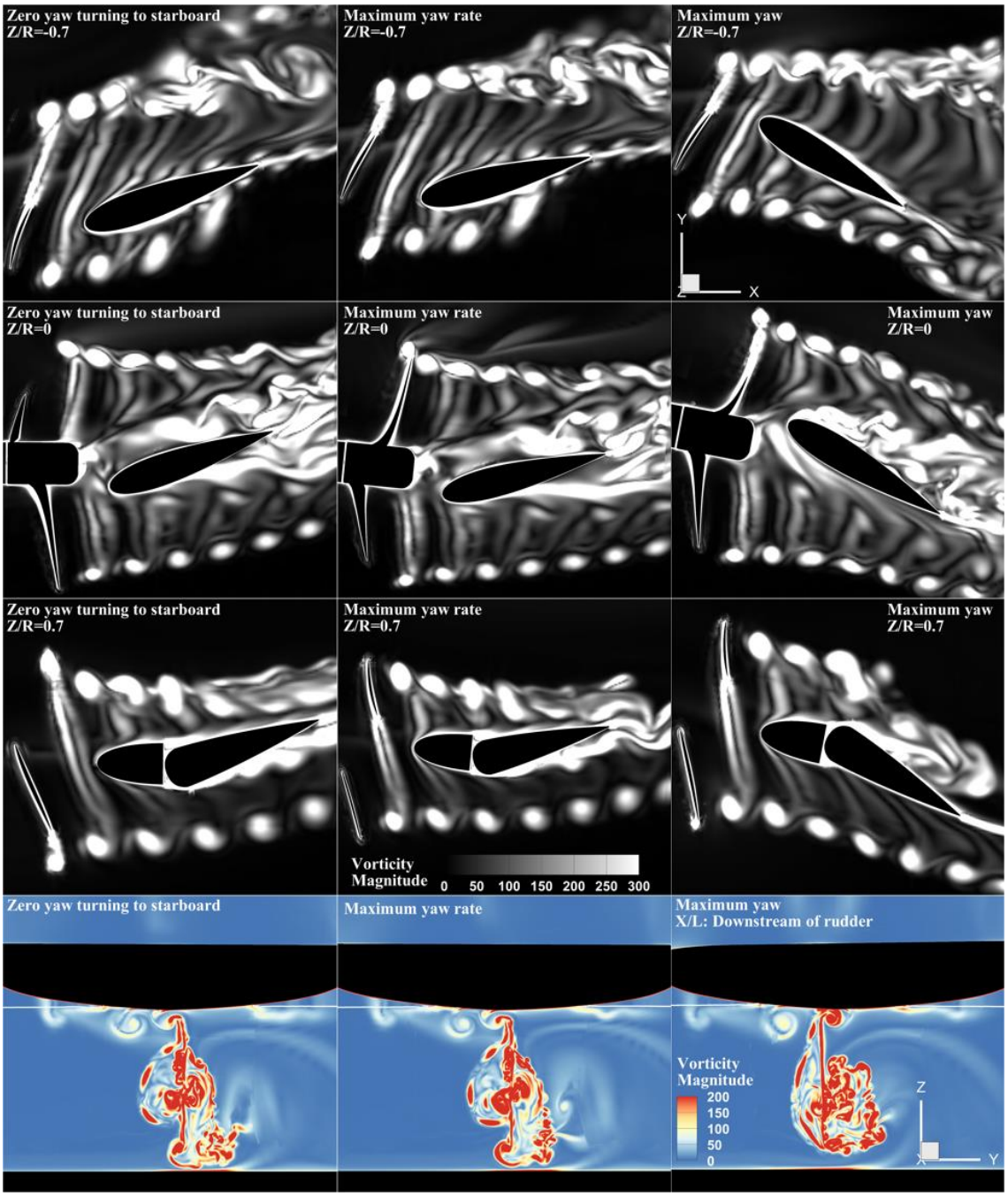

Figure 4.17 Horizontal sections 0.7R below the propeller axis (Z/R=-0.7, top row), at the propeller axis (Z/R=0, second row), and 0.7R above the propeller axis (Z/R=0.7, third row), and axial cross section at the trailing edge of the rudder (bottom row), showing vorticity magnitude at instantaneous points of zero yaw turning to starboard, maximum yaw rate and maximum yaw.

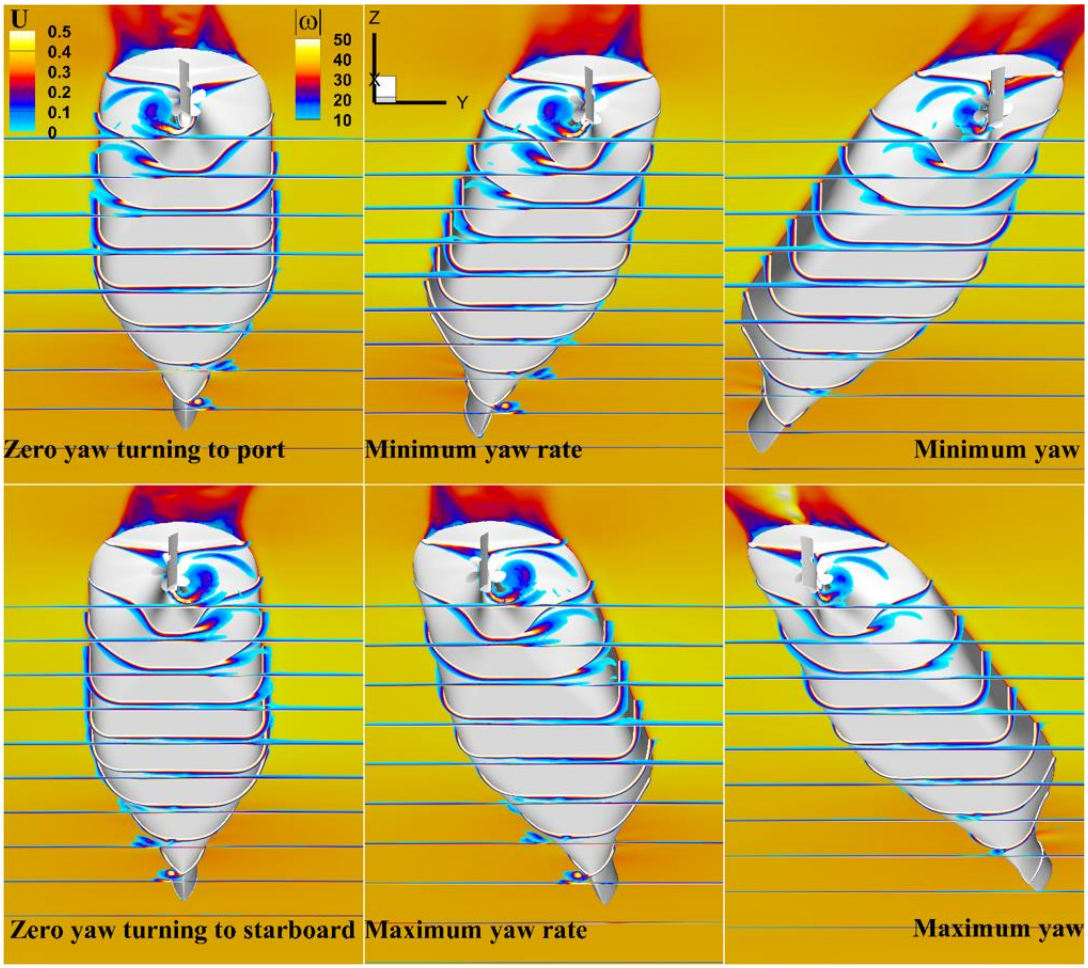

Figure 4.18 Cross sections colored with vorticity magnitude showing the boundary layer at instantaneous points of zero yaw turning to port, minimum yaw rate, minimum yaw, zero yaw turning to starboard, maximum yaw rate and maximum yaw. Free surface colored with velocity.

CHAPTER 5

COUPLED CFD/POTENTIAL FLOW METHOD FOR MANEUVERING SIMULATION

5.1 Overview

Direct simulations of the KCS container ship maneuvering in deep and shallow water with rotating discretized propeller and moving rudder were presented in chapters 3 and 4. While the results and comparisons with experimental data show that direct CFD simulations of modified and standard maneuvers are feasible, computational cost remains too high for many practical applications. A complete turn or zigzag maneuver simulation can take several weeks, depending on the length of the simulation to perform and the computational resources available. There are several possible strategies to reduce the computational time to perform direct CFD simulations of maneuvers. Some of these strategies include serial performance improvements, scalability improvements, single precision floating-point operation, decomposition of the overset process, local partially rotating frame for the propeller, and CFD/propeller model coupled approach. Use of coarser grids in calm water maneuvers yields good quality results for forces, moments and motions at a considerably lower computational cost, but the time step is still controlled by the rotational speed of the propeller, demanding 0.5 to 3 degrees of propeller rotation per time step. Coupling a dynamic overset CFD solver with a potential propeller code can dramatically reduce the computational time to perform maneuvering simulations by using one order of magnitude larger time step than direct simulation. In most cases a time step such that the ship advances one ship length in 200~400 time steps is adequate to handle the

flow around the ship. The propeller requires a much smaller time step, usually 10 times smaller, causing a significant increase in the total computation time.

In this chapter we investigate the extent of the influence of the presence of a rudder in the wake of a propeller in the propeller performance and the influence in maneuvers of the KCS container ship, in which case the rudder is very close downstream of the propeller. In order to apply coupled approach for maneuvering simulations it is important to estimate the effects of the propeller-rudder interaction because the rudder behind a propeller has a significant effect on the propulsive performance of a ship (Fumio Moriyama 1981). Both discretized propeller and PUF-14 model are used for rudder-propeller interactions simulations to make sure PUF-14 model is predicting propeller performance and rudder forces with a good accuracy in comparison with discretized propeller especially at propeller design point. For the first step of this study, the coupled approach performance is examined on OWCs simulations for SVA propeller. Propeller thrust and toque coefficients and overall propeller efficiency are computed for the range of advance ratios and results are compared with discretized propeller and experimental data. For the second step, the rudder interaction with propeller is considered to simulate the situations close to maneuvering conditions. Three different rudder angles are examined to evaluate the performance of coupled approach and comparing rudder/propeller interactions results to direct method. For the final step, modified zigzag maneuver simulation of KCS in deep water is performed with coupled REX/PUF-14 approach and results are compared with discretized propeller simulation and experimental data.

5.2 Propeller Modeling

Two approaches are considered to model the propeller. Discretized propeller for direct propeller simulation and PUF-14 model for coupled simulation. In discretized method, grids are created for the ship hull, rudder, and propeller including shaft, hub, and blades and the fluid flow and forces and moments are computed by REX. This method using a controller to determine the rotational rate of the propeller. Since this method uses direct gridding of the rotating propeller it is very expensive in terms of computational time. The force and torque of each propeller are projected into the non-inertial ship-fixed coordinates and used to compute an effective force and torque about the center of rotation, which is usually coincident to the center of gravity. Propeller location is determined in the static condition of the ship. When motions are involved, the propeller will move accordingly with the ship's motions.

The coupled REX/PUF-14 approach relies on PUF-14 to compute forces and moments, and REX to provide appropriate velocities to PUF-14 (Chase et al. 2013, Martin et al. 2015a).

PUF-14 has a capability to use as stand-alone code or coupled with other CFD codes. The current version of the PUF-14 used in this thesis was designed for coupled operation with CFD solver REX and details of the implementation can be found in Martine et al. (2015a). PUF-14 is a vortex lattice lifting-surface propeller code developed by Warren in MIT (1999). The B-spline surfaces are used to define the blade geometry and blade thickness is modeled via sources at the vortex lattice control points. Propeller hub is modeled by vortex images and propeller wake is described by using a vortex lattice. The

effective inflow for the vortex lattice solution is predicted from given wake field and propeller induced velocities.

Figure 5.1 depicts the details of coupling process between CFD code REX, propeller model PUF-14, and overset solver Suggar. At each time step REX computes the fluid flow and the rotational speed of the propeller, this last through the speed controller. The vortex wake geometry at each time step is updated by relocation of the last geometry by the current velocity field. PUF-14 maintains the geometry of the vortex wake and singularity strength in order to use in the next calculation steps. PUF-14 then provides REX with selected locations on the propeller disc and the wake, where REX evaluate fluid flow velocities. REX then sends these velocities and the new operational conditions (dependent on the propeller rotational speed) to PUF-14. PUF-14 computes then propeller forces and moments and send them to REX, which uses them in the 6DOF solver to predict the new state of the ship and compute the new flow field, advancing to the next time step and repeating the process. Details on the lagged coupling mode operation are discussed in Martin et al. (2015a). In this thesis propeller shaft and body forces are computed for a full rotation of the propeller at each time step, resulting in a distribution of forces on the propeller swept volume. This approach is more stable than time-accurate treatment of the propeller (see Calcagni et al. 2017 for an example where a time accurate approach is followed) but still reproduces well the response of the propeller to the ship wake, see Martin et al. (2015a) for details.

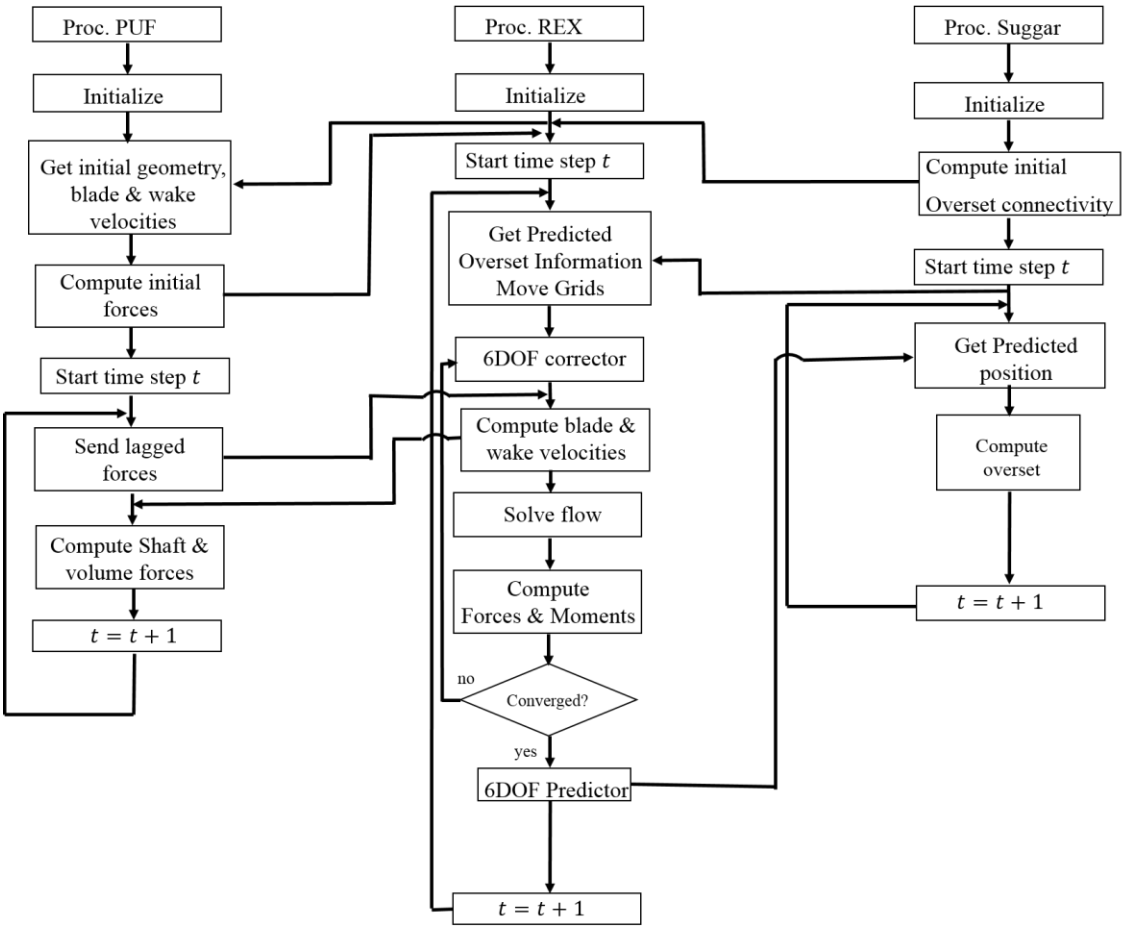

Figure 5.1 Flow chart depicting exchanges between REX, PUF-14, and Suggar, Martin et al. (20015a).

5.3 Grids and Geometry for Propeller/Rudder Interaction Study

Before using coupled REX/PUF-14 approach to perform maneuvering simulations, simpler conditions are studied for both discretized propeller and PUF-14 methods. SVA propeller model the generic KRISO Very Large Crude oil Carrier (KVLCC) rudder are used as working geometries. Figure 5.2 shows the overset grid topology at the solid surfaces and also shows the propeller and rudder positions for both discretized propeller

and coupled REX/PUF-14 methods. The overset grid system for discretized method consists of 16 grid blocks, including grids for propeller, rudder, refinements, and background. The total number of grid points is 4.6 million for discretized propeller method and 3.25 million for coupled REX/PUF-14 methods. Table 5.1 summarizes the dimensions of the grids that used in simulations. The difference in number of grid points is another advantage of the coupled method, as not only the blade grids are eliminated, but also much coarser wake refinement is used, since it is no longer require to resolve tip vortices. The chosen cylindrical grid for coupled REX/PUF-14 case is 181 axially by 51 radially by 61 azimuthally. The grid is partly coarse but has been proven adequate for OWCs computations. As will be discussed later in this chapter, a finer grid size is required for cylinder for maneuvering simulations to capture the flow separation on rudder surface properly.

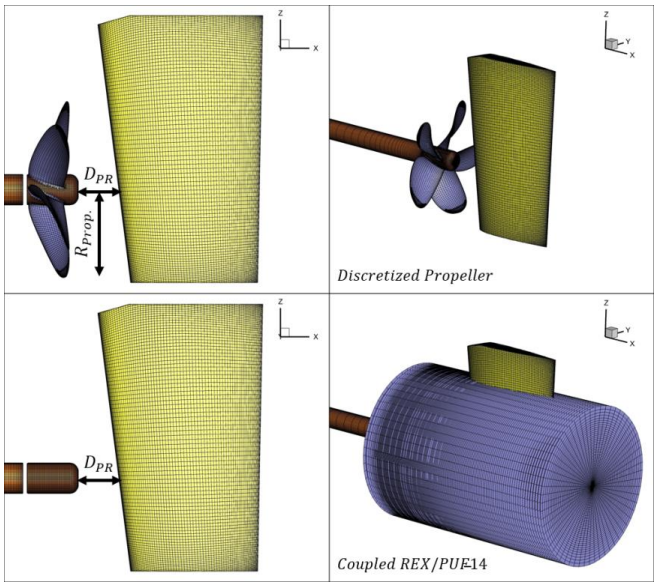

Figure 5.2 Discretized propeller and PUF-14 model grid topology.

Table 5.1 Grid system used for Propeller/Rudder geometry in discretized and PUF-14 methods.

Grid	Size	Total Points	Grid Type	Model
Shaft	$101 \times 42 \times 91$	$386\ K$	"O"	Disc./PUF
Hub	$101 \times 22 \times 91$	$202\ K$	"O"	Disc./PUF
Blades	$5 \times 101 \times 42 \times 91$	$524\ K$	"O"	Disc. Only
Tip	$5 \times 101 \times 22 \times 91$	$101\ K$	Wrapped	Disc. only
Rudder Stb	$80 \times 40 \times 109$	$349\ K$	Wrapped	Disc./PUF
Rudder Port	$80 \times 40 \times 109$	$349\ K$	Wrapped	Disc./PUF
Refinement	$181 \times 51 \times 121$	$1.1\ M$	Cylindrical	Disc.
Refinement	$181 \times 51 \times 61$	$563\ K$	Coupling cylindrical	PUF
Background	$153 \times 95 \times 95$	$1.4\ M$	Cartesian	Disc./PUF
Total		$4.6\ M$		Disc.
Total		$3.25\ M$		PUF.

5.4 Propeller/Rudder Simulation Conditions and Cases

The goal of this chapter is to investigate the performance of advance propeller model PUF-14 coupled with CFD code REX for maneuvering applications. To achieve this goal, an estimation of propeller-rudder interaction effects on the propulsive performance of the propeller need to be considered for both discretized propeller and PUF-14 propeller model. The simulation matrix consists of cases with the SVA propeller and PUF-14 model and the rudder at different distances respect to the propeller. Also, rudder deflections of 20 and -20 degrees are considered to simulate the maneuvering conditions. Table 5.2 summarizes all the simulation conditions for both discretized propeller and coupled REX/PUF-14 methods. All variables are non-dimensionalized using a reference velocity

U_0 taken to be the KCS ship service speed and a length scale taken to be the length between perpendiculars L_{pp}.

Table 5.2 Simulation matrix.

Advance Coefficient	Rudder/Propeller Gap		Rudder Angle			Model
0.2	0.2	0.4	20	−20	0	*Discretized*
	0.8	*No Rudder*				$PUF-14$
0.4	0.2	0.4	20	−20	0	*Discretized*
	0.8	*No Rudder*				$PUF-14$
0.6	0.2	0.4	20	−20	0	*Discretized*
	0.8	*No Rudder*				$PUF-14$
0.8	0.2	0.4	20	−20	0	*Discretized*
	0.8	*No Rudder*				$PUF-14$
1	0.2	0.4	20	−20	0	*Discretized*
	0.8	*No Rudder*				$PUF-14$

Simulations are conducted in model scale, with the parameters consistent with the operational conditions for the experimental KCS model. Propeller advance coefficient defines: $J=\frac{U_{fullspeed}}{nD}$ where $U_{fullspeed}$ is flow velocity, n is propeller rotational speed and D is propeller diameter. Therefore, the dimensionless propeller rotational speed, forces and moments are $n^*=\frac{nL_{pp}}{U_0}$, $F^*=\frac{F}{\rho U_0^2 L_{pp}^2}$ and $M^*=\frac{M}{\rho U_0^2 L_{pp}^3}$, respectively, where ρ is the water density. In discretized propeller method the time step is chosen to rotate the propeller

1.58 degrees per time step and constant $n^* = 29.43$ is used for all advance coefficients and $U_{fullspeed}$ is changed for each advance coefficients to adjust flow field velocity. For coupled REX/PUF-14 method, time step is chosen to guarantee all advance coefficients have the same amount of rotation. The rotated angle per time step for coupled REX/PUF-14 simulations is 15.8 degrees which depicts remarkable reduction in computational time.

5.5 Coupled REX/PUF-14 Results

5.5.1 Open Water Curve Simulations

In order to study the propeller performance under different operational conditions, the open water simulations are performed. Figure 5.3 shows thrust and torque coefficients and propeller efficiency for discretized propeller, coupled REX/PUF-14 and experimental data from Schiffbau-Versuchsanstalt Postdam GmbH (SVA). The friction coefficient, an input in PUF-14, was adjusted to match the friction of the discretized propeller solution. The drag coefficient used within PUF-14 is 0.0115, which is consistent with the chord-based Reynolds number of 1×10^5. The friction coefficient is calculated based on the friction force on the discretized propeller blade in the same operational condition as PUF-14. Simulations are performed at Reynolds number $Re_c = 7.51 \times 10^6$ based on the $L_{pp} = 4.4141\ m$ and $U_0 = 1.701\ m/s$. Coupled REX/PUF-14 results show good agreement with experiments, even better than discretized propeller simulation results due to the adjusting the friction coefficients. The results are particularly good at the point of maximum efficiency, which matches the data almost perfectly. The standard definitions for propeller thrust, K_T, and propeller torque, K_Q, coefficients and propeller efficiency η were used:

$$K_T = \frac{F_x}{\rho n^2 D^4}; K_T = \frac{M_x}{\rho n^2 D^5}; \eta = \frac{J K_T}{2\pi K_Q} \tag{5-1}$$

Where ρ is the fluid density, n the propeller rotational speed, D the propeller diameter, F_x and M_x are axial propeller thrust and torque, respectively, and J is the advance coefficient, expressed as:

$$J = \frac{U}{nD} \tag{5-2}$$

Where U is the advance speed or incoming flow velocity. Figure 5.4 shows instantaneous and mean longitudinal velocity contours on a horizontal cross section through the center of the shaft, for discretized propeller and coupled REX/PUF-14 at $J = 0.8$. By observing instantaneous solutions it is clear that most of the vortical structures resolved by the discretized propeller approach (tip vortices, trailing edge vortices, hub necklace vortices, etc.) cannot be captured with the coupled REX/PUF-14 approach, as discussed in Martin et al. (2015b). The mean solutions show good agreement between the two methods, with the largest differences observed in the hub wake, which is wider in the case of coupled REX/PUF-14 approach and it also shows higher velocity defects.

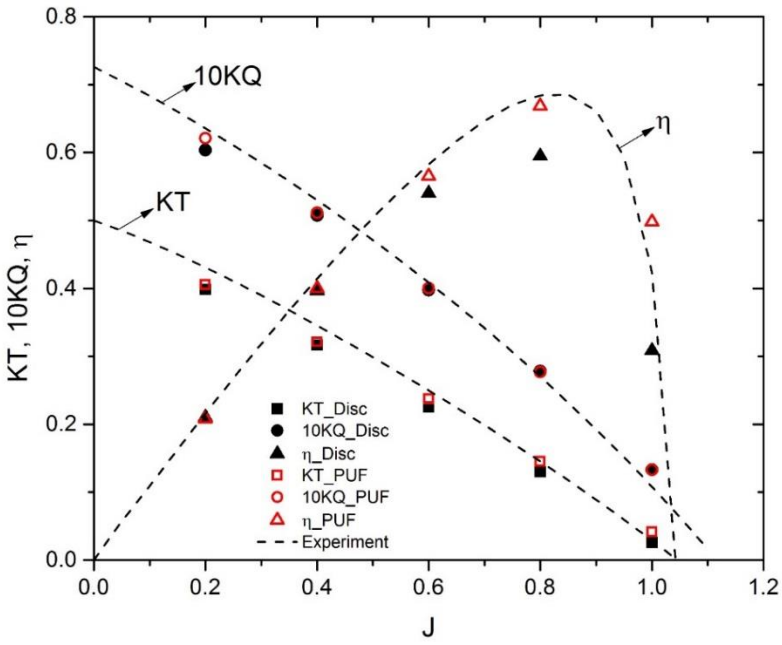

Figure 5.3 Open water curve for propeller SVA and PUF-14 model.

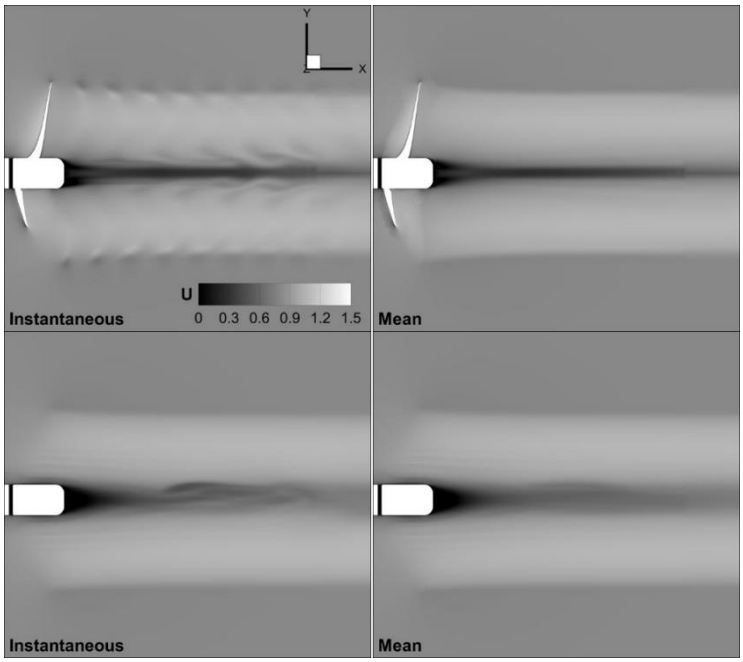

Figure 5.4 Longitudinal fluid velocity at J=0.8 for discretized propeller (top) and coupled REX/PUF-14 (bottom) for a horizontal plane across the shaft center.

5.5.2 Effects of Presence of Rudder on Propeller Performance

The effects of the presence of a rudder on the propeller performance are studied in this section. Figures 5.5 - 5.8 depict the effects of the propeller-rudder gap (D_{PR}), advance coefficients, and rudder angles on the thrust and torque coefficients. Since there is no experimental data available for the same propeller and rudder geometries used in these simulations, coupled REX/PUF-14 results only compared with discretized propeller results with similar propeller/rudder configuration. At higher loads ($J = 0.2$ and 0.4, Figs. 5.5 and 5.6) differences between discretized propeller and coupled REX/PUF-14 model are significant, notably at $J = 0.2$ and smaller propeller/rudder gap. Discretized propeller simulations predict that the thrust increases as the gap between propeller and rudder decreases, and also increases when the rudder is turned either way, but slightly more when turned to port. This effect is caused by the blockage of the rudder that effectively decreases the advance velocity and the advance coefficient, resulting in higher thrust. Propeller torque coefficients show similar trend, but the rudder turning to port results in more torque and turned to starboard less torque than with the rudder straight. At high loading condition, J=0.2, the coupled REX/PUF-14 approach predicts opposite trends, with the torque and thrust decreasing when the rudders are turned, but following the trends observed for discretized propeller at higher advance coefficients. According to Black and Michael (2003), adverse trend of propeller performance at high loads is a common limitation with lifting surface codes and is associated to not capturing the wake roll up and separation from blade leading edge properly. This problem becomes more striking when a rudder is located downstream of the propeller and propeller wake being distorted massively by the rudder.

For lower loading and advance coefficients close to design point condition, coupled REX/PUF-14 results show notably better agreement with discretized propeller results. Figure 5.9 displays longitudinal velocity contours at the design point $J = 0.8$ on a horizontal cross section through the center of the shaft, for discretized propeller and coupled REX/PUF-14 at different rudder-propeller gap sizes. In order to have fair comparison the discretized propeller solutions are averaged over one propeller rotation. For all gap sizes the agreement between the two approaches is good and the detected propeller/rudder features are fairly similar. The main differences between two methods are observed at propeller hub due to the different strength of the hub vortex. Coupled REX/PUF-14 results show higher vorticity and velocity defect on the hub vortex which results in smaller velocity coming through the propeller. This is more evident when the rudder is straight compare to deflected rudder. This condition is very local, since the area ratio of the hub vortex to the propeller disk is very small, therefore, most of the rudder will not be affected by this flow.

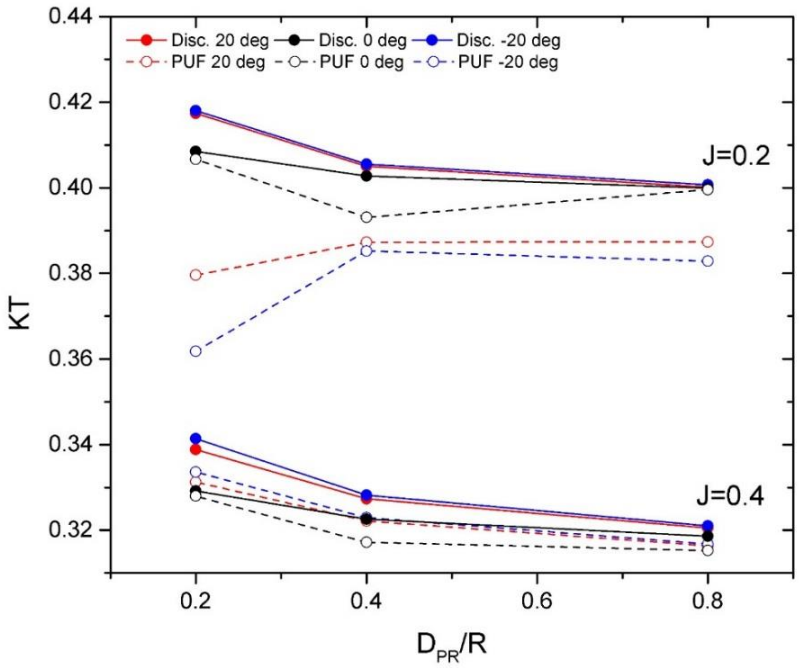

Figure 5.5 Effect of propeller-rudder gap sizes on thrust coefficient for J=0.2 and J=0.4.

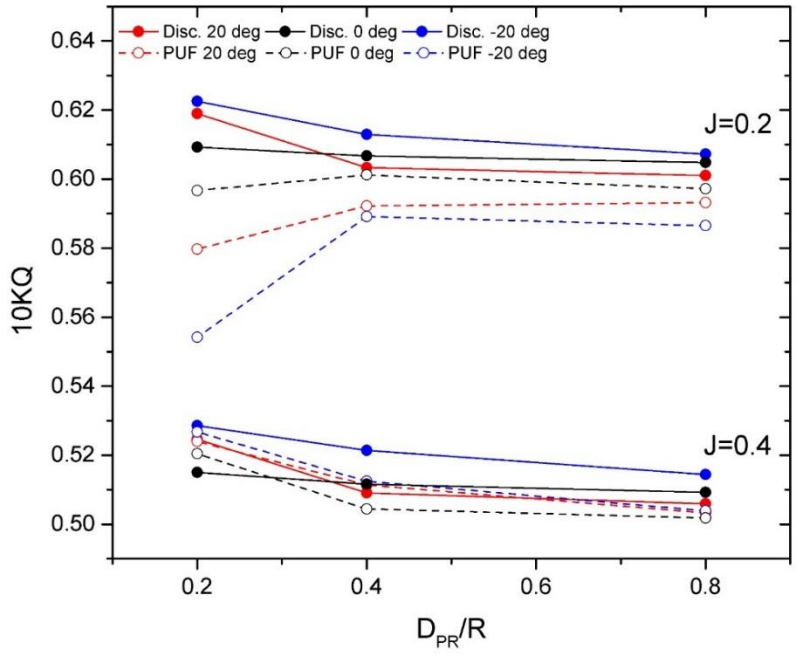

Figure 5.6 Effect of propeller-rudder gap sizes on torque coefficient for J=0.2 and J=0.4.

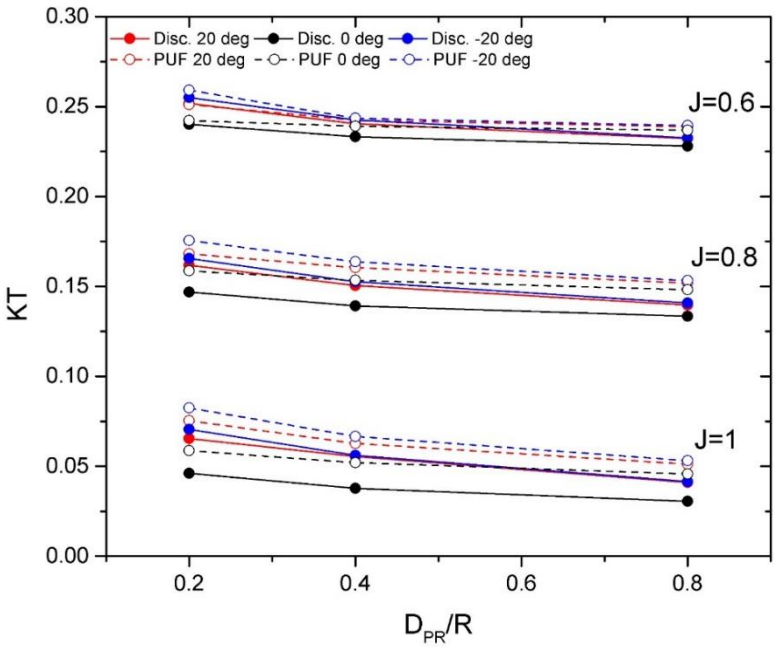

Figure 5.7 Effect of propeller-rudder gap sizes on thrust coefficient for J=0.6, J=0.8 and J=1.

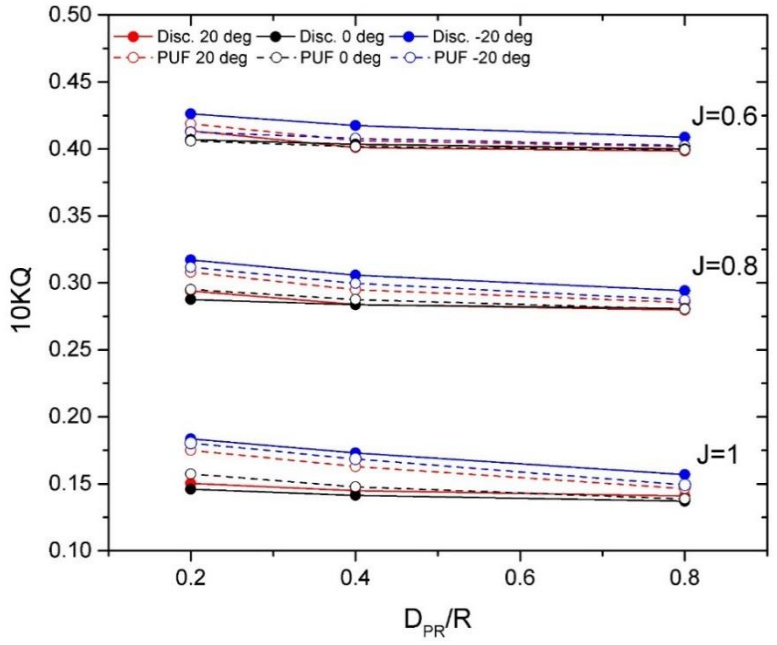

Figure 5.8 Effect of propeller-rudder gap sizes on torque coefficient for J=0.6, J=0.8 and J=1.

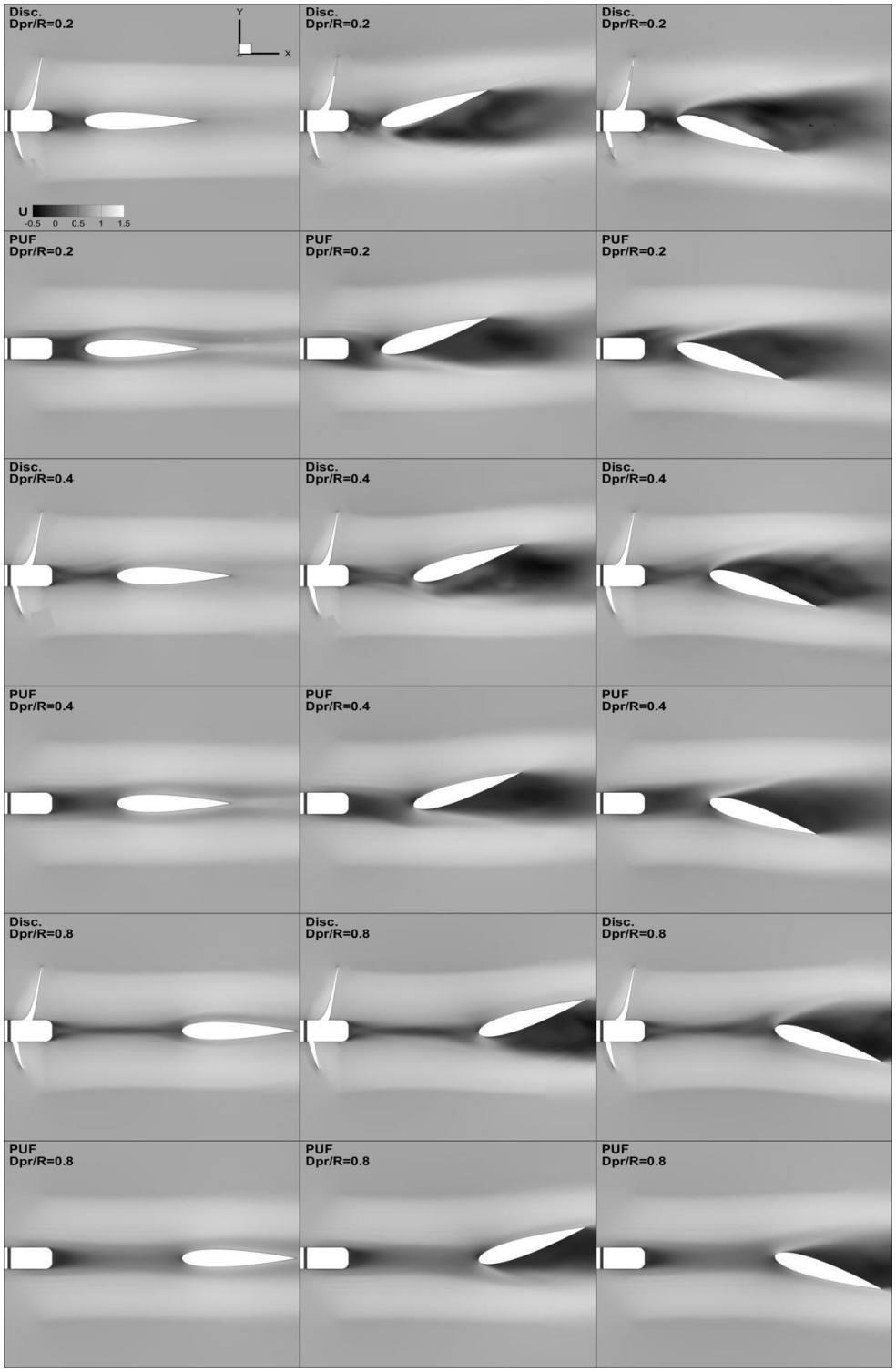

Figure 5.9 Longitudinal fluid velocity at J=0.8 and different propeller/rudder gaps. Discretized velocity contours are for solutions averaged over one rotation and rudder angles are 0 deg. (first column), 20 deg. (second column), and -20 deg. (third column).

Fig. 5.10 shows the propeller performance curve in presence of the rudder, which includes rudder angles of $0, 20, and -20$ degrees. The propeller/rudder gap size $D_{PR}/R = 0.2$ is considered here to mimic the actual propeller/rudder gap in KCS. The main effect of turning the rudder on the propeller performance is an increase in the blade loading, a direct result of the lower flow velocities at the propeller plane caused by the presence of the rudder. In Fig. 5.10, the efficiency of the propeller is computed based on the far-field velocity instead of actual advance velocity, which is unknown in this computation. By increasing advance coefficients the error in computing efficiency is more evident but still displays the effects of the rudder on propeller performance. The coupled REX/PUF-14 approach under-predicts thrust and torque respect to discretized propeller computations at high load conditions, but overall results are good and consistent with Fig. 5.3, and within acceptable range for most engineering purposes for advance coefficients between 0.4 and 0.8. Corrections to computations of the wake within PUF-14 to account for the presence and operation of the rudder may yield better results.

Figures 5.11 to 5.14 show the turbulence kinetic energy for propeller/rudder configuration at J=0.6 for both discretized propeller and coupled REX/PUF-14 approaches. In Fig. 5.11 the K-contours display at x-constant plane downstream of the propeller wake and upstream of the rudder and also z-constant plane at center of the shaft. Due to presence of the propeller tip vortices and stronger hub vortex in discretized propeller method, the turbulence kinetic energy significantly higher than coupled REX/PUF-14 approach. Similar comparison is observed for velocity fluctuations at the propeller/rudder region. As can be seen, lower velocity fluctuation and weaker turbulence structure around the rudder is evident in PUF-14 propeller model results.

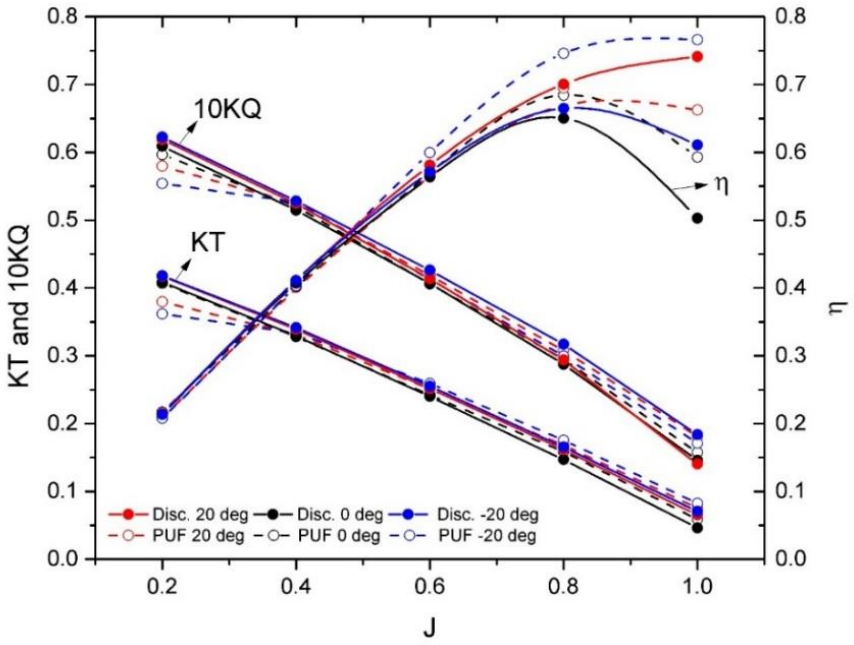

Figure 5.10 Propeller performance curve in presence of the rudder for discretized propeller and coupled REX/PUF-14 for D_PR/R=0.2 at 0,20,and-20 degree rudder angles.

Figure 5.15 shows the average velocity vectors at x-constant plane downstream of the propeller for discretized propeller and coupled REX/PUF-14 approaches. The momentum flux results based on the velocity averages implying that PUF-14 model generates up to 3 times higher flux at propeller wake respect to the discretized propeller. The presence of stronger turbulent structures due to blade tip vortices in discretized propeller approach results in higher velocity deficit than PUF-14 propeller model. This results are also correlated with the results in Fig. 5.11.

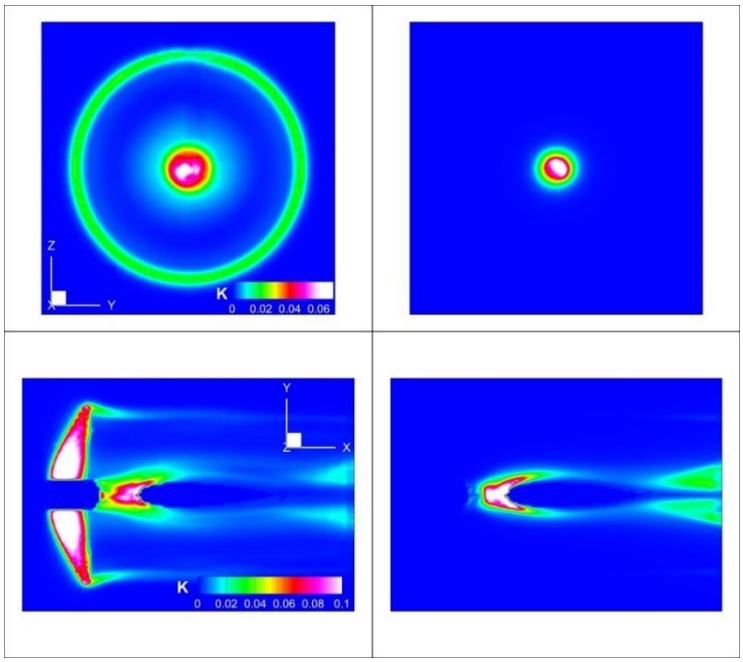

Figure 5.11 Turbulence kinetic energy at cross sections downstream of the propeller (top row) and horizontal cross section at the center of the shaft (bottom row) for discretized propeller (1st column) and coupled REX/PUF-14 (2nd column).

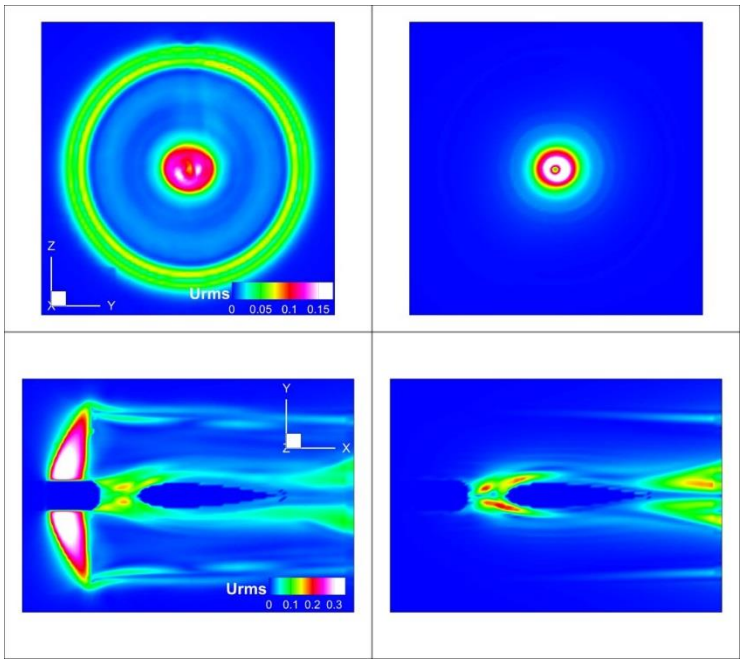

Figure 5.12 Velocity fluctuations $Urms$ at similar cross sections as Fig.5.11.

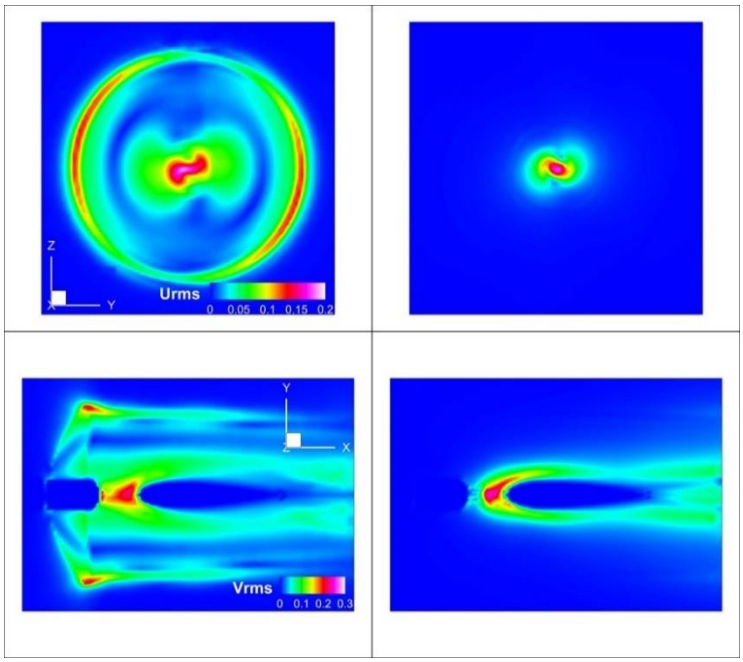

Figure 5.13 Velocity fluctuations $Vrms$ at similar cross sections as Fig.5.11.

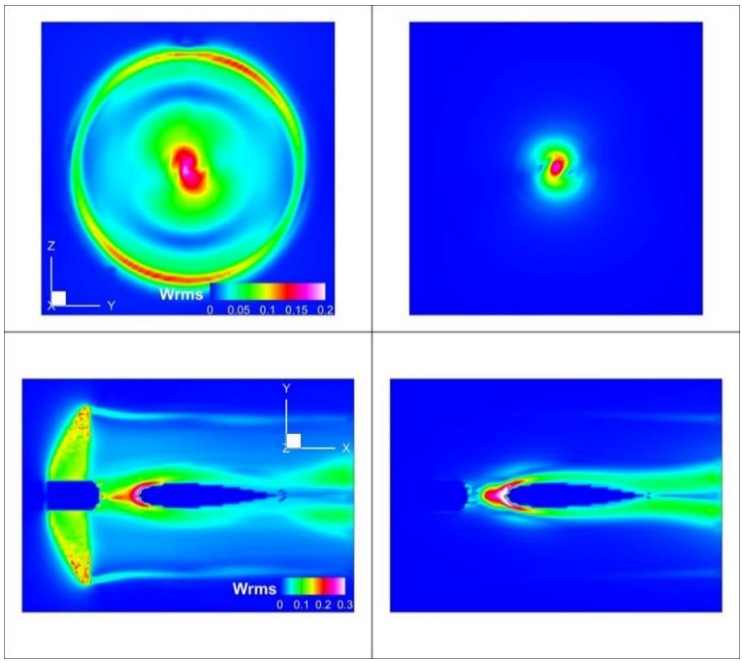

Figure 5.14 Velocity fluctuations $Wrms$ at similar cross sections as Fig.5.11.

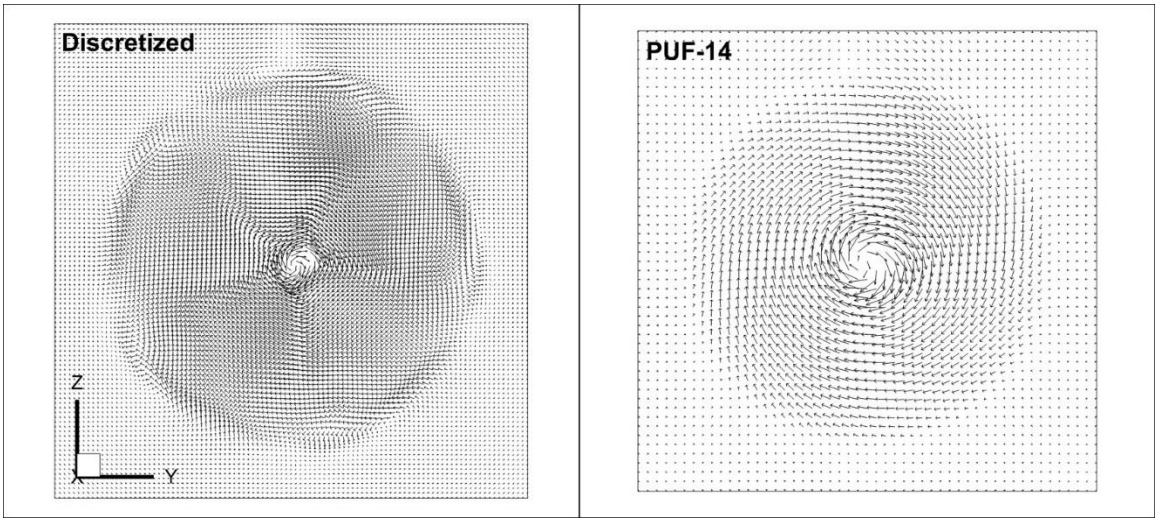

Figure 5.15 Average axial velocity vector at cross section downstream of the propeller.

5.5.3 Effects of Presence of Propeller on Rudder Performance

The effects of presence of propeller on the rudder are studied in this section. As discussed in Fig. 5.9, discretized propeller and coupled REX/PUF-14 predict similar mean flow patterns around the rudder. The results for rudder forces under different propeller loading conditions are presented here for rudder angles of 0, 20, and -20 degrees. To evaluate the effects of the presence of the propeller on the rudder forces it is more convenient to define the change in force as:

$$\Delta F_{X_{Rudder}} = \frac{F_{X_{Rud+Prop}} - F_{X_{Rudder}}}{F_{X_{Rudder}}} \tag{5-3}$$

$$\Delta F_{y_{Rudder}} = \frac{F_{y_{Rud+Prop}} - F_{y_{Rudder}}}{F_{y_{Rudder}}} \tag{5-4}$$

where $\Delta F_{X_{Rudder}}$ and $\Delta F_{y_{Rudder}}$ are the fractional changes in rudder forces caused by the propeller presence respect to the rudder forces with no propeller. $F_{X_{Rud+Prop}}$ and $F_{y_{Rud+Prop}}$ are the rudder forces with propeller/rudder configuration, and $F_{X_{Rudder}}$ and $F_{y_{Rudder}}$ are the rudder forces in absence of the propeller.

Effects of the presence of the propeller on the rudder forces at 0, 20, and -20 degrees rudder angles for both discretized propeller and coupled REX/PUF-14 are shown in Fig. 5.16. At higher propeller loads (low advance coefficient) the coupled approach under-predicts thrust, resulting in a weaker propeller wake and consequent lower forces on the rudder respect to the discretized approach. At lower propeller loads (high advance coefficient) which is closer to the maneuvering operation conditions, both approaches predict similar results.

Fig. 5.17 displays the instantaneous contours of axial velocity profiles at planes immediately upstream and downstream of the rudder for J=0.8 for both discretized propeller and coupled REX/PUF14. The overall flow pattern presenting fairly similar results, with the main difference due to a stronger velocity defect at the propeller hub for the coupled approach which is consistent with results in Fig. 5.16. The deflected flow pattern in deflected rudder condition showing similar tip vortices detaching from the rudders and a significant momentum defect in the rudder wake. Smoother boundary is presented between the far-field and the high-velocity region in propeller wake in the discretized propeller approach while sharper boundary is observed in coupled REX/PUF-14 approach. The main reason of the discrepancies between two approaches is due to the additional effective mixing caused by the propeller tip vortices in discretized propeller method, which are not presence in the coupled REX/PUF-14 approach.

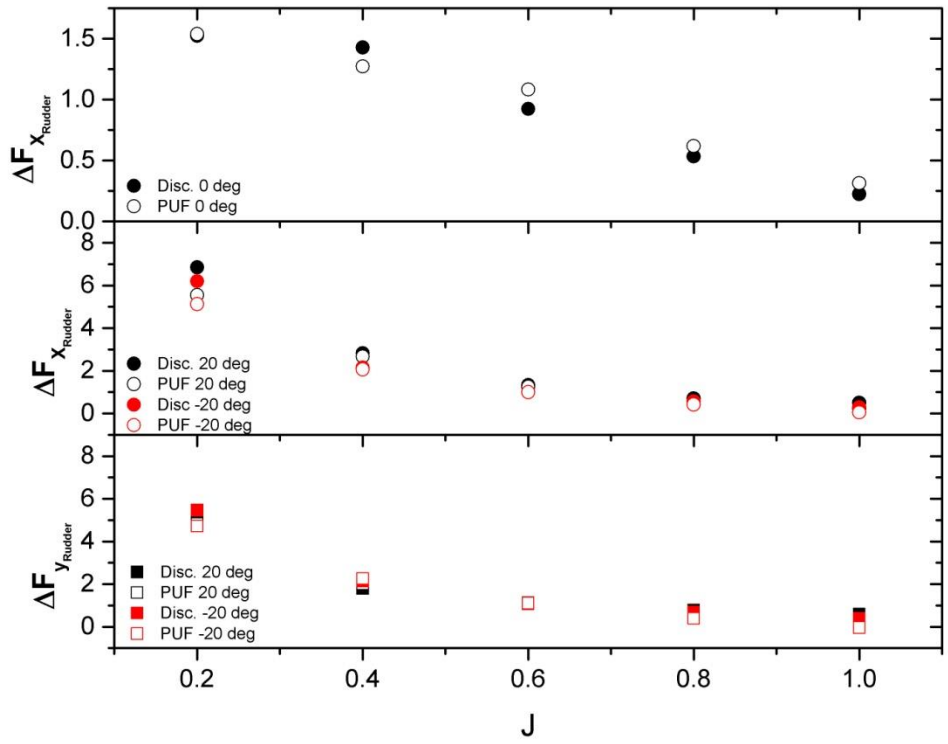

Figure 5.16 Effect of propeller load on rudder drag force at 20 and -20 deg. rudder angle.

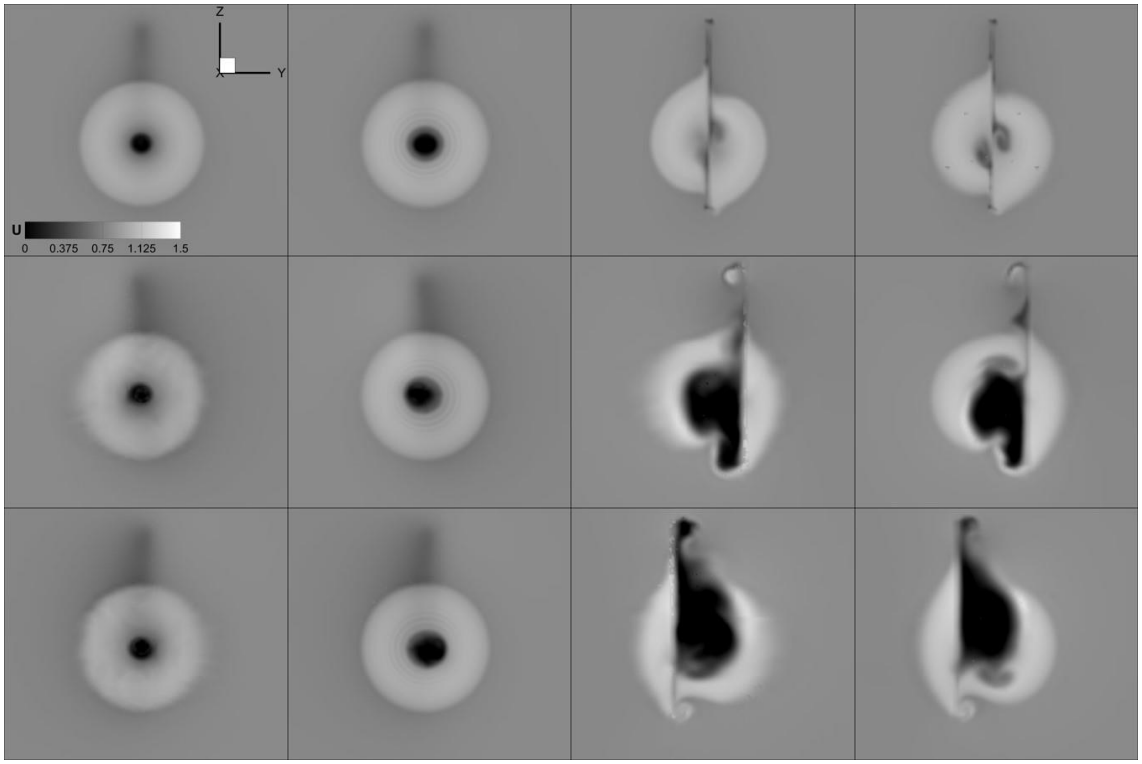

Figure 5.17 Axial velocity at J=0.8 at planes immediately upstream of the rudder (left two columns) and downstream of the rudder (right two columns) for discretized propeller (first and third columns) and coupled REX/PUF-14 (second and fourth columns). 0, 20, and -20 deg rudder angles are presented in top, center and bottom, respectively.

5.6 Grid Studies for Coupled REX/PUF-14 Propeller/Rudder Simulations

In order to evaluate the grid numerical uncertainties of the solutions for the coupled REX/PUF-14 approach, a grid study was performed in a propeller/Rudder configuration. The grid study was conducted for advance coefficient, $J = 0.6$ and rudder angle $\delta = 20\ degrees$, values representative of maneuvering conditions.

As previously stated in section 4.5.1 of Chapter 4, the first step for estimation of the grid uncertainty (U_G) is the convergence study. The refinement ratio $r_G = \sqrt{2}$ is used

on each direction of the grids and three systematically refined grid sizes are summarized in Table 5.3. Solutions on these grids are compared to estimate the grid uncertainty.

Convergence studies were performed on propeller thrust and torque coefficients and rudder axial and side forces. Rudder dimensionless forces are defined as: $CF_{X_{Rudder}} = \frac{F_{X_{Rudder}}}{0.5\rho U_0^2 L_{pp}^2}$, $CF_{y_{Rudder}} = \frac{F_{y_{Rudder}}}{0.5\rho U_0^2 L_{pp}^2}$. The simulations were run until solutions reached statistically stationary condition, and then the last few propeller rotations were used to obtain the final values.

Verification study results are summarized in Table 5.4 and Fig. 5.18 shows all obtained propeller and rudder coefficients for the three grids. The grid study shows monotonic convergence for propeller thrust coefficient, KT with $R_G = 0.75$, propeller torque coefficient $10KQ$ with $R_G = 0.84$. The rudder side force coefficient, $CF_{y_{Rudder}}$ shows oscillatory convergence with $R_G = -0.83$. The uncertainties for propeller thrust and torque are $U_G = 0.78\%S_2$ and $U_G = 3.22\%S_2$, respectively. The grid uncertainties of propeller thrust and torque coefficients are suggesting that the effects of the grid changes are small on the results for the present range of grid sizes. The grid uncertainty is higher than for rudder side force, with $U_G = 8.14\%S_2$ and exhibit oscillatory convergence. The only parameter shows oscillatory divergence is rudder axial force ($CF_{X_{Rudder}}$) with $R_G = -1.35$. The axial force results for all grids show that the highest deviation belongs to the medium grid with only 1.5% deviation from the average. The main cause for changes are large force fluctuations due to unsteady separation in the rudder.

Figure 5.19 shows instantaneous velocity contours at a horizontal plane cross section through the propeller shaft and plane and an axial plane immediately downstream

of the rudder for 20 degree rudder angle and $J = 0.6$ for all grids. Massive separation is observed on the suction side of the propeller with higher resolution of the flow structures for finer grids. Inspecting Fig. 5.19 shows the rudder axial force does not converge, and grids considerably finer than those used in this study may be required to achieve grid convergence.

Table 5.3 Grid dimensions for refinement study.

Grid	Grid Points
1- Coarse	1.1 M
2- Medium	3.2 M
3- Fine	8.7 M

Table 5.4 Coupled REX/PUF-14 grid convergence. $U_{GC}$and U_G are $\%S_2$.

Variable	Coarse Grid	Medium Grid	Fine Grid	R_G	P_G	C_G	U_{GC}	S_C	U_G	Convergence Type
KT	0.2612	0.2603	0.2597	0.75	0.81	0.32	0.53	0.259	0.78	Monotonic
$10KQ$	0.4361	0.4329	0.4302	0.84	0.51	0.19	2.60	0.430	3.22	Monotonic
$1000CF_{x_{Rudder}}$	0.3037	0.2801	0.3120	-1.35	-	-	-	-	-	Divergence
$-100CF_{y_{Rudder}}$	0.0716	0.0616	0.0700	-0.83	-	-	-	-	8.14	Oscillatory

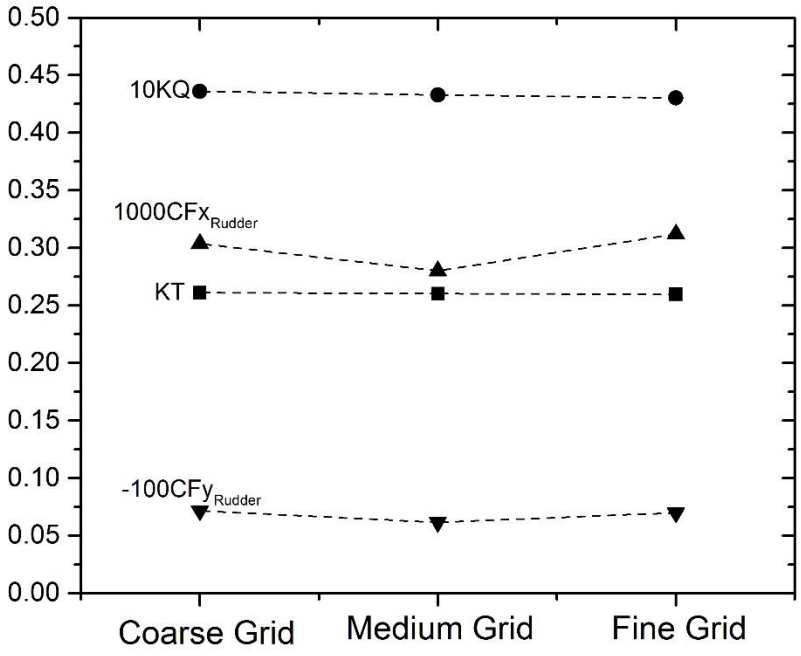

Figure 5.18 Propeller and rudder force and moment coefficients for coarse, medium, and fine grids.

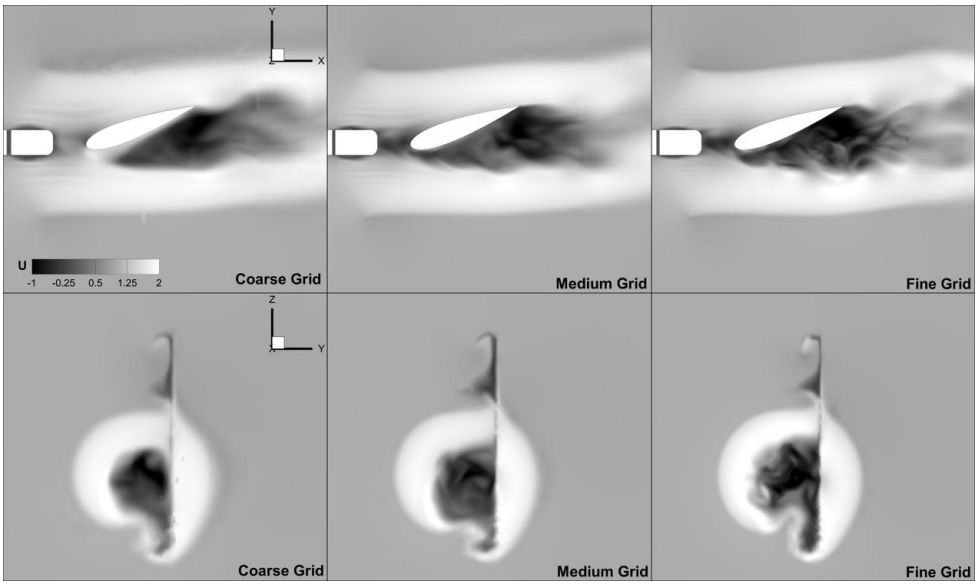

Figure 5.19 Velocity contours at a horizontal plane cross section through the propeller shaft and plane and an axial plane immediately downstream of the rudder at 20 degree rudder angle and J=0.6 for coarse, medium, and fine grids.

5.7 KCS Zigzag Maneuver Simulations with Coupled REX/PUF14 Approach

In this section the performance of the coupled REX/PUF-14 approach is evaluated for the generic KCS containership in a 15/1 zigzag maneuver, and results are compared with discretized propeller simulations and experimental data for trajectories, motions, forces, and moments.

5.7.1 Geometry and Simulation Conditions

Simulations are performed in deep water for model scale conditions as described in detail in Chapter 3 and a limited description include herein. The Reynolds and Froude numbers are $Re = 7.51 \times 10^6$ and $Fr = 0.26$ similar to the discretized propeller simulations discussed in Chapter 3. Grid studies performed for KCS self-propulsion and zigzag maneuvers suggest that medium grid are appropriate to capture integrated values like forces, moments and motions, and thus a medium size grid is selected herein. The overset grid system consists of blocks, including grids for hull, propeller, rudder, refinement and background. The propeller hub is kept but the blades are discarded and replaced by a cylindrical coupling grid, as required to interact with PUF-14 (Martin et al. 2015) and shown in Fig. 5.20. CFD code REX and propeller model PUF-14 are exchanging information at propeller disk volume and in the wake. The overset grid system consists of 28 grid blocks, including grids for hull, rudder, cylindrical propeller refinement grid, other refinements and background. Coarse, medium and fine cylindrical coupling grids were explored. These 28 blocks are distributed in 101 or more processors for parallel processing. The total number of grid points ranges from 18.1 to 20.9 million for the coarse to the fine

cylinder grid. Table 5.5 shows details of the grid system and the hierarchy of bodies used to run the simulation with the coupled REX/PUF-14 approach.

The simulations were performed using 3 Suggar groups in lagged mode running in 3 processors, 101 processors running CFD and 1 processor running PUF-14 with the coarse cylinder grid. For medium and fine cylinder grids 3 and 2 Suggar groups were used.

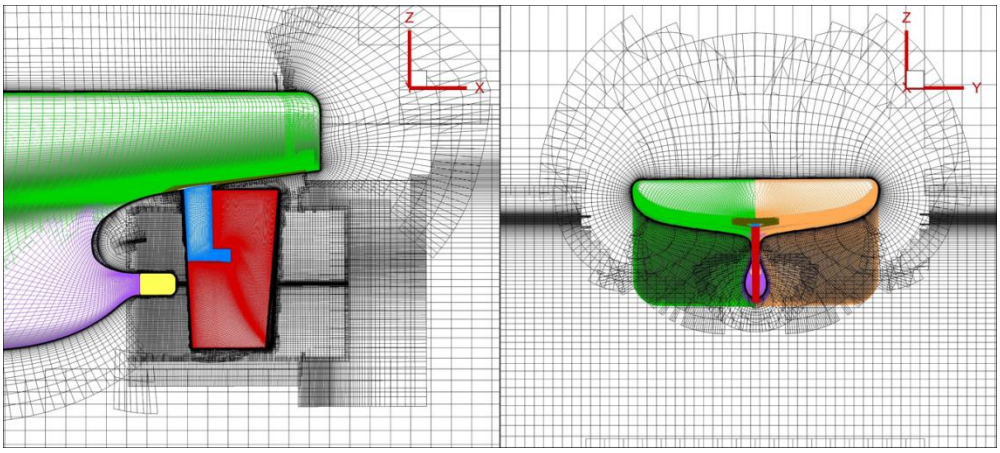

Figure 5.20 KCS overset grid topology for PUF-14 model.

The time step required in the coupled approach is determined by the number of angular increments per revolution, which is a multiple of the number of blades (Martin et al. 2015a). The direct CFD simulation of KCS performed with a non-dimensional time step of $\Delta t = 0.00025$ and the coupled REX\PUF-14 is executed with $\Delta t = 0.002$ which represents significant reduction in computational time. The propeller can rotate 3.33 degrees per time step in discretized approach while in coupled RE/PUF-14 approach propeller allows to rotate 26.64 degrees per time step. The longitudinal location of the center of gravity, the mass and the static wetted area of the ship are computed by running the code in hydrostatic mode. The resulting dimensionless values for longitudinal location

of the center of gravity, mass and static wetted area are 0.5097877, 4.14550E-3 and 0.179525, respectively.

Table 5.5 Details of the grids and decomposition information for coupled REX/PUF-14 simulations with three cylindrical coupling grids.

Grid	Size	Grid Points	Belongs to body	Processors (C, M, F)*
Boundary layer starboard 1	244×55×89	1179 K	Ship	6,2,1
Boundary layer starboard 2	241×58×53	740 K	Ship	4,2,1
Stern starboard	61×48×51	149 K	Ship	1,1,1
Hub starboard	71×41×51	148 K	Ship	1,1,1
Boundary layer port1	241×55×89	1179 K	Ship	6,2,1
Boundary layer port2	241×58×53	740 K	Ship	4,2,1
Stern port	61×48×51	149 K	Ship	1,1,1
Hub port	71×41×51	148 K	Ship/Propeller	1,1,1
Propeller hub	101×32×91	294 K	Ship/Propeller	2,1,1
Refinement Rudder	79×136×135	1450 K	Ship	1,1,1
Refinement	241×142×101	3456 K	Ship	18,6,3
Background	181×141×91	2322 K	Ship	12,4,2
Rudder stem refinement	61×45×109	299 K	Ship	2,1,1
Rudder stem starboard	61×55×89	298 K	Ship	2,1,1
Rudder stem port	61×55×89	298 K	Ship	2,1,1
Rudder stem top	55×45×61	150 K	Ship	1,1,1
Rudder stem bottom	119×41×61	297 K	Ship	2,1,1
Refinement gap top	26×103×55	147 K	Ship	1,1,1
Rudder gap	73×35×175	447 K	Ship/Rudder	3,1,1
Rudder top	113×36×37	150 K	Ship/Rudder	1,1,1
Rudder starboard	211×47×89	882 K	Ship/Rudder	5,2,1
Rudder port	211×47×89	882 K	Ship/Rudder	5,2,1
Rudder cap top	71×41×51	148 K	Ship/Rudder	1,1,1
Refinement wake	201×172×151	5220 K	Ship	8,3,2
Cylinder coarse grid	181×51×61	563 K	Ship	3,3,3
Cylinder medium grid	181×81×121	1774 K	Ship	3,3,3
Cylinder fine grid	211×91×181	3475 K	Ship	3,3,3
Refinement rudder bottom	121×117×21	297 K	Ship	2,1,1
Refinement rudder port	117×21×121	298 K	Ship	2,1,1
Refinement rudder starboard	117×21×121	297 K	Ship	2,1,1
Refinement rudder top	117×121×21	297 K	Ship	2,1,1
Total – coarse cylinder grid		**18.07 M**		**101**
Total – medium cylinder grid		**19.3 M**		**47**
Total – fine cylinder grid		**20.9 M**		**35**

*C: Coarse, M: Medium, F: Fine refer to cylinder grid size

5.8 Coupled REX/PUF-14 Self-Propulsion Computations

The self-propulsion computations are carried out with the ship free to surge, heave, roll, and pitch and restrained from yaw and sway motions, with the rudder restricted to straight condition . In this case the dimensionless proportional and integral constants were set to 60 and 40, respectively. The dimensionless target speed was set to 1 (24 knots at full scale) and the initial dimensionless RPS was set to 37 (corresponding to 118 RPM in full scale, close to the measured experimental value). The dimensionless time step was set to $\Delta t = 0.002$, taking approximately 72 hours of wall clock time to achieve self-propulsion.

Table 5.6 shows the propeller rotational speed and the ship velocity as self-propulsion is obtained for discretized propeller simulation, coupled REX/PUF-14 simulation, and experimental measurement. Figure 5.21 shows the time history of the ship and propeller rotational speeds as self-propulsion is reached. Self-propulsion at the target speed of 24 knots requires a propeller rotational speed of 115.98 RPM in full scale, compared to 118.04 RPM for discretized propeller and 116.1 RPM in the experiments. The experiments show a ship speed 24.2 knots before starting the maneuver, compared to 24.17 knots for discretized propeller and 24.06 knots for coupled REX/PUF-14. The error in propeller rotational speed is computed respect to the experimental value. Errors in RPM for the discretized and coupled approaches are 1.7% and -0.10%, respectively, showing that the coupled approach can compute self-propulsion properly.

Fig. 5.22 shows cross sections at constant x planes colored with dimensionless vorticity magnitude and the free surface colored by elevation for self-propulsion. As can be seen, the ship and propeller wakes are following the ship trajectory on self-propulsion conditions.

Table 5.6 Self-propulsion RPM and speed for discretized propeller, coupled REX/PUF-14 and experimental test.

Propeller Modeling	RPM	Ship Speed (Knots)	RPM Error
Direct	118.04	24.17	1.6%
Coupled	115.98	24.06	-0.10%
Experiment	116.1	24.2	0%

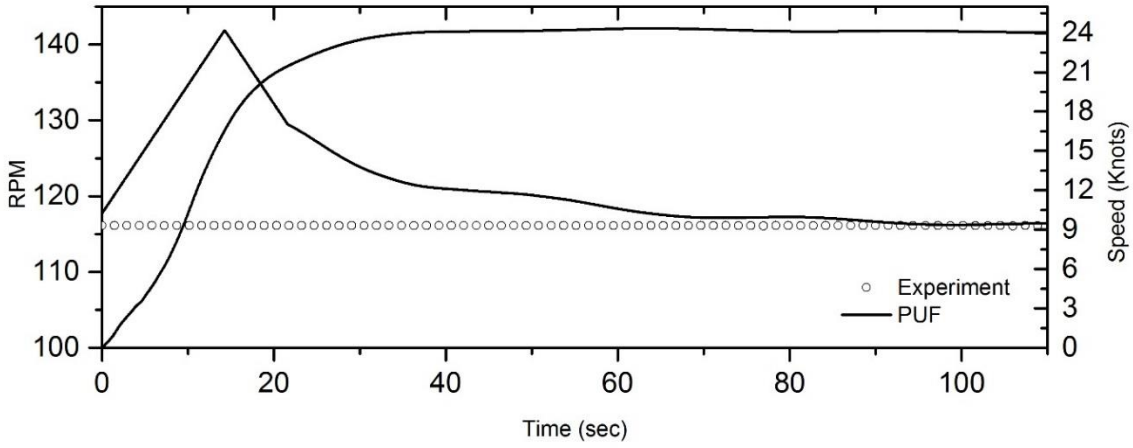

Figure 5.21 Time history of ship speed and propeller rotational speed for self-propulsion computation with coupled REX/PUF-14 method.

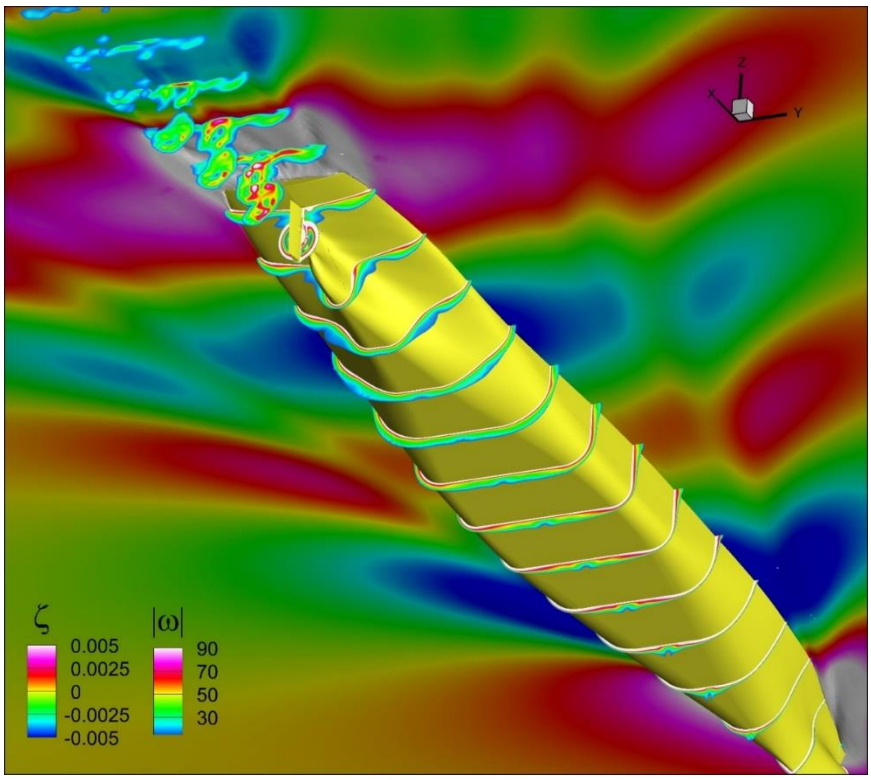

Figure 5.22 Free surface elevation and cross sections showing the vorticity magnitude at self-propulsion.

5.9 KCS 15/1 Zigzag Maneuver

In this section, computations for a 15/1 modified zigzag maneuver with the coupled REX/PUF-14 approach and comparison with discretized propeller simulations and experiments for motions, forces and moments are presented. In order to investigate the effects of the grid refinement around the rudder, coarse, medium and fine grids are used for the cylindrical coupling grids, see Table 5.5. All coupled REX/PUF-14 simulations were carried out with a non-dimensional time step of $\Delta t = 0.002$ and DDES turbulence model. The robustness of the approach was examined by also performing simulations with smaller time step, using explicit and implicit 6DoF solvers, and refining the coupling

cylindrical grids. Only changes in the coupling grid refinement had significant effects on the results, as discussed below.

5.10 Coupled REX/PUF-14 Maneuvering Results

Figure 5.23 shows the time histories of yaw, yaw rate, and rudder angle. Coupled REX/PUF solutions for the three cylinder grids coarse, medium, and fine are compared with the discretized propeller solution and experiments. The agreement between coupled REX/PUF-14 and discretized propeller predictions, and experiments is very good until 62 s from the beginning of the maneuver in. At that time the ship heading starts to deviate from discretized propeller predictions and experimental data and the heading overshoot is over-predicted. The second rudder execution from port to starboard for coupled REX/PUF-14 with the coarse cylinder grid occurs at 114.5 s, resulting in 8.7 and 10.1 s of phase delay respect to the discretized propeller and experimental data, respectively. The yaw rate predicted with the coarse cylinder grid shows a smaller rate of change than the yaw rate predicted with the medium and fine cylinder grids, between 60 and 70 s. This causes a slower change in yaw rate after the end of the rudder execution from starboard to port, and a higher predicted overshoot.

The results clearly show, refining the cylindrical coupling grid improves the rudder execute time and yaw angles and also reducing the phase error and first overshoot. It should be noted that, the coupling between REX and PUF-14 only requires a coarse grid but using a finer coupling cylindrical grid significantly improves the resolution of solving flow around the rudder, resolving turbulent structures better and predicting separation more accurately. Improvements from refining the coarse to the medium cylindrical grids are

obvious in Figure 5.23, but refining the medium grid to the fine grid does not show additional improvements in results. It is worth mentioning that, regardless of how fine the coupling grid is, the coupled REX/PUF-14 approach is unable to resolve blade tip or trailing edge vortices, and thus resulting in lower effective resolved turbulent fluctuations in the rudder than for discretized propeller computations. Results suggest that this limitation causes earlier separation in the rudder and thus limits the lift, reflected in the rudder yaw moment and its ability to steer the ship and the consequent higher heading overshoots.

In order to analyze the discrepancies in the prediction of yaw, yaw rate, and rudder execution time in coupled Rex/PUF-14 approach respect to the discretized propeller and experiments, the main contributors in total yaw moments are investigated here. Since for KCS the predicted values for roll and pitch are small, neglecting cross terms from other degrees of freedom is a good approximation, thus, the rate of change in yaw can be written as:

$$I_{\psi}\frac{d\dot{\psi}}{dt} = Mz_{Hull} + Mz_{Rudder} + Mz_{Propeller} \tag{5-7}$$

where I_{ψ}, is the yaw moment of inertia of the ship, ψ is the yaw, and Mz are the yaw moments due to hull, rudder, and propeller. Figure 5.24 illustrates the yaw moment for each component of Eq. (5-7) computed using coupled REX/PUF-14 and discretized propeller approaches. The overall trends are extremely similar for all terms, even though a phase delay is observed for the coupled REX/PUF-14 approach, with the most notable difference occurring at the end of the execution of the rudder from starboard to port starting at $t_1 = 49.1\,s$ for the coupled approach (the execution starts slightly earlier for the

discretized solution). At t_1 the rudder is fully deflected to starboard ($\delta = 15$ degrees) and the yaw angle reaches $\psi = 1$ degree, triggering the execution of the rudder to port. At time t_2 corresponds to the execution is complete and the rudder is fully deflected to port ($\delta = -15$ degrees). For coupled REX/PUF-14 with the fine cylindrical grid $t_2 = 62.6\ s$. At the end of the rudder execution both discretized and coupled approaches predict considerable fluctuations in rudder yaw moment until $t \cong 80\ s$, but with values slightly larger for the discretized propeller computations. The total yaw moment is then moderately stronger for the discretized propeller approach, resulting in a tighter maneuver. It is interesting to note that although moments prediction are so similar but yaw histories can present large discrepancies over the simulation since this value is integrated in time.

Figures 5.25 and 5.26 show the flow around the rudder on horizontal cross sections at three depths corresponding to 70% of the propeller radius above the propeller hub, at the propeller hub and 70% radius below the propeller hub. The coupled REX/PUF-14 results shown correspond to the fine cylinder grid. The incoming flow from the propeller and hull to the rudder is at low angle of attack and no significant separation is observed at time t_1. At time t_2 the rudder execution is completed and the incoming flow into the propeller exhibits a large angle of attack and considerable separation are captured in both discretized propeller and coupled REX/PUF-14 approaches. Notice that the explicit velocity fluctuations produced by the propeller in the discretized approach result in richer turbulent structures around the rudder, but in terms of average flow field both approaches presenting similar pattern.

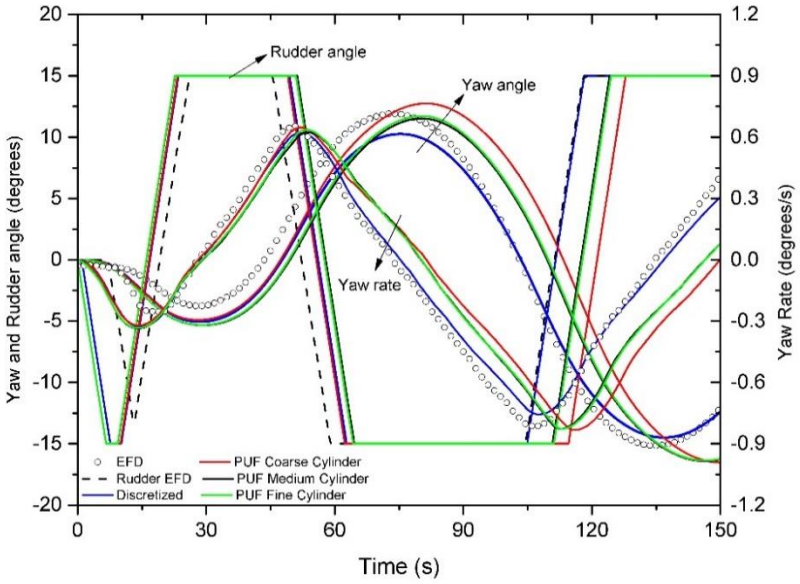

Figure 5.23 Time histories of yaw, yaw rate, and rudder angles for KCS 15/1 zigzag maneuver.

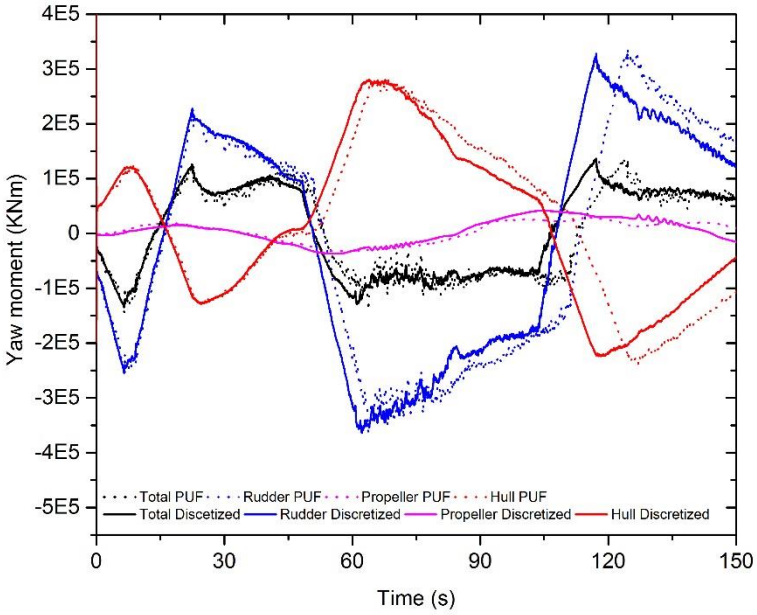

Figure 5.24 Yaw moment components for computations with discretized propeller and coupled REX/PUF-14 with the fine cylindrical grid.

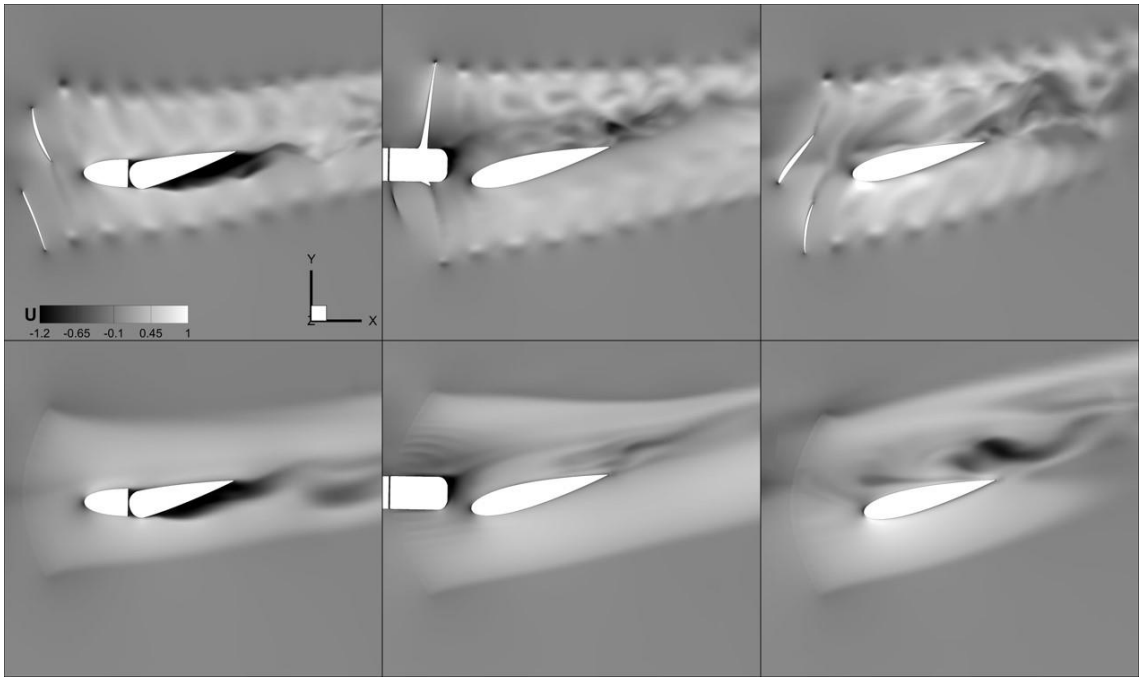

Figure 5.25 Velocity contour around the rudder at horizontal sections 0.7R above the shaft axis (left), at the shaft axis (center), and 0.7R below the shaft axis for discretized propeller (top) and coupled REX/PUF-14 (bottom) at time t_1.

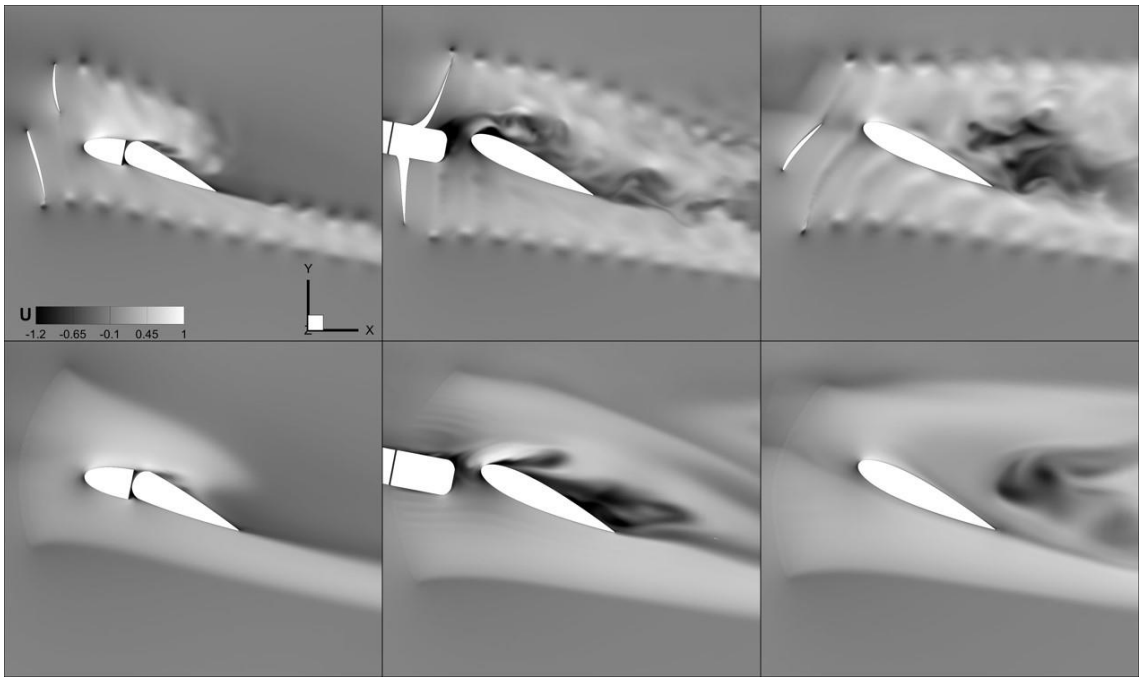

Figure 5.26 Same as Figure 5.25 but at time t_2.

Figure 5.27 displays the instantaneous pressure on the rudder surface at times t_1 and t_2 for discretized propeller and coupled REX/PUF-14 approaches. At time t_1 the rudder starts the maneuver from starboard to port after turning to starboard for a while, and thus the pressure side is on starboard and as shown in Figure 5.24 the load is moderate. At time t_2 the rudder completes the execution to port, resulting on a load approximately four times higher than at t_1 (see Figure 5.24), and with the pressure side at port. The predicted pressures for coupled REX/PUF-14 and discretized propeller approaches are qualitatively similar, though some differences are apparent. The discretized propeller results contain tip vortices that are reflected as small wavelength pressure fluctuations on the rudder surface, a feature absent in the coupled approach. On the suction side, the pressure recovery is predicted slightly earlier for the discretized propeller approach, but the minimum pressures are lower than for the coupled approach. Similar results are observed on the pressure side, where slightly higher pressures are present with the discretized propeller approach. This is probably due to the discretized propeller producing stronger swirl because of a lower efficiency that results in more torque and rotational momentum transfer to the fluid, see Figures 5.3 and 5.10. While similarities shown in Figures 5.25 through 5.27 are consistent with the close results observed in Figures 5.23 and 5.24, the differences discussed do not suggest a clear reason for the discrepancies in histories in yaw and yaw rate displayed in Figure 5.23.

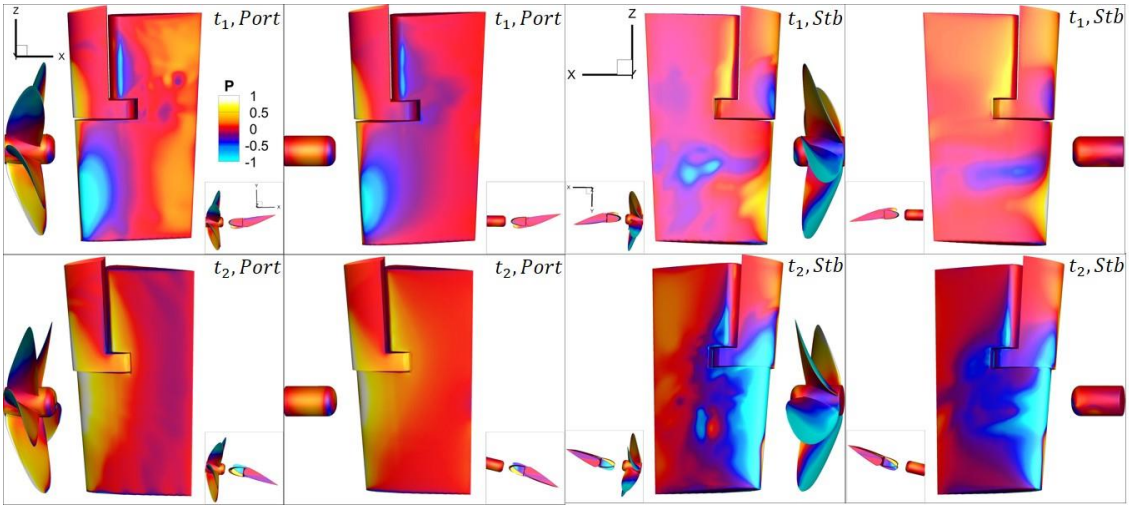

Figure 5.27 Pressure distribution on rudder surfaces at times t_1 and t_2 for discretized propeller (1st and 3rd columns) and coupled REX/PUF-14 simulations (2nd and 4th columns).

Roll rate and roll, pitch and drift angle are shown in Figure 5.28. The results for medium and fine coupling cylindrical grid sizes are very close to discretized propeller simulations and experimental data for all variables, though the maximum roll angle is slightly over-predicted for both medium and fine coupling cylindrical grids in coupled REX/PUF-14 and discretized propeller results. Notice that the pitch angles are very small but the trends are still consistent with experiments. The roll rate, related to the roll damping, is also very consistent with experiment for medium and fine cylindrical coupling grids but coarse grid shows higher discrepancies. The drift angle also presents comparable data with experiment and discretized propeller, especially in amplitude.

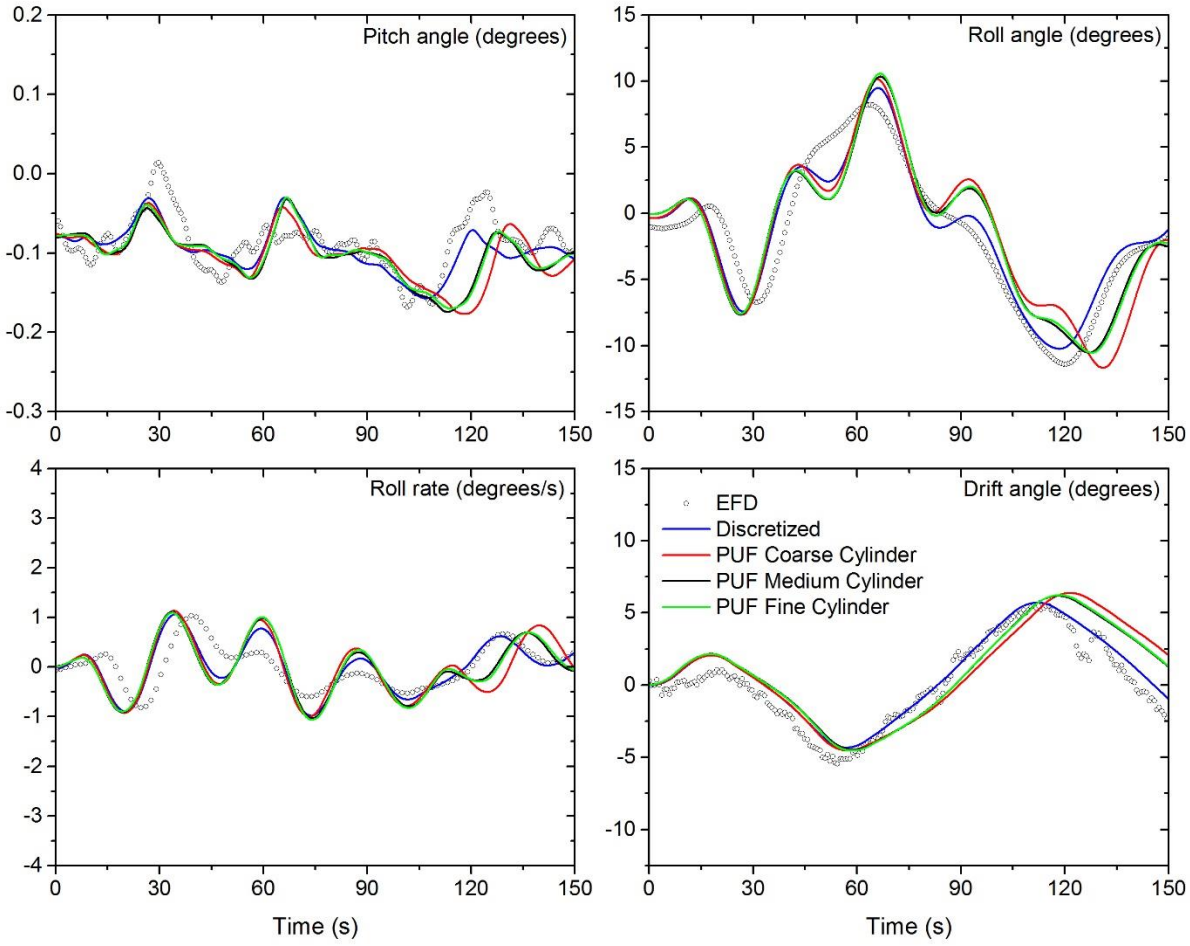

Figure 5.28 Time history of pitch, roll, and drift angles and roll rate for coupled REX/PUF-14 and discretized propeller approaches.

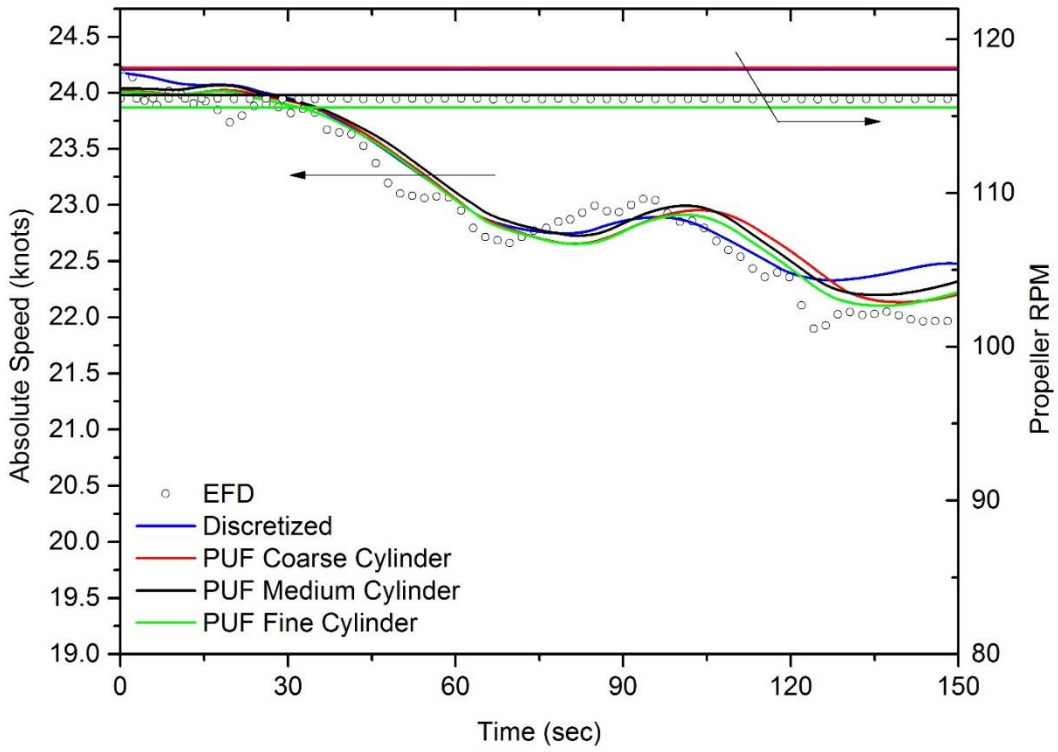

Figure 5.29 Ship speed and propeller RPM.

Figure 5.29 shows the time evolution of the absolute ship speed for discretized propeller and coupled REX/PUF-14 approaches and the comparison with experiment. The velocity of the ship decreases rapidly as the maneuver progresses due to the added resistance of the rudder and turning hull. The speed loss is correlated with roll angle and drift angle and both of these factors are affected by the rudder execution. The discretized propeller and coupled REX/PUF-14 approaches show good agreement with the experiments in the first 90 sec. of the simulation, but over-predict the speed on the final stages of the simulation, in particular the discretized propeller results.

Figure 5.30 shows the time histories of propeller thrust and torque. As the cylindrical coupling grid is refined, the coupled REX/PUF-14 approach exhibits better

agreement with the experiments and the discretized propeller computations. The discretized propeller presents high frequency oscillations in thrust and torque with the blade passage frequency as blades are exposed to various inflow speeds in the propeller wake plane. These oscillations are not present in the coupled REX/PUF-14 method since blade forces are integrated over one propeller rotation as discussed in section 5.2, and are absent in the data as well since the sampling rate is not high enough to capture them. The propeller torque in Fig. 5.30 is computed with respect to the propeller *x*-axis, which is parallel to the ship system's *x*-axis. All cylindrical coupling grids show similar trends as experiment but finer grids present better match with discretized propeller and experiment.

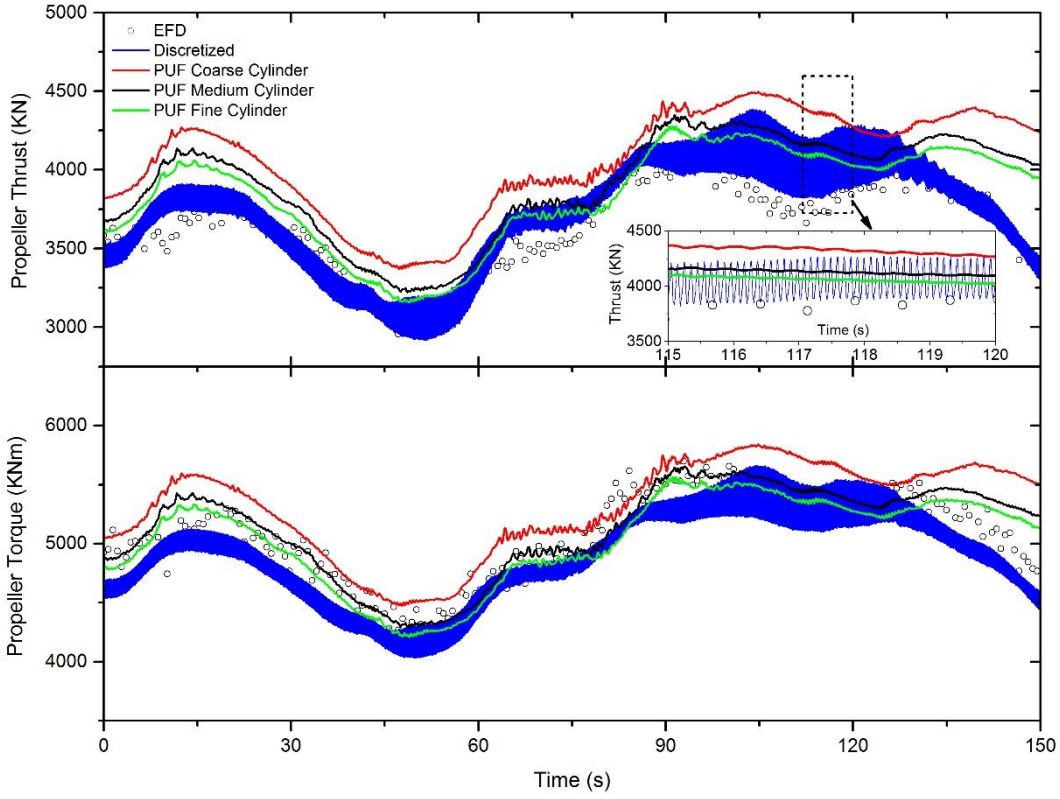

Figure 5.30 Time history of propeller thrust and torque.

Rudder resistance and yaw moment are shown in Figure 5.31. Every time the rudder is executed there is a minimum in rudder resistance as the rudder aligns with the flow. Between 60 and 80 s both simulation approaches predict increased resistance due to flow separation, which is not observed in the experiments. This significant resistance predicted by the simulations is a major source of speed loss as shown in Figure 5.29. The opposite condition is also valid, every time the rudder resistance reached the minimum there is some degree of speed recovery in Figure 5.29. The rudder yaw moment respect to the shaft is also shown in Figure 5.31. While both simulation approaches produce similar results consistent with the preceding discussions, they follow the experimental data only in trend.

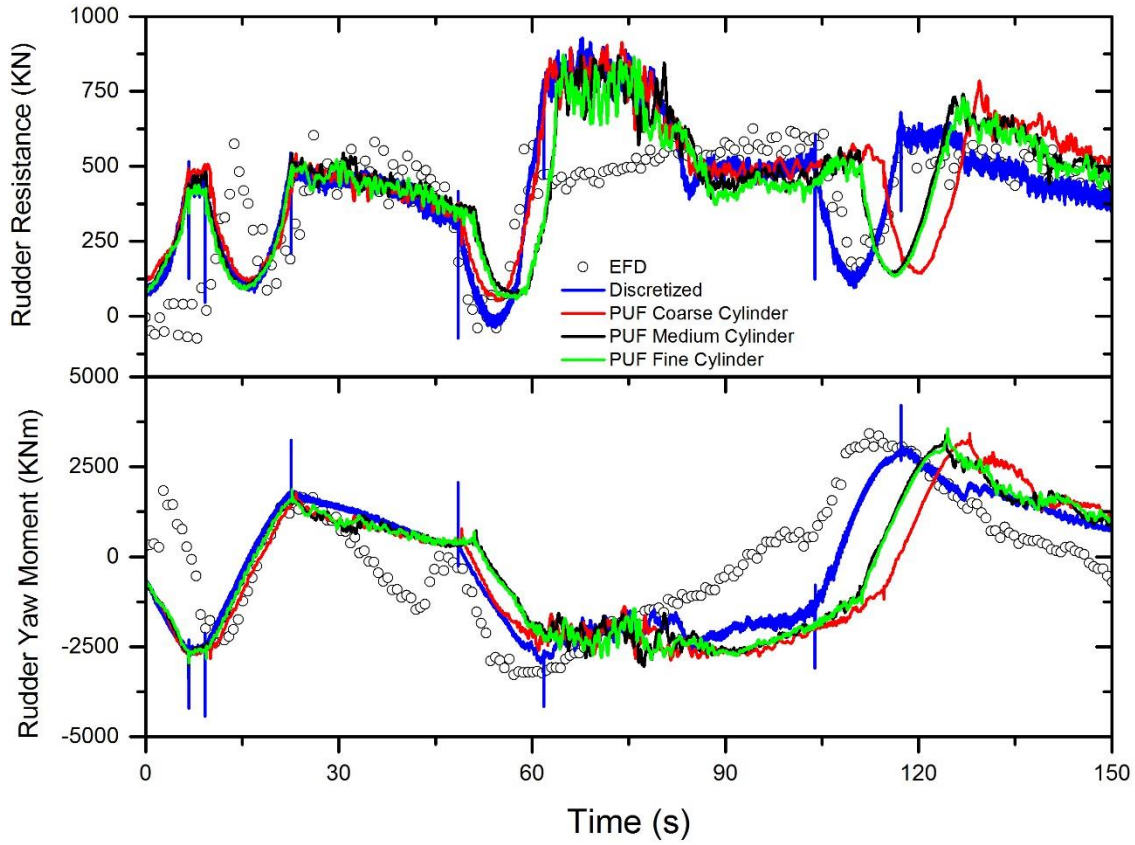

Figure 5.31 Time history of rudder resistance force and yaw moment.

5.11 Summary

In this chapter, a coupled potential propeller model PUF-14 and CFD solver REX was utilized for maneuvering simulation of Korean Container Ship (KCS) in deep water. Since in coupled approach the required time steps are allowed to consider one order of magnitude larger than for the discretized propeller approach, the coupled REX/PUF-14 approach can run approximately five times faster, results in significant saving in computational time.

In the first section of this chapter, the coupled approach performance was examined on OWCs simulations for SVA propeller and results compared with experimental data and discretized propeller simulations. Next, propeller/rudder interaction was considered for three rudder angles and wide range of propeller advance coefficients. Results show good performance of coupled approach at design points. The final part of this chapter involved simulation of KCS modified zigzag maneuver in deep water with coupled REX/PUF-14 approach. Three cylindrical coupling grids were tested to evaluate coupled approach performance in predicting motions, forces, and moments during the maneuver. The results showed, irrespective of how fine the coupling grid is, the coupled REX/PUF-14 approach was still suffered from lack of resolution in the propeller wake and incoming flow to the rudder due to the limitations of model in resolving blade vortical structures.

CHAPTER 6

CONCLUSION AND FUTURE WORK

A high fidelity direct CFD and coupled CFD/Potential solver approaches for maneuvering applications was presented. The objective of this thesis was to assess the capability of CFD code REX and overset technique to perform direct simulations of maneuvering predictions. Also, coupling REX with the potential flow propeller solver PUF-14 was investigated in order to discover significant time saving over discretized propeller computations in maneuvering applications.

Simulation of the KCS 15/1 modified zigzag maneuver and 10/10 standard zigzag maneuver with semi-balanced horn rudder and discretized propeller were presented. While the results and comparisons with experimental data show that using CFD to predict ship maneuvering is feasible, computational cost remains a obstacle for many practical applications. The comparison between experiments and simulations was very satisfactory for motions and motion rates. Propeller thrust and torque were also very well predicted. These good results are a consequence of the ability of CFD to properly predict integrated forces and moments on streamlined bodies, even for relatively coarse grids. Though dynamic maneuvers result in significant more complex flow, in particular the inflow and wake of the propeller, still prediction of forces and moments and consequent motions is good. The main differences between CFD and experiments were observed in the prediction of the absolute speed in 15/1 zigzag maneuver, where experiments showed a large speed loss when the rudder was operated to the port. These speed decreases were significantly weaker in CFD, indicating that modeling of the rudder flow needs improvement. The flow

around the rudder is extremely complex, as the rudder is located downstream of the propeller and its inflow contains a variety of vortical scales that makes turbulence modeling specially challenging.

In order to investigate the effects of shallow water condition on maneuvering performances, 20/5 zigzag maneuver for the container ship KCS was studied numerically and results compared with experimental data. The CFD analysis included grid studies for the self-propulsion stage and the zigzag maneuver at the nominal rudder rate, and a simulation with the medium grid for the actual achieved experimental rudder rate. This work also presented the first grid study for direct CFD simulations of self-propulsion and free maneuvers. The self-propulsion grid study showed good grid convergence for the most relevant variables (RPM and propeller thrust and torque), though higher uncertainty for the propeller side force. The grid study for the zigzag maneuver was performed using the same procedures designed for steady-state processes, results in much higher grid uncertainties than the self-propulsion study. Several parameters exhibited oscillatory convergence or even divergence, highlighting the difficulties of performing grid studies on naturally transient problems such as ship maneuvers. Comparison of CFD results with EFD data were satisfactory for the self-propulsion condition, with errors below 2.7% for all relevant variables. For the zigzag maneuver at the experimental rudder rate CFD compared very well with the experiments for all variables, except yaw and yaw rate, which exhibited errors of about 15% for yaw on the overshoots and around 20% for the yaw rate, in both cases lower than EFD data. Possible reasons for these under-predictions include under-prediction of rudder yaw moment and over-prediction of the hull yaw moment, likely due to improper separation caused by errors in the turbulence model. In addition, the walls of the tank were

neglected in the CFD simulations, which could have a significant role on the discrepancies observed with EFD because of the higher blockage occurring in shallow water conditions.

For the first time the ability of a coupled CFD/propeller code approach to simulate maneuvers in ships, where the rudder is located downstream of the propeller, was studied in this thesis. First, the extent of the influence of the presence of the rudder in the wake of a propeller in the propeller and rudder performance were investigated. The study was performed using the CFD code REX and the propeller code PUF-14. Simulations of propeller/rudder interaction with three different rudder-propeller gap sizes ($D_{PR}/R = 0.2, 0.4, 0.8$) and three different rudder angles ($\delta = 0, 20, -20\ deg.$) showed that the coupled REX/PUF-14 approach predicts forces and moments near design point in good agreement with discretized propeller results. At very low advance coefficients the prediction is poor due to inherent limitations of PUF-14 to operate at high loads and inability to capture the wake roll up and blade leading edge separation. A grid study was performed for $J = 0.6$ and a rudder angle $\delta = 20$ degrees, exhibiting monotonic convergence for propeller thrust and torque coefficient while the rudder side force coefficient shows oscillatory convergence. The grid uncertainties for propeller thrust and torque coefficients suggest that the effects of the grid changes are small for the present range of grid sizes.

A 15/1 zigzag maneuver for the KCS container ship, in which case the rudder is very close downstream of the propeller, was also analyzed. Comparison of coupled results with discretized propeller method and EFD data are very satisfactory for the self-propulsion condition, in which the rudder is maintained straight. Coarse, medium, and fine coupling cylindrical grids, used to exchange CFD and propeller model data but also to

refine the solution around the rudder, were employed for the simulations of the zigzag maneuver. Results showed that using finer coupling cylindrical grids improves resolution, helping the DDES approach better predict forces on the rudder. Prediction of motions, forces and moments and mean flow field with the coupled REX/PUF-14 approach were comparable with results obtained with discretized propeller simulations and agree well with experiments, though as implemented the coupled approach is unable to resolve tip vortices and other flow structures that interact with the rudder, potentially affecting separation. It can be concluded that approaches coupling CFD with a potential flow propeller code are an effective and economical way to perform direct simulation of surface ship maneuvers with CFD, providing time savings approaching an order of magnitude in cost at the price of poorer resolution of the propeller/rudder flow.

Future work will focus on analyzing the turbulence quantities and flow around the rudder which is extremely complex, as the rudder is located downstream of the propeller and its inflow contains a variety of vortical scales that makes turbulence modeling specially challenging.

Adding turbulence to the propeller wake in the coupled REX/PUF-14 in order to compensate the effects of unresolved tip vortices and other flow structures and help prediction of the separation on rudder is considered as future work. Also, corrections to computations of the wake within PUF-14 to account for the presence and operation of the rudder may yields better results.

REFERENCES

ANSI/ASME Power Test Codes-PTC 19.1 (2005). *Test Uncertainty*, American Society of Mechanical Engineers, New York, New York, USA.

Aoki, I., Kijima, K., Furukawa, Y., and Nakiri, Y. 2006. "On the Prediction Method for Maneuverability of a full scale Ship." *Journal of Japan Society of Naval Architect and Ocean Engineering*. **3**, 157-165.

Araki, M., Ohashi, K., and Hirata, N. 2014. "KVLCC2 Simulations with Overset Grid Method." *Proceeding SIMMAN 2014 Workshop on Verification and Validation of Ship Maneuvering Simulation Methods*. Copenhagen, Denmark.

Black, S. D. and Michael, T. J. 2003. "Experiences Using a Coupled Viscous/Potential-Flow Unsteady Propeller Analysis Procedure.", *Proceedings, SNAME Propeller/Shafting Symposium*, Virginia Beach, VA.

Boger, D., and Dryer, J. 2006. "Prediction of Hydrodynamic Forces and Moments for Underwater Vehicles Using Overset Grids." *44th AIAA Aerospace Sciences Meeting and Exhibit*. Reno, Nevada, USA.

Broglia, R., Muscari, R., and Di Mascio, A. 2006. "Numerical Analysis of Blockage effects in PMM Tests." *Proceeding of 26th Symposium on Naval Hydrodynamics*. Rome, Italy.

Calcagni D, Salvatore F, Dubbioso G, Muscari R. 2017. A Generalized Unsteady Hybrid DES/BEM Methodology Applied to Propeller-Rudder Flow Simulation. Proceedings of the VII International Conference on Computational Methods in Marine Engineering; May 15-17; Nantes, France.

Carlton, J. 2012. "Marine Propellers and Propulsion." Butterworth-Heinemann, 3rd Edition.

Carrica, P. M., Mofidi, A., Eloot, K., and Delefortrie, G. 2015. "Direct Simulation and Experimental Study of Zigzag Maneuver of KCS in Shallow Water." *Ocean Engineering*. **112**, 117-133.

Carrica, P.M., and Stern, F. 2008a. "DES Simulations of KVLCC1 in Turn and Zigzag Maneuvers with Moving Propeller and Rudder." *SIMMAN Workshop on Ship Maneuvering Simulation Methods*. Copenhagen, Denmark.

Carrica, P.M., Castro, A.M., and Stern, F. 2010a. "Self-Propulsion Computations Using Speed Controller and Discretized Propeller with Dynamic Overset Grids." *Journal of Marine Science and Technology*. **15**, 316-330.

Carrica, P.M., Huang, J., Noack, R., Kaushik, D., Smith, B., and Stern, F. 2010b. "Large-Scale DES Computations of the Forward Speed Diffraction and Pitch and Heave Problems for a Surface Combatant." *Computers and Fluids*. **39**, 1095–1111.

Carrica, P.M., Ismail, F., Hyman, M., Bhushan, S., and Stern, F. 2013. "Turn and Zigzag Maneuvers of a Surface Combatant Using a URANS Approach with Dynamic Overset Grids." *Journal of Marine Science and Technology*. **18**, 166-181.

Carrica, P.M., Ismail, F., Hyman, M., Bhushan, S., and Stern, F. 2013. "Turn and Zigzag Maneuvers of a Surface Combatant Using a URANS Approach with Dynamic Overset Grids," *Journal of Marine Science and Technology*. **18**, 166-181.

Carrica, P.M., Paik, K. J., Hosseini, H.S., and Stern, F. 2008b. "URANS Analysis of a Broaching Event in Irregular Quartering Seas." *Journal of Marine Science and Technology*. **13**, 395–407.

Carrica, P.M., Wilson, R.V., and Stern, F. 2007a. "An Unsteady Single-phase Level Set Method for Viscous Free Surface Flows." *International Journal for Numerical Methods in Fluids*. **53**, 229–256.

Carrica, P.M., Wilson, R.V., Noack, R.W., and Stern, F. 2007b. "Ship Motions Using Single-phase Level Set with Dynamic Overset Grids." *Computers and Fluids*. **36**, 1415–1433.

Castro, A.M., and Carrica, P.M. 2013. "Bubble Size Distribution Prediction for Ship Flows: Model Evaluation and Numerical Issues." *International Journal of Multiphase Flow*. **57**, 131-150.

Castro, A.M., Carrica, P.M., and Stern, F. 2011. "Full Scale Self-propulsion Computations Using Discretized Propeller for the KRISO Container Ship KCS." *Computers and Fluids*. **51**, 35-47.

Celik, I., Klein, M., and Janicka, J. 2009. "Assessment measures for LES application." *Journal of Fluids Engineering*. **131**, 031102.

Celik, I., Klein, M., Freitag, M., and Janicka, J. 2006. "Assessment measures for URANS/DES/LES: an overview with applications." *Journal of Turbulence*. **7**, 1–27.

Chase, N., and Carrica, P.M. 2013. "Submarine Propeller Computations and Application to Self-Propulsion of DARPA Suboff." *Ocean Engineering*. **60**, 68-80.

Coleman, H. W., and Steele, W. G. 1999. "Experimentation and Uncertainty Analysis for Engineers." *2nd Edition, Wiley*, New York, NY.

Cura-Hochbaum, A., and Uharek, S. 2014. "Prediction of the Maneuvering Behavior of the KCS Based on Virtual Captive Tests." *Proceeding SIMMAN 2014 Workshop on Verification and Validation of Ship Maneuvering Simulation Methods*. Copenhagen, Denmark.

Cura-Hochbaum, A., Vogt, M., and Gatchell, S. 2008. "Maneuvering Prediction for Two Tankers Based on RANS Simulations." *Proc. SIMMAN 2008 Workshop on*

Verification and Validation of Ship Maneuvering Simulation Methods, Lyngby, Denmark.

Delefortrie, G., Eloot, K. 2014. "Mathematical Mode for Shallow Water Maneuvers with the KVLCC2 as Used in SIMMAN 2014." *Proc. SIMMAN 2008 Workshop on Verification and Validation of Ship Maneuvering Simulation Methods*, Lyngby, Denmark.

Drouet, A., Jacquin, E., Alessandrini, B., Ferrant, B., Gentaz, L., Monroy, C., Rousset, J. M., Guillerm, P. E., and Perdon, P. 2008. "Simulation of Unsteady Ship Maneuvering on Calm water and in Waves Using Free-surface RANS Solver." *Proceeding 27th Symposium on Naval Hydrodynamics*. Seoul, Korea.

Dubbioso, G. and Viviani, M. 2012. "Aspects of Twin Screw Ships Semi-empirical Maneuvering Models." *Ocean Engineering*, **48**, 69-80.

Eloot K., Delefortrie, G., Vantorre, M., and Quadvlieg, F. 2015. "Validation of Ship Manoeuvring in Shallow Water through Free Running Tests." *OMAE 2015*, St. John's, Canada.

Esmaeilpour, M., Martin, J.E., Carrica, P.M. 2016. "Near-field flow of submarines and ships advancing in a stable stratified fluid." *Ocean Eng*. **123**, 75-95.

Ferrant, P., Gentaz, L., Monroy, C., Luquet, R., Ducrozet G., Alessandrini, B., Jacquin, E., and Drouet, A. 2008. "Recent Advances towards the Viscous Flow Simulation of Ships Maneuvering in Waves." *23rd Int. Workshop Water Waves Floating Bodies*. Jeju, Korea.

Fosson, T.I. 2011. "Handbook of Marine Craft Hydrodynamics and Motion Control." *New York: John Willy and Sons Ltd*.

Gritskevich, M. S., Garbaruk, A. V., Schutze, J., and Menter, F. R. 2011. "Development of DDES and IDDES Formu;ations for the K-Ω Shear Stress Transport Model." *Flow, Turbulence and Combustion*. **88**, 431-449.

Guilmineau, E., Deng, G., Queutey, P., Visonneau, M., Leroyer, A., and Wackers, J. 2014. "URANS Simulations of Planar Motion Mechanism for Two Hulls." *Proceeding SIMMAN 2014 Workshop on Verification and Validation of Ship Maneuvering Simulation Methods*. Copenhagen, Denmark.

International Maritime Organization, 2002. "Standards for Ship Maneuverability." IMP resolution MSC. 137. 76.

International Towing Tank Conference Maneuvering Committee, 2008. "Final report and recommendations to the 25th ITTC." *Proc. 25th International Towing Tank Conference*. Fukuoka, Japan.

ITTC Maneuvering Committee, 2011. "Maneuvering Committee Report and Recommendations." *26th International Towing Tank Conference*, Rio de Janeiro, Brazil.

ITTC Maneuvering Committee, 2014. "Final Report and Recommendations to the 27th ITTC Conference." *27th International Towing Tank Conference*, Copenhagen, Denmark.

ITTC Quality Manual, 2014. "ITTC – Recommended Procedures and Guidelines: Uncertainty Analysis for Free Running Model tests (7.5-02-06-05)." Available at http://ittc.info/downloads/Quality%20systems%20manual/Index/index.pdf.

Jacquin, E., Guillerm, P.E., Drouet, A., and Perdon, A. B. 2006. "Simulation of Unsteady Ship Maneuvering Using Free-Surface RANS Solver." *26th ONR Symposium. Naval Hydrodynamics*. Rome, Italy.

Jensen, G., Klemt, M., and Xing, Y. 2004. "On the Way to the Numerical Basin for Seakeeping and Maneuvering." *9th Symposium. Practical Design Ships*. Luebeck, Germany.

Krasilnikov, V. 2013. "Self-Propulsion RANS Computations with a Single-Screw Container Ship." *Proceedings*, 3rd International Symposium on Marine Propulsors. Australia.

Li, J., Castro, A.M., and Carrica, P.M., 2015a. "A Pressure–Velocity Coupling Approach for High Void Fraction Free Surface Bubbly Flows in Overset Curvilinear Grids." *International Journal for Numerical Methods in Fluids*. **79**, 343-369.

Li, Y., Castro, A.M., Sinokrot, T., Prescott, W., and Carrica, P.M. 2015b. "Coupled CFD/Multibody Dynamics Approach for Wind Turbine Simulations," *Renewable Energy*. **76**, 338-361.

Martin, J. E., Michael, T., and Carrica, P. M. 2014. "Overset Simulations of a Submarine in Self-propelled and Maneuvering Conditions." *Proceeding The 30th Symposium on Naval Hydrodynamics*. Hobart, Australia.

Martin, J.E., Michael, T., and Carrica, P.M. 2015. "Submarine Maneuvers Using Direct Overset Simulation of Appendages and Propeller and Coupled CFD/Potential Flow Propeller Solver," *Journal of Ship Research*. **59**, 31-48.

Menter, F. R. 1994. "Two-Equation Eddy-Viscosity Turbulence Models for Engineering Applications." *AIAA Journal*. **32**, 1598-1605.

Mikkelsen, H., Sanchez, F., and Knudsen, S. 2014. "RANS Simulation of the KCS Container Ship in Pure Sway Motions." *Proceeding SIMMAN 2014 Workshop on Verification and Validation of Ship Maneuvering Simulation Methods*. Copenhagen, Denmark.

Mofidi, A., and Carrica, P.M. 2014a. "Simulations of Zigzag Maneuvers for a Container Ship with Direct Moving Rudder and Propeller." *Computers and Fluids.* **96**, 191-203.

Mofidi, A., and Carrica, P.M. 2014b. "Verification of 20/5 Zigzag Maneuver for a Container Ship with Direct Moving Rudder and Propeller." *Proceeding SIMMAN 2014 Workshop on Verification and Validation of Ship Maneuvering Simulation Methods*. Copenhagen, Denmark.

Moriyama, F., 1981. "On the Effect of a Rudder on Propulsive Performance.", *Journal of the Society of Naval Architects of Japan.*, **150**, 63-73.

Muscari, R., Broglia, R., and Di Mascio, A. 2008a. "Trajectory Prediction of a Self-propelled Hull by Unsteady RANS Computations." *27th ONR Symposium Naval Hydrodynamics*. Seoul, Korea.

Muscari, R., Broglia, R., and Di Mascio, A. 2008b. "Analysis of the Flow around a Maneuvering VLCC." *Proceedings of the ASME 27th International Conference on Offshore Mechanics and Arctic Engineering*. Estoril, Portugal.

Neitzel, J. C., Pergande, M., Berger, S., and Abdel-Maksoud, M., 2015. "Influence of the Numerical Propulsion Modelling on the Velocity Distribution behind the Propulsion Device and Maneuvering Forces.", *Proceedings,* 4th International Symposium on Marine Propulsors, Texas, US.

Noack, R. 2005. "SUGGAR: A General Capability for Moving Body Overset Grid Assembly." *17th AIAA CFD Conf*. Toronto, ON, Canada.

Noack, R.W., Boger, D., Kunz, R., and Carrica, P.M. 2009. "Suggar++: An Improved General Overset Grid Assembly Capability." *AIAA Paper 2009-3992*. doi:10.2514/6.2009-3992.

Otzen, J. F., and Agdrup, K. 2008. "Maneuvering Prediction Based on PMM Tests for Two Versions of a VLCC Tanker." *Proc. SIMMAN 2008 Workshop on Verification and Validation of Ship Maneuvering Simulation Methods*, Lyngby, Denmark.

Paik, K-J., and Carrica, P.M. 2014. "Fluid-Structure Interaction for an Elastic Structure Interacting with Free Surface in a Rolling Tank." *Ocean Engineering.* **84**, 201-212.

Paik, K-J., Carrica, P.M., Lee, D., and Maki, K. 2009. "Strongly Coupled Fluid–Structure Interaction Method for Structural Loads on Surface Ships." *Ocean Engineering.* **36**, 1346–1357.

Pankajakshan, R., Remotigue, S., Taylor, L., Jiang, M., Briley, W., and Whitfield, D. 2004. "Validation of Control-Surface Induced Submarine Maneuvering Simulations using UNCLE." *24th ONR Symposium Naval Hydrodynamics*. Fukuoka, Japan.

Rijpkema, D., Starke, B., and Bosschers, J. 2013. "Numerical Simulation of Propeller-hull Interaction and Determination of the Effective Wake Field Using a Hybrid RANS-

BEM Approach." *Proceedings, 3rd International Symposium on Marine Propulsors*. Australia.

Shen, Z., Wan, D., and Carrica, P. M. 2014. "RANS Simulations of Free Maneuvers with Moving Rudders and Propellers Using Overset Grids in OpenFoam." *Proceeding SIMMAN 2014 Workshop on Verification and Validation of Ship Maneuvering Simulation Methods*. Copenhagen, Denmark.

Shen, Z., Wan, D., and Carrica, P. M. 2015. "Dynamic Overset Grids in OpenFOAM with Application to KCS Self-propulsion and Maneuvering." *Ocean Engineering*. **108**, 287-306.

SIMMAN 2008, "Workshop on Verification and Validation of Ship Maneuvering Simulation Methods*." Workshop Proceedings*, Copenhagen, Denmark.

SIMMAN 2014, "Workshop on Verification and Validation of Ship Maneuvering Simulation Methods."*Workshop Proceedings*, Copenhagen, Denmark.

Steinwand, M., 2006. "Manövrierversuche mit einem Modell des Kriso Container Ship (KCS) Modell Nr. M1203S 001." *Report 3293*, Schiffbau-Versuchsanstalt Potsdam GmbH (In German).

Stern, F., Kim, H.T., Patel, V.C., and Chen, H.C. 1988. "A Viscous-Flow Approach to the Computation of Propeller–Hull Interaction," *Journal of Ship Research*. **32**, 246–262.

Stern, F., Wilson, R.V., Coleman, H.V., and Paterson, E.G. 2001. "Comprehensive Approach to Verification and Validation of CFD Simulations-Part 1&2: Methodology and Procedures." *ASME Journal of Fluids Engineering*. **124**, 793-802.

Thompson, J. F., Zahir, U.A., Warsi, and C. Wayne Mastin. 1985. *Numerical GridGeneration: Foundations and Applications*. **38**. North-holland Amsterdam.

Toxopeus, S., L. 2013. "Viscous-Flow Calculations for KVLCC2 in Deep and Shallow Water," *International Conference on Computational Methods in Marine Engineering*. **29**, 151-169.

Venkatesan G., and Clark, W. 2007. "Submarine Maneuvering Simulations of ONR Body 1." *Proceeding of OMAE2007, 26th International Conference on Offshore Mechanics and Arctic Engineering*. San Diego, USA.

Warren, C., Taylor, T., and Kerwin, J. 2000. "A Coupled Viscous/Potential Flow Method for the Prediction of Propulsor-induced Maneuvering Forces." *Proceedings SNAME Propellers/Shafting Symposium*, VA, USA.

Wilson, R., Shao, J., and Stern, F. 2004. "Discussion: Criticism of the "Correction Factor" Verification Method" *ASME Journal of Fluids Engineering*. **126**, 704-706